

FINAL
IN-91-2R
Smyth

**Studies for the Loss of Atomic
and Molecular Species from Io**

William H. Smyth

Atmospheric and Environmental Research, Inc.
840 Memorial Drive
Cambridge, MA 02139-3794

Final Report for the Period of
May 7, 1993 to May 6, 1996

primary orbits, and these points become the starting points for the secondary species. Velocities for the secondary species are initialized as being the sum of the primaries velocity at the initial point plus some excess energy generated from the dissociation processes. A weighting factor is associated with each secondary orbit and reflects the fact that the primary species is partially depleted at the point in the orbit where it gives rise to the secondary species and also that the dissociative branching ratios are properly included for each secondary species.

Additional efforts in the second year were directed to generalization of the SO₂ neutral cloud model for SO₂ escape from Io in order to investigate the spatial distribution of the SO₂, SO, O₂, S, and O neutral clouds produced near Io and in the circumplanetary space. This generalization has resulted in the addition of almost 1000 lines of new code to the numerical model. The Io model has been improved to include multiple neutral species and their interconversion into each other. Previously only the destruction of a single neutral species due to its interaction with the plasma torus was treated, where for a neutral (parent) molecule, the initial creation source rates for the daughter and granddaughter products were calculated. Now SO₂, SO, O₂, S, and O can be simultaneously followed taking into account not only the destruction of each species by the usual torus interactions and photo processes but also their formation from more complex molecules. The formation of SO from the dissociation of SO₂, O₂ from the dissociation of SO₂, S from the dissociation of SO₂ and SO, and O from the dissociation of SO₂, SO, and O₂ are now taken into account. In this way, a pure SO₂ Io exospheric source can be followed as it breaks up into SO, O₂, S, and O. The secondary species SO, and O₂ can also be simultaneously followed as they turn into S and O. For each species, the column density and brightness of various desired emission lines may be calculated on the sky plane of the observer. In addition to this generalization, the model has been rendered more efficient by some restructuring. The model is at present, however, not fully completed since we are still awaiting improved values for the electron impact destruction rates for SO and O₂ as well as improved excitation rates for some important S lines and an SO band.

2.2 SO₂⁺ Production Rate in the Plasma Torus

Although the SO₂ neutral cloud model has not been completed because of the lack of some of the dissociative chemistry rates, the chemistry for the initial dissociation of SO₂ is sufficiently in tack to proceed with some exploratory model calculations. The SO₂ neutral cloud model has therefore first been used to explore the escape of SO₂ from Io as one possible source for the SO₂⁺ ions measured well inside of Io's orbit (L=5.25) near western elongation by the PLS experiment aboard the Voyager 1 spacecraft during its 1979 flyby of Jupiter (Bagenal 1985).

The spatial distribution and abundance of SO₂ in the plasma torus depend upon the strength of the SO₂ source at Io and its subsequent spacetime lifetime history in plasma torus as the SO₂ cloud moves dynamically away from Io. The various lifetime processes for SO₂ in the plasma torus are summarized in Table 1, where the listed lifetimes are typical values in the hot plasma torus. The dominant lifetime process for SO₂ in the plasma torus is electron impact dissociation, which has a major branch

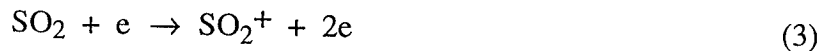


and a minor branch



As discussed by Scherb and Smyth (1993), the lifetime of SO₂ in the plasma torus is, however, highly spacetime dependent because of the oscillation of the plasma torus about the satellite orbital plane and the presence of System III longitude and east-west asymmetries in the plasma torus. The lifetime of SO₂ in the plasma torus at Io's location is illustrated in Figure 1 and can be seen to vary by more than an order of magnitude. For Io near western elongation (i.e., an Io geocentric phase angle of 180°), the SO₂ lifetime varies only moderately with System III longitude and has its minimum value which is smaller than the 0.5 hour contour shown. For Io near eastern elongation (i.e., an Io geocentric phase angle of 90°), the SO₂ lifetime varies considerably with System III longitude and has its maximum value which is larger than the 6 hour contour shown. This highly spacetime dependent lifetime for SO₂ in the plasma torus near Io causes the local abundance of SO₂ in the circumplanetary environment near Io to be highly spacetime dependent as illustrated by Scherb and Smyth (1993) and will hence cause the subsequent production of SO₂⁺ near Io to also be highly spacetime dependent.

For a given time history of the SO₂ cloud abundance near Io, the local abundance of SO₂⁺ ions in the plasma torus will then depend upon the cumulative spacetime history of the local SO₂⁺ production rate and the local SO₂⁺ destruction rate. The two primary sources for production of SO₂⁺ from SO₂ are a minor electron impact ionization branch and a charge exchange reaction with O⁺ ions:





where the relative rates and lifetimes in the hot plasma torus are given in Table 1. Preliminary model calculations for these SO_2^+ production rate will be discussed below. The SO_2^+ destruction rate in the plasma torus is not at present determined, but will hopefully a good estimated will be obtained in the near future by Dr. D. E. Shemansky.

Model calculations for the instantaneous SO_2^+ production rate when Io is east and west of Jupiter have been undertaken. The maximum instantaneous SO_2^+ production rate occurs at the L-shell and System III longitude location of Io, as expected, because the SO_2 abundance is maximum at this position. When Io is west of Jupiter and thus in the hot plasma torus, the calculated L-shell profile for the SO_2^+ production rate is shown in Figure 2. The SO_2^+ production rate in Figure 2 is dominated by electron impact ionization (solid line) at Io's location, but well inside Io's orbit (where the electron temperature in the plasma torus drops to a lower value), electron impact ionization becomes inefficient, and the O^+ charge exchange process (dash-dot line) becomes dominant. The SO_2^+ production rate inside of Io's L-shell position decreases very rapidly since SO_2 is rapidly dissociated in the hot plasma torus very near Io and its supply rate well inside Io's position (near $L=5.25$ where SO_2^+ was detected by the PLS experiment aboard the Voyager 1 spacecraft) is therefore drastically reduced. When Io is east of Jupiter and hence partially in the cold torus, the calculated L-shell profile for the SO_2^+ production rate is, however, significantly different as illustrated in Figure 3. At Io's position, the SO_2^+ production rate is now dominated by the O^+ charge exchange (dash-dot line), and inside Io's position, the SO_2^+ production rate is now larger by much more than an order of magnitude and extends to about $L=4.4$ for the lowest production rate shown. This bulge in the SO_2^+ production rate inward of Io's orbit is caused by the increase in the SO_2 lifetime that occurred approximately 150° earlier in System III longitude (see Figure 1) and that allowed the forward neutral cloud density to be greatly enhanced inside of Io's orbit at the later time.

The results of Figures 2 and 3 and other model calculations not shown suggest that the SO_2^+ abundance detected well inside of Io's orbit ($L=5.25$) near western elongation by the PLS experiment aboard the Voyager 1 spacecraft during its 1979 flyby of Jupiter (Bagenal 1985) is likely produced when Io is east of Jupiter and is then distributed about Jupiter by the corotational motion of the plasma torus. Based on the SO_2 source rate at Io of 8.9×10^{27} molecules s^{-1} adopted here and deduced earlier by Scherb and Smyth (1993) from the analysis of the $[\text{O I}]$ 6300 Å emission near Io, values of the SO_2^+ production rate of about $(0.5 - 1) \times 10^{25}$ ions s^{-1} are produced at $L=5.5$ for Io east of Jupiter. These SO_2^+ ions would then be located in the vicinity

of western elongation near $L=5.3$ and may be able to produce the SO_2^+ abundance detected by the PLS experiment aboard the Voyager 1 if the local SO_2^+ lifetime in the plasma torus is long enough. The determination of the SO_2^+ lifetime in the plasma torus is therefore critical for understanding the presence of SO_2^+ ions in the plasma torus and for providing additional constraints on the SO_2 source rate at Io.

This residence lifetime of SO_2^+ in the plasma torus will depend upon the electron impact recombination rate and the electron impact dissociation rate. An estimate of the former was acquired recently from Dr. D. E. Shemansky, while the latter is not known but is currently under study by him. To develop some insight into the abundance of SO_2^+ inside Io's orbit, the electron impact dissociation lifetime of SO_2 was used as a proxy for the SO_2^+ electron impact dissociation lifetime in the plasma torus. Based on this approach, very preliminary model results for the production, destruction, and accumulation of SO_2^+ are presented in Figure 4 and suggest that an SO_2 source rate at Io of $\sim 10^{28}$ molecules s^{-1} will likely match the Voyager 1 measurement if the SO_2^+ effective average residence time at 5.3 R_J is as long as ~ 100 hours (see Figure Caption). It should be noted that inside of Io's orbit the enhancement factor for the average SO_2^+ residence time relative to its value in the plasma torus equator plane will be particularly sensitive to the radial location in the plasma torus. This follows since the steep temperature gradient inside of Io's orbit (which occurs approximately to the right of the vertical line in Figure 4) dramatically reduces the scale height and hence volume of the plasma about the centrifugal equator so that a new hot latitudinally-oscillating SO_2^+ produced inside of this gradient will spend far less time interacting with the plasma and thus will have a greatly elevated residence lifetime. Hence, one would expect to find SO_2^+ in the plasma torus preferentially inside of Io orbit at ~ 5.3 Jupiter radii as shown in Figure 4, which is just where these ions were measured by the Voyager spacecraft. Further work will await an improved estimate of the SO_2^+ electron impact dissociation lifetime in the plasma torus.

2.3 Ultraviolet Observations for O and S Near Io

To study of the ultraviolet observations for O and S near Io measured in 1992 by the Hubble Space Telescope (HST), such as those published by Clarke et al. (1994) or those acquired but not yet reduced in our collaborative relationship with Dr. M. A. McGrath (see Table 2), we have obtained from Dr. D. E. Shemansky electron impact excitation rates as a function of electron temperature for various ultraviolet lines of O and S. These emission lines are summarized in Table 3, where their excitation rates are given for an electron temperature of 60,000 K. The most relevant emission lines have been updated and/or added to our neutral cloud

models, and model calculations for the brightness and spatial distribution near Io of select emission lines have been undertaken. As an example, the neutral cloud models has been to calculate the spatial distribution of the OI 1304 Å ultraviolet emission near Io. In the calculation, a description for the plasma torus with a nominal east-west electric field ($\epsilon = 0.025$) and an inherent System III asymmetry is adopted. In addition, an isotropic atomic oxygen source at Io's exobase (radius assumed to be 2600 km) of 3.2×10^{27} atoms s^{-1} ejected with a monoenergetic speed of 2.6 km s^{-1} is assumed and corresponds to that source deduced by modeling (see Smyth 1992; Scherb and Smyth 1993) of the O(¹D) 6300 Å emission observation for the neutral oxygen cloud measured in 1980 at larger distances from Io by Brown (1981). Io is chosen to be located at eastern elongation (a geocentric phase angle of 90°) and to have an Io System III longitude of 50°. For these conditions, the model calculation is presented in Figure 5.

In Figure 5, the spatial brightness pattern of the OI 1304 Å emission near Io on the sky plane is shown to distances of $\pm 10,000$ km from the center of the satellite. This distance is comparable to the average satellite Lagrange sphere radius of $\sim 10,600$ km (~ 5.85 satellite radii) within which the gravitational grasp of Io dominates over that of Jupiter. The 1304 Å emission brightness at a distance of 3 satellite radii (5445 km) from Io's center is about 10 Rayleighs. This 10 Rayleighs brightness corresponds to an optically-thin column density of $\sim 2.88 \times 10^{13}$ oxygen atoms cm^{-2} for Io position's in the plasma torus (stated above), where the electron density is ~ 1200 cm^{-3} and where the electron temperature is $\sim 50,000$ K so that the emission rate in Table 3 is reduced by a factor of 0.625. For distances from 3 satellite radii from Io's center to those somewhat beyond than the Lagrange sphere radius, the simple assumed monoenergetic neutral source of 2.6 km s^{-1} (where all atoms completely escape Io) is expected to provides a reasonable estimate of the absolute brightness and its gradient, based on past modeling studies for the sodium cloud. However, within 3 satellite radii of Io's center, the lower velocity components that are ballistic in nature and that will be present in a more realistic description of the neutral flux velocity distribution at the exobase will rapidly begin to dominate the column density and hence emission line brightness. Based upon the more detailed calculations of Smyth and Combi (1996) that successfully simulated the sodium eclipse measurements of Schneider et al. (1991a) from the exobase to distances far beyond the Lagrange sphere by using an appropriately chosen neutral flux velocity distribution at the exobase, it is estimated that the column density of oxygen should increase from ~ 3 satellite radii from Io's center to the satellite exobase by about a factor of 5. If corrected for this flux velocity distribution, the exobase atomic oxygen column density would then be $\sim 1.44 \times 10^{14}$ cm^{-2} , which is about one optical depth for the OI 1304 Å emission line. This exobase oxygen column interestingly also implies that the exobase sodium column density of $\sim 1 \times 10^{12}$ atoms cm^{-2} as determined from groundbased observations by Schneider et

al. (1991a) is $\sim 1\%$ of the oxygen column. This sodium-oxygen abundance ratio is similar to values deduced by other methods.

Measurements obtained from HST of the brightness of various combinations of the multiplets of ultraviolet emission lines of OI and SI very near Io have been published by Clarke et al. (1994) as seen through a $1.4 \text{ arcsec} \times 4.3 \text{ arcsec}$ observing slit centered on the satellite. The combined brightness of the three OI 1304 Å multiplet lines and the six SI 1299 Å lines when Io was in sunlight was estimated to be 1320 Rayleighs if the emission region area is assumed to have a radius of 1.75 satellite radii. For the measurements of Clarke et al. (1994), Io's location in the plasma torus was different, having a geocentric phase angle near 330° and a System III longitude varying from $152\text{--}179^\circ$. For these conditions, the electron density is $\sim 1800 \text{ cm}^{-3}$ and the electron temperature is $\sim 60,000 \text{ K}$. These different plasma torus conditions increase the brightness of the 1304 Å line by a factor of 1.5 and 1.6, respectively. For the interval between 1.75 satellite radii from Io's center (located near of just within the 13 Rayleigh contour) and the exobase (located at ~ 1.4 satellite radii), the average 1304 Å emission brightness is estimated to increase by an additional factor of ~ 4 to account for a flux velocity distribution. The average value for the 1304 Å line would then be approximately $(1.5)(1.6)(4)(\sim 13 \text{ Rayleighs})$ or ~ 125 Rayleighs. By including the other two lines of the 1304 Å multiplet (1302.7 Å and 1306.83 Å , see Table 3), the total oxygen multiplet brightness would then increase by a factor of 3 to ~ 375 Rayleighs. If a comparable column amount of atomic sulfur were also present, its six multiplet lines (see Table 3) would have a combined excitation rate of $25.57 \times 10^{-10} \text{ cm}^3 \text{ s}^{-1}$ compared to that of $13.94 \times 10^{-10} \text{ cm}^3 \text{ s}^{-1}$ for oxygen. The addition of the sulfur multiplet brightness in the observing slit would then provide an enhancement factor of 2.83 so that the total estimated brightness of the OI and SI multiplets together would be ~ 1063 Rayleighs. This value is similar to the 1320 Rayleigh value measured. Simple comparisons of the calculated and measured brightness for other emission lines measured by Clarke et al. (1994) are, however, not in agreement and suggest that other excitation mechanisms (e.g., SO_2 and/or O_2 dissociative excitation by electron impact or aurora emissions at or below the exobase) may be operative as well as errors in the emission rates in Table 3. These matters will be explored more fully in the future once additional reduced HST data becomes available.

2.4 Observations for O(¹D) 6300 Å Emission Near Io

Past and near future projected general information for the synoptic groundbased observations of the O(¹D) 6300 Å oxygen emission brightness near Io acquired at the McMath-Pierce telescope on Kitt Peak using the stellar spectrograph by Dr. F. Scherb (of the University of

Wisconsin-Madison) and colleagues are summarized in Table 4. These observations were obtained with a short integration-time (~ 10 -15 minutes) and with a spatial resolution determined by the seeing conditions. Presently these observations provide a unique and large (over 200 spectra) optical data set for exploration of the abundance of atomic oxygen near Io and its time-variable interaction with the plasma torus. A detailed chronology of the O(¹D) 6300 Å oxygen emission data is summarized in Table 5 for data acquired over the four-years period 1990-1993 and in Table 6 for data acquired in 1994. These observations provide a vital component of our research program for Io established by our collaboration with Dr. Scherb in the past several years and continued in this project.

During 1990-1993, a total of 48 observations were obtained (23 with Io east of Jupiter and 25 with Io west of Jupiter) during 8 nights while in 1994 a total of 131 observations were obtained (72 with Io east of Jupiter and 59 with Io west of Jupiter) during 16 nights. The 1990-1993 observations exhibit a significant brightness variation with Io System III longitude for Io both east and west of Jupiter as shown in Figure 6, although there are obvious and large data gaps in the coverage. The 1994 observations are expected to greatly improve the data gap present in the 1990-1993 observations as illustrated in Figure 7.

2.5 Preliminary Reduction of the O(¹D) 6300 Å Emission Observations

For the O(¹D) 6300 Å oxygen emission observations, Io's disk is centered in the 5.2 arcsec x 5.2 arcsec (i.e., $\sim 10 R_{Io} \times 10 R_{Io}$) field of view of the observing aperture and is not occulted. The bright solar continuum reflected by Io is therefore contained in observed spectra. In order to extract the much dimmer [O I] 6300 Å emission from Io in the observed spectra, the reflected bright solar continuum must be carefully removed. This removal process requires that the reflected solar continuum must be accurately fitted and subtracted from the observed spectra. In the preliminary analysis (Scherb and Smyth 1993) of the 35 observations obtained in 1990-1992, the reflected solar continuum was removed by fitting it with an iterative least-squares computer program using only Gaussians to represent the solar Fraunhofer lines, the terrestrial atmospheric lines, and the [O I] 6300 Å emission feature. It is, however, well known that Voigt functions are much better than Gaussians as models of solar absorption lines and terrestrial absorption lines, but at that time only the iterative least-squares computer program using Gaussians was available. In the interim, a very powerful and effective iterative least-squares computer program using multiple Voigt functions has been developed for Scherb by Dr. R. C. Woodward. An example of the excellent fit of the new Voigt function program to the Kitt Peak Solar Atlas in the vicinity of the an [O I] 6300 Å line is shown in Figure 8. The individual line

parameters obtained in the fit to the Kitt Peak Solar Atlas are then used to model the absorption lines in the Io (and Europa) spectra, including convolution with the echelle spectrometer instrumental profile function. An example of such a fit to a [O I] 6300 Å observation acquired on 5 May 1991 is shown in Figure 9. Observations summarized in Table 4 are presently undergoing a final reduction using the new Voigt fitting program and will soon provide the first complete coverage in Io System III longitude of the 6300 Å emission brightness variation for Io both east and west of Jupiter. The more accurate emission brightness will be particularly important in our modeling studies for its dependence (e.g., sinks, excitation, dissociation) on System III longitude and east-west asymmetries in the plasma torus.

Within this project, however, all of these observations have undergone a preliminary reduction using the new Voigt fitting program to determine their aperture brightness. This preliminary reduction provides a nearly complete coverage in Io System III longitude of the 6300 Å emission brightness variation for Io both east and west of Jupiter. The preliminary results presented here are based upon 85 selected west data points and 64 selected east data points and are shown, respectively, in Figures 10 and 11, where the brightness value is referenced to the disk area of the satellite.

In Figure 10, the 6300 Å emission brightness in the observing aperture for Io west of Jupiter is shown as a function of the Io System III magnetic longitude angle. The angular coverage of the data is good except for a small interval from $\sim 230^\circ$ to 270° . The 6300 Å emission brightness is seen to have extreme maximum and minimum values that differ by about an order of magnitude. On average, however, the brightness varies by about a factor of ~ 2 , with a distinct maximum near 200° and a minimum near 20° . Since the 6300 Å emission rate is not extremely sensitive to temperature, this factor of two suggests that the electron density near 200° may have increased by a factor of about two. The single maximum in the 6300 Å emission brightness located near 200° in Figure 10 verifies the pattern seen with much less angular coverage in the 1990-1992 data set (Scherb and Smyth 1993) and in the 1990-1993 data set in Figure 6 where all east-west data were combined.

In Figure 11, the 6300 Å emission brightness in the observing aperture for Io east of Jupiter is shown as a function of the Io System III magnetic longitude angle. The angular coverage of the data has two noticeable gaps: one for $\sim 30^\circ$ to 60° and one for 160° to 220° . The 6300 Å emission brightness is seen to have extreme maximum and minimum values that differ by almost a factor of four. The absolute brightness and the extreme variation of the east data are therefore less than for the west data. The average brightness, calculated separately for the east

and west data, is, however, interestingly nearly the same because of the large dynamic range in the west data. On average, the east brightness varies by a smaller factor of ~ 1.3 , with a poorly defined minimum near 180° and a poorly defined maximum near 0° . The data gap near 200° is particularly problematical since additional data points might establish either a minimum or maximum here. Additional observations to fill this gap are therefore highly desirable, and firm conclusions about the brightness behavior of the east data must await this information.

2.6 Preliminary Assessment of the O(¹D) 6300 Å Emission Observations

The possibility that the 6300 Å emission brightness near 200° Io System III magnetic longitude has a maximum for the satellite west of Jupiter and a minimum for the satellite east of Jupiter is, however, intriguing. This behavior is reminiscent of the "bite-out" in the sodium cloud south of Io that occurs when the satellite is in the active sector and only when the satellite is near western elongation (Smyth and Goldberg 1996). This behavior appears to be related to the decrease of the small sodium lifetime of by a factor of ~ 2 in the active sector (due to an active sector increased in the electron impact ionization rate by a factor of two) when Io is near western elongation. The sodium-cloud transport time and lifetime are then competitive, hence causing a noticeable reduction in the population of the sodium column brightness. This does not occur for Io near eastern elongation since the east-west electric field alters the plasma torus properties at the orbital position of the satellite so as to increase the absolute sodium lifetime, making it is no longer competitive with the sodium-cloud transport time. This dual dependence for Na suggests that the combined effects of a System III longitude asymmetry and an east-west asymmetry may also play a role in the different behavior of the variation of the 6300 Å emission brightness for Io east and west of Jupiter.

The angular pattern of the 6300 Å emission brightness in Figure 10 for Io west of Jupiter is remarkably similar to the variation of the 6731 Å ion emission line observed in the plasma torus. For the location of the so called "ribbon", the 6731 Å ion emission line brightness measured by Schneider and Trauger (1995) has a minimum near 20° System III magnetic longitude and a maximum near 200° System III magnetic longitude with a corresponding minimum to maximum brightness variation of ~ 3 -4. The "ribbon" is the brightest feature on the centrifugal equator of the plasma torus and is located just within Io's orbit (5.90 satellite radii) by a distance that depends upon the System III magnetic longitude at the east or west location of the plasma torus observation. For observations that ranged in radial distances from ~ 6 to 7.5 satellite radii, the 6731 Å ion emission line brightness measured by Brown (1996) show a broad minimum between 0° and 45° System III longitude and a maximum at 170° System III longitude.

The corresponding minimum to maximum brightness variation is ~ 2 for a radial distances near 6 satellite radii and becomes progressively smaller with increasing distance, essentially vanishing at a radial distance of ~ 7.5 satellite radii for plasma torus observations west of Jupiter. The variation of the 6731 Å ion emission line brightness with System III longitude was shown to be anticorrelated (1) with the parallel ion temperature (Schneider and Trauger 1995), where in the "ribbon" there is a minimum to maximum variation of a factor of ~ 2.5 in the east and ~ 4 in the west and (2) with the perpendicular ion temperature (Brown 1996), where at a distance of ~ 6 satellite radii there is a minimum to maximum variation of a factor of ~ 1.8 in the east and ~ 2.1 in the west. This anticorrelation has lead to the picture that the brightness asymmetry of the plasma torus 6731 Å emission is due to a latitudinally more confined and hence more dense plasma torus centered near 200 System III magnetic longitude (i.e., the electron density has increased by ~ 1.4 -2). The reason for the lower ion temperature near 200 System III magnetic longitude remains, however, unknown. Direct information regarding the variation of the electron temperature and density near 200° , which is more important in understanding the variation of the neutral oxygen 6300 Å emission brightness and the lifetime of sodium, is also unavailable. The variation of the 6300 Å emission brightness may, therefore, provide a direct probe of the plasma torus properties near 200° unless independent and very local excitation mechanisms at and below the satellite exobase (e.g., auroral emission excited by the Birkeland current) dominate the emission brightness in the larger $5.2 \text{ arcsec} \times 5.2 \text{ arcsec}$ observing aperture.

It is interesting to compare the pattern of the 6300 Å emission brightness in Figure 10 to that of the magnetic field strength at Io's northern flux tube footprint in Jupiter's atmosphere. To make this comparison, however, it is first important to understand that the System III longitude angle of the flux tube footprint in Jupiter's atmosphere (call it FPIII longitude), where the current circuit is completed in the ionosphere, is different than the System III longitude angle of Io (call it IoIII longitude) which is located at ~ 6 planetary radii from the planet. The FPIII longitude occurs ahead of Io in its orbit and hence has a smaller System III longitude by an amount $\Delta\phi$:

$$\text{IoIII longitude} = \text{FPIII longitude} + \Delta\phi \quad .$$

Examination of images of the excited H_3^+ near-infrared emission ($3.40 \mu\text{m}$) at the footprint of the Io flux tube in Jupiter's atmosphere by Connerney et al. (1993) provided a value for $\Delta\phi$ of 15 - 20° . As they noted, Goldreich and Lynden-Bell (1969) had earlier indicated that a $\sim 15^\circ$ lead angle of the Io footprint with respect to that of the undisturbed field is what is also needed to symmetrize the observations of the Jovian DAM at 90° and 240° Io phase, relative to an Earth observer at 180° phase. In a more recent paper, Prangé et al. (1996) examined HST images at

Io's footprint for ultraviolet H₂ Lyman band emission (near 1550 Å) and determined a smaller value for $\Delta\phi$ of 7-12.3°. They also noted that the value of the lead angle may be intrinsically variable and may depend upon the spacetime nature of the ion mass-loading rate at Io's position. For our immediate purposes, we adopt a value of 15° for the lead angle. The magnetic field strength at Io's northern flux tube footprint has a peak of >13 gauss at a FPIII longitude of ~150° (IoIII longitude of 165°), falls off rapidly by a factor of ~2 by 240° FPIII longitude (255° IoIII longitude), and remains rather flat in the angular range 240-360° FPIII longitude (255-375° IoIII longitude). The variation of the 6300 Å emission brightness in Figure 10 is therefore remarkably similar to the variation of the magnetic field strength at Io's northern flux tube footprint. The increased magnetic field strength in a sector of Jupiter's ionosphere reduces the Pedersen electrical conductivity in that sector. Such a sector reduction of the Pedersen conductivity was recently reported by Marconi and Smyth (1995) to increase the outward transport rate of the plasma torus in that magnetic sector. Marconi and Smyth (1995) also noted that this increased outward transport rate may possibly provide a basis for the observed cooling of the ions centered near 200° IoIII longitude in the plasma torus. This process might also enhance the flow of plasma into the magnetic sector centered near 200° IoIII longitude both from Jupiter and from the outer impounding plasma as it is convected inward and thereby directly affect the electron impact excitation and ionization rates in this sector. More detailed analysis is required to assess these exciting possibilities.

The analysis by Scherb and Smyth (1993) of the 6300 Å emission brightness data acquired in 1990-1992 identified two excitation processes: (1) electron impact excitation of atomic oxygen and (2) electron impact excitation by molecular dissociation of SO [i.e., $\text{SO} + e \rightarrow \text{S} + \text{O}(^1\text{D}) + e$]. They suggested that the latter mechanism is likely the viable mechanism to explain the large 6300 Å emission brightness and its factor of five System III variability, where SO is either present at the exobase or produced subsequently by dissociation of SO₂. The variation as a function of the Io System III longitude of the 6300 Å emission brightness in Figures 10 and 11 provides additional information that may be used to explore the nature of the excitation mechanism. The 5.2 arcsec x 5.2 arcsec observing aperture is very close to the size of the Lagrange sphere, within which the typical transport times for ballistic and escape orbits are ~1 hour. This transport time is short compared to the combined electron impact and charge exchange lifetime (many hours) of atomic oxygen at Io's position so that, for a constant atomic oxygen source, the abundance of OI in the Lagrange sphere volume should not depend very much upon the position of Io in the plasma torus. If electron impact excitation by the plasma torus is the only mechanism for exciting the 6300 Å emission brightness in the Lagrange sphere, then the variation of this brightness should, approximately, vary as the excitation rate evaluated

at the location of Io in the plasma torus. This variation of the excitation rate at Io's position in the plasma torus has therefore been calculated and is shown in Figure 12.

The plasma torus description adopted in Figure 12 is inherently symmetric in System III longitude and is for an offset and tilted dipole magnetic field in the presence of a nominal ($\epsilon = 0.025$) east-west electric field. The excitation rate, in relative units, is dominated by the variation of the electron density at Io's position in the plasma torus, since the electron temperature does not vary significantly at Io's position and the emission rate for this temperature variation is not on the steep part of its temperature curve. The variation of the excitation rate is, however, very different for Io near western elongation (Io phase angle of 270°) and eastern elongation (Io phase angle of 90°) and is caused by the east-west electric field. Near western elongation, Io's orbital position is shifted outward in the plasma torus and is located well within the warm torus. The maximum excitation rate is therefore centered about 110° and 290° as expected, since the electron density is maximum at the intersection of the satellite orbit plane and the plasma torus centrifugal equator plane. The minimum excitation rate is centered about 20° and 200° as expected, since the electron density is a minimum at the extreme southern and northern latitudes when Io is at its maximum distance from the centrifugal equator plane. This behavior, however, is very different than the observations in Figure 10, where the brightness peaks is near 200° . This difference suggests that the presence of a large System III longitudinal asymmetry peaked near 200° and not just confined to the plasma centrifugal equator plane would be required to alter this situation in the correct direction. Simple enhancements of the plasma torus near 200° which have also been considered to date do not completely correct this situation near western elongation. In Figure 12 near eastern elongation, Io's position in the torus is altered by the east-west electric field so that it moves inward toward the cold torus by a variable distance that depend on the Io System III longitude angle. This causes a minimum in the excitation rate at $\sim 150^\circ$ and a maximum that is centered near $\sim 270^\circ$. The minimum is located near the observed nominal minimum in Figure 11, but the calculated variation of the brightness for Io near eastern elongation is ~ 3 , which is much larger than the nominal variation of ~ 1.3 for the observations. This behavior suggest that the east-west electric field might be responsible for a minimum near 200° , but that the plasma torus must have an inherent System III longitude asymmetry so as to reduce the calculated excitation rate near 270° . Alternatively, this may suggest that the electron impact excitation of atomic oxygen is not the dominant mechanism and that a dissociative excitation mechanism may be more appropriate.

The excitation rates for electron impact dissociation of SO, a one step process [i.e., $\text{SO} + e \rightarrow \text{S} + \text{O}(^1\text{D}) + e$] and of SO₂, a two step process [i.e., $\text{SO}_2 + e \rightarrow \text{SO} + \text{O} + e$; $\text{SO} + e \rightarrow \text{S} +$

$O(^1D) + e]$, are more complex and uncertain. The uncertainty occurs since the electron impact dissociative rate for SO is not well known, the exothermic nature of its liberated $O(^1D)$ is not known, and the delay times and exothermic nature of the two step process for SO_2 are not known. For initial considerations, the lifetime of SO_2 at Io's position in the plasma is calculated and shown in Figure 13 for the same plasma torus description adopted in Figure 12. The lifetime of SO will likely be somewhat similar in nature and will be assumed the same for our immediate considerations. Since SO would approximately fill the observing aperture for these lifetime values, the emission rate would be proportional to the reciprocal of the lifetime. At eastern elongation, this emission rate would then have a minimum at $\sim 150^\circ$ and a maximum centered about $\sim 270^\circ$. At western elongation, this emission rate would have a minimum centered about 20° and 200° and a maximum centered about 110° and 290° . This is the same incorrect calculated pattern noted above for atomic oxygen. Additional calculations for SO involving simple enhancements of the plasma torus electrons near 200° and additional corrections to account for the lack of SO filling the whole observing aperture have also been undertaken, but these additional calculations have not yet been able to correct completely the gap that exists between the simulated and observed System III longitudinal behavior for the 6300 \AA emission brightness. The System III longitudinal behavior of the 6300 \AA emission brightness for the two step process of SO_2 is too complex to pursue in this simple manner. It will require full SO_2 neutral cloud model calculations once a plasma torus description with a proper System III longitude dependence is available.

From the above preliminary consideration three important directives emerge: (1) it is important to develop a more accurate picture for the System III longitude structure of the electrons in the plasma torus, (2) it is important to obtain a more complete Io System III longitude coverage, particularly near 200° , for the OI 6300 \AA emission brightness near Io, and (3) it is important to distinguish the role of plasma torus excitation mechanisms and independent excitation mechanisms that are local to Io's atmosphere. The first directive is ongoing in another project. The second directive will be addressed in the summer of 1996 by F. Scherb who plans to obtain at the McMath-Pierce telescope at Kitt Peak two weeks of OI 6300 \AA emission measurements for Io. The third directive will be pursued in future comparisons of (1) HST observations for high spatial resolution scans across Io of OI and SI ultraviolet emission lines acquired only for very limited System III longitudes and (2) groundbased observations for the lower spatial resolution 6300 \AA emission brightness in updated versions of Figures 10 and 11 acquired for an almost complete System III longitude coverage. The lack of availability of the final reduced observations for the HST and groundbased data sets has, to date, hampered this very interesting comparison.

III. Na FAMILY

3.1 Review of the 1987 Observations for the Sodium Emissions Near Io

The 110 sodium emission spectra acquired from Catalina Observatory over 5 nights in October of 1987 by N. M. Schneider are summarized in Table 7. In Table 7, the data file number, the UT date, the observational midpoint time, and the corresponding Io geocentric orbital longitude and Io System III magnetic longitude are given. The slit for the observation was 40 arcsec long with Io located at the midpoint and was ~ 1 arcsec wide. In Table 7, the orientation of the long dimension of the observing slit is indicated and occurs north-south for only 7 spectra and east-west for 103 spectra. The midpoint of the slit was centered on Io for all 7 north-south spectra. For the 103 east-west spectra, the midpoint position of the slit was varied vertically among three locations designated by (1) "N" when the slit was positioned 5 arcsec (~ 10 satellite radii) north of Io for 20 spectra, (2) "Io" when the slit was centered on Io for 64 spectra, and (3) "S" when the slit was positioned 5 arcsec south of Io for 19 spectra. In Table 8, the observations are subdivided into 63 observations for Io east of Jupiter and 47 observations for Io west of Jupiter. It can be seen in Table 8 that observations were acquired (1) on October 13 and 15 when Io was only east of Jupiter, (2) on October 16 when Io was only west of Jupiter, and (3) on October 17 and 18 when Io was both east and west of Jupiter.

All the 110 spectra have been reduced. Three data products for one east-west spectra acquired when Io was in the field of view are illustrated in Figure 14. As a function of the distance along the east-west observing slit, the three data products for the D_1 and D_2 lines are (1) the brightness profile, (2) the velocity FWHM of emission profile, and (3) the velocity centroid of the emission profile relative to Io. The variation as a function of the geocentric phase angle of these profiles for the first and third of the data products is shown in Figures 15 and 16, respectively. The brightness profile in Figure 15 can be seen to decrease as Io moves away from eastern or western elongation as expected for an excitation mechanism of solar resonance scattering. The analysis of the 1987 emission observations has only been initiated in this project and will be continued in a new three-year follow-on project. The emphasis in this project has been directed to the completion of the analysis of the earlier 1985 emission data and its comparison to other sodium data. This analysis and comparison is presented in Smyth and Combi (1996), which is attached in the Appendix. Part of the background review work required in this comparison is presented in the following section.

3.2 Review of the Velocity Dispersion of Sodium Atoms at Io's Exobase

An extensive review for the analysis of sodium observations near Io and its orbit was undertaken in order to ascertain the implications and constraints that these observations have imposed on the velocity dispersion and source strength of sodium at the satellite exobase. The results of the review are summarized in Table 9 and have been incorporated in Smyth and Combi (1996). In Table 9, the analysis of sodium observations are divided into three spatial regions: (1) the Io corona located within the Lagrange sphere of Io, (2) the neutral cloud located beyond the Lagrange sphere and near Io's orbit, and (3) the north-south oscillating directional features that are observed to trail Io in its orbit. Analysis of sodium in the Io corona can be, furthermore, subdivided into early observations of the average intensity in a 8 arcsec x 3 arcsec slit centered on Io reported by Bergstralh et al. (1975, 1977) that indicated an east-west intensity asymmetry of ~ 1.25 and later observations of a more spatially detailed one-dimensional column density profiles within the Lagrange sphere reported by Schneider et al. (1987, 1991a). A summary of the review for the three spatial regions is given below.

3.2.1 Corona: East-West Intensity Asymmetry:

Studies of Smyth (1983) based upon sodium atoms ejected monoenergetically from Io's exobase established that small scale structures in the D-line intensity profile observed as a function of the Io geocentric phase angle could arise from modulation of the atoms escape rate from Io caused by the action of solar radiation acceleration in the D-lines. These modulations occur primarily for exobase speeds of 2.0 km/s and 2.1 km/s, which are near the escape-speed threshold of the Lagrange sphere. Studies of Smyth and Combi (1987a) showed that the main reason for the east-west intensity asymmetry was, however, an east-west electric field which altered the plasma properties at Io's orbit so as to increase the sodium lifetime and hence sodium abundance when Io was preferentially east of Jupiter. More complex modeling studies of Smyth and Combi (1988b) were undertaken to constrain the flux velocity dispersion for sodium at Io's exobase by simultaneously fitting the average east-west intensity asymmetry and the general spatial morphology of the forward sodium cloud, located on a much larger spatial scale well beyond the Lagrange sphere. These studies showed that the sodium ejection speed at the exobase required to fit the east-west intensity asymmetry is double-valued, having a lower value ≤ 1 km/s and a higher value in the range 2.6-3.65 km/s. For a Maxwell-Boltzmann flux distribution, the lower and higher speed values were 0.71 km/s ($T=460$ K) and 3.65 km/s ($T=12,300$ K). Neither value was, however, suitable for properly populating the forward cloud. The lower value produces essentially all ballistic atoms orbits which could not populate the forward cloud, while the higher value was significantly larger than the nominal ~ 2.6 km/s characteristic velocity

required to reproduce the proper spatial morphology for the forward cloud. For the higher and more nominal thermal exobase temperatures in the range ~ 1000 - 2000 K, the calculated east-west intensity ratio was much higher than the observed value with the atoms still contributing primarily to the corona density and far too deficient in energy to contribute any significant sodium to the forward cloud. For the preferred ($\alpha=7/3$) modified-sputtering distribution of Smyth and Combi (1988b) with a source strength of $\sim 2 \times 10^{26}$ atoms/s, the lower and higher speed values were ≤ 0.5 km/s and ~ 2.9 km/s, respectively, with the latter value being preferred because of its closer proximity to the ~ 2.6 km/s characteristic velocity for the forward cloud. Interestingly, however, it is actually the lower value which has recently been shown by Smyth and Combi (1995, 1996) to reproduce the correct one-dimensional profile for the sodium column density within the Lagrange sphere.

3.2.2 Corona: Column Density Profile:

In modeling studies, Smyth and Combi (1987b, c) determined that typical forward cloud brightness data for the sodium cloud could be properly simulated well beyond the Lagrange sphere radius of ~ 5.81 Io radii by an average sodium source of $\sim 1 \times 10^{26}$ atoms/s ejected monoenergetically from Io's exobase with a characteristic velocity of ~ 2.6 km/s. They also established that this same sodium source reproduced the column density profile of Schneider et al. (1987) within the Lagrange sphere up to a radius of ~ 3.5 Io radii. For a radius smaller than ~ 3.5 Io radii, the calculated profile was lower than the observed profile, indicating that lower velocity (ballistic and escape) components are required, in addition, in a more realistic flux velocity dispersion. A similar behavior for the calculated column density profile, with an even more dramatic departure from the observed profile both inside and outside the Lagrange sphere, was also later shown by a model of Ip (1990) who assumed an exobase speed of 3 km/s but did not include the gravity of Jupiter so as to properly include the near zero escape speed conditions at the Lagrange sphere. Adopting for the sodium atoms at the exobase a simple ($V_b = 0$) classical sputtering energy distribution with a low energy cut-off and also excluding Jupiter's gravity, McGrath (1988) modeled the column density in the Lagrange sphere region and produced a profile with a slope slightly less steep than the observation for an infinite sodium lifetime and a slope somewhat steeper than the observation for a sodium lifetime of 3 hr. Adopting a Maxwell-Boltzmann flux distribution, assuming an infinite sodium lifetime, and similarly also excluding Jupiter's gravity, Summers et al. (1989) and Schneider et al. (1991a) modeled the column density within the Lagrange sphere region and produced a profile that reasonably well matched the observed profile for an exobase temperature, respectively, of 1000 K based on the partial eclipse data set (Schneider et al. 1987) and of 1500 K based on the

complete eclipse data set (Schneider 1988). Although these different flux velocity distributions reasonably fit the observations within the Lagrange sphere, it is clear from the earlier studies of Smyth and Combi (1988b) that the Maxwell-Boltzmann distributions are energetically inappropriate and that the more energetically promising sputtering distribution cannot be explored adequately near or beyond the Lagrange sphere radius without properly including the gravity of Jupiter, solar radiation acceleration, and the spacetime variable lifetime of sodium in the plasma torus.

3.2.3 Sodium Cloud

The early studies of the sodium cloud were general in nature probing its poorly documented spatial and angular extent about the planet. An excitation mechanism for the cloud of solar resonance scattering was established by Bergstralh et al. (1975). Based upon this mechanism and limited angular extent data determined by slit-averaged intensity data, Carlson et al. (1975) undertook monoenergetic (3.5 km/s) model calculations and estimated that the sodium cloud lifetime (assumed to be spatially uniform) was an order of magnitude faster than photoionization and was likely determined by electron impact ionization by the (then very poorly characterized) plasma in planetary magnetosphere. This general picture was confirmed by more extensive model calculations performed by Fang et al. (1976) to investigate the structure of the cloud in the long-lived limit and by Smyth and McElroy (1977) to explore the time evolution and two-dimensional nature of the cloud for exobase velocities near or just above the escape speed from the Lagrange sphere. The acquisition of sodium cloud images in late 1976 and early 1977 brought this subject into dramatic focus. By adopting a classical sputtering flux distribution that peaked at 4 km/s, Matson et al. (1978) successfully modeled a one-dimensional brightness profile, extending from Io in the forward cloud to ~ 80 Io radii and in the trailing cloud to ~ 40 Io radii. The one-dimensional brightness profile was derived from a cloud image by averaging it in the north-south direction. The analysis by Smyth and McElroy (1978) of the much larger sodium cloud image data set (Murcray 1978) indicated that the forward cloud could be characterized by an exobase ejection speed of ~ 2.6 km/s and that its changing intensity pattern could be understood as the projection on the sky plane of a changing viewing perspective of an approximately steady state cloud as Io moved on its orbit around Jupiter. In both modeling efforts, the observed predominance of the forward sodium cloud over the trailing cloud was accomplished both by limiting the exobase source area to a hemisphere (see Table 9) and by limiting the spatially uniform lifetime so as to dynamically select sodium atom orbits that would primarily populate the forward cloud. Modeling studies of Macy and Trafton (1980) of the radial and vertical cloud structure on larger spatial scales indicated that dispersion speeds with values at least up to 13 km/s were required to explain a variety of different observations. Additional

model studies (Smyth 1979, 1983) showed that the east-west orbital asymmetry of Goldberg et al. (1978), i.e., the lack of cloud mirror symmetry when the sodium cloud is compared at diametrically opposite Io orbital phase angles east and west of Jupiter, was due to the perturbing action of solar radiation acceleration on the sodium atom orbits. Adopting a one-dimensional radial dependent sodium lifetime in the plasma torus based upon limited Voyager spacecraft encounter information in 1979 and retaining their asymmetric exobase source for a classical sputtering distribution with a peak velocity at 4 km/s, Goldberg et al. (1980) successfully modeled a one-dimensional brightness profile derived from a sodium cloud image acquired during the Voyager 1 encounter period for distances extending from Io in the forward cloud to ~ 80 Io radii and in the trailing cloud to ~ 30 Io radii. Later modeling by Smyth and Combi (1988b) using a more accurate two-dimensional spacetime-dependent lifetime for sodium in the plasma torus demonstrated that the predominant forward cloud was caused by the highly radially dependent sink for sodium that exists in the plasma torus inside and outside of Io's orbit. Their exobase source strength for the sodium cloud was $\sim 2 \times 10^{26}$ atoms/s.

3.2.4 Directional Feature

Pilcher et al. (1984) using their observations acquired in 1980 and 1981 for weaker D-line emissions in the trailing portion of the sodium cloud discovered an elongated feature in the sodium brightness distribution that on the sky plane was directed away from Jupiter and was inclined sometimes to the north and sometimes to the south of the satellite's orbital plane. The north/south direction of the feature was shown to be correlated with Io's magnetic longitude and suggested a formation mechanism involving the oscillating plasma torus. Modeling analysis by Pilcher et al. indicated that the feature resulted from a high-velocity (~ 20 km/s) sodium source combined with the oscillating neutral sodium sink provided by the plasma torus. The directionality of the high-velocity source was at near right angles to Io's orbital motion with a source strength required on the outer satellite hemisphere of $\sim 1 \times 10^{26}$ atoms/s. The peculiar directionality of the source was investigated by Sieveka and Johnson (1984) who concluded that it was produced by direct collisional ejection of neutral sodium from the exosphere by the corotating plasma flow past Io, as exhibited in their discussion of more appropriate interaction potentials for these collisional processes. More recent modeling by Smyth and Combi (1991) of the sodium magneto-nebula or zenocorona, detected out to 400-500 planetary radii from Jupiter by Mendillo et al. (1990), showed that it required a two component source: a high-velocity (~ 20 km/s) exobase sodium source of $\sim 1 \times 10^{26}$ atoms/s for the spatial distribution nearer the planet and an even higher-velocity (~ 57 km/s) exobase sodium source of $\sim 2 \times 10^{26}$ atoms/s for the spatial distribution further from the planet. Both source components, however, were based on ion-neutral charge exchange processes in Io's exosphere and were therefore composed of a

tangential speed to Io's orbit at Io's position plus an isotropic Maxwell-Boltzmann distribution with a most probable speed of about one-third of the tangential speed in the Jupiter frame (i.e., one-third of ~ 37 and ~ 74 km/s, respectively). The lower component is therefore symbolically denoted in the Io frame by 20 ± 12 km/s in Table 9. Very recently, successful modeling of the directional features has also been reported by Wilson and Schneider (1995) who have deduced a similar lower component source denoted in Table 9 by 20 ± 10 -20 km/s, where the isotropic portion of their source may be variable in magnitude.

3.2 Sodium Model for a Molecular Ion Source

In the paper by Smyth and Combi (1991), the comet model of Combi and Smyth (1988 a,b) was modified for the purpose of constructing a model of the sodium zenocorona (or magneto-nebula) which was measured to distances of 400-500 Jupiter radii (R_J) from the planet by Mendillo et al. (1990). In that model, sodium atom trajectories emanating from Io were calculated in a heliocentric frame, accounting for solar gravity and solar radiation pressure explicitly. The gravitational attraction of Jupiter was accounted for only implicitly through the approximate subtraction of the gravitational escape energy from Jupiter at Io's distance. This model was useful for exploring the very large scale "coma-like" shape of the sodium cloud which is apparent on the order of an astronomical unit or $\sim 2000 R_J$. For modeling the wide-field images of Mendillo et al., covering distances out to about 500 R_J , the effect of solar radiation pressure on the observed shape of the sodium cloud is, however, small.

In this project, we are interested not only in the wide-field type of image data of Mendillo et al. but also in more near-Jupiter images, covering distances more typically on a scale of $\sim 10 R_J$. Models developed in older work successfully addressed the low and intermediate speed sodium, 1-25 km/s, and account for the circular-restricted three-body problem (e.g., Smyth 1979, Pilcher et al. 1984, Smyth and Combi 1988 a,b) between the sodium atom, Jupiter, and Io. This model is most useful for the low speed sodium (1-10 km/s) that is generally responsible for the forward (Region B) cloud. For intermediate and high speed sodium (10-100 km/s), both in the vicinity of Io ($\sim 10 R_J$ from Jupiter) and out to the region of the measured zenocorona ($\sim 500 R_J$ from Jupiter), it was judged that a model which accounted explicitly for the two-body problem between Jupiter and a sodium atom ejected from Io, was more than adequate for tracking the trajectories of atoms. This simpler method yields a computational tractable basis for studying in a physically detailed manner (1) the large scale zenocorona, (2) the so-called molecular-ion source of sodium responsible for the jet of sodium emitted from the region just ahead of Io (Schneider et al. 1991b), and (3) the relative strengths of the two.

The core of a new two-body model (sodium atom and Jupiter), based on algorithms and code contained in former comet and zenocorona models, has been constructed and is now undergoing testing. The standard iterative inversions of Kepler's laws, as described by Combi and Smyth (1988a,b) in connection with the orbit of the cometary nucleus, were employed. This is in contrast to the fourth-order Runge-Kutta scheme employed in the previous zenocorona model of Smyth and Combi (1991). The previous zenocorona model results can be faithfully reproduced, in fact improved, with many more particles (much reduced statistical noise) in a small fraction of the computational time, using the two-body model.

A simple preliminary version of a molecular-ion jet source for sodium atoms has also been added to the two-body model. The scenario for the model was adopted from the picture described by Schneider et al. (1991b) of sodium-bearing ions (NaX^+) being picked up at Io's position, in the frame of the corotating dipole magnetic field. The ions are accelerated to corotational speed and considered to decay through the process of dissociative recombination, producing neutral sodium atoms with some branching ratio. In this preliminary version of the model, the decay rate is considered to be simply exponential, similarly to Schneider et al. The NaX^+ ions bounce up and down along a magnetic field line about the centrifugal equator as described by Cummings et al. (1980). Using this model a credible reproduction of the spatial morphology of the sodium molecular jet as seen in the images presented by Schneider et al. (1991b) is obtained and shown in Figure 17. The next step in this process is to replace the simple time constant in the exponentially decaying molecular-ion source and the simple dipole-field bounce oscillations, with a space-time dependent lifetime for the decaying molecular-ion source in a physically realistic description of the plasma torus. The dissociative recombination rate must by nature be dependent on plasma density and temperature. With such a model, we can begin to explore the effects on the sodium jet of variations in the source rate produced by more realistic processes such as the east-west electric field, higher order magnetic field descriptions, and System III longitudinal asymmetries in the plasma torus. Similar processes can effect the direct charge-exchange component of fast sodium as well.

IV. NEUTRAL CLOUDS FOR THE OTHER GALILEAN SATELLITES

The possibility that Europa has an interesting atmosphere and that this atmosphere can play a noticeable role in the structure of the planetary magnetosphere has evolved rapidly, particularly in the past year. From the analysis of Voyager plasma data (Bagenal 1989; Bagenal

et al. 1992), it was suggested that Europa may supply a possible weak source of oxygen ions for Jupiter's magnetosphere beyond 7.25 planetary radii, which is beyond Io's orbit (5.90 planetary radii) and near Europa's orbit (9.40). Even more definitively, the recent discovery of atomic oxygen in the atmosphere of Europa from HST measurements (Hall et al. 1995) has suggested that O₂ is present in the satellite atmosphere (< 900 km altitude or < 0.57 satellite radii altitude) produced from breakup of water molecules liberated from its icy surface. The preliminary investigations of Hall et al. indicated that the observed atomic oxygen is excited primarily by electron impact dissociation of an O₂ column density of $\sim 1.5 \times 10^{15}$ molecules cm⁻². Very recently near Europa, atomic sodium emissions in the optical D₁ and D₂ lines excited by solar resonance scattering have been discovered from groundbased measurements (Brown 1995; Brown and Hill 1995) to distances at least as large as ~ 25 satellite radii from the satellite. The Lagrange sphere radius of Europa, where the satellite's gravitational field dominates over Jupiter's gravitational field is, however, only 8.7 satellite radii. Europa therefore has an extended sodium corona (radius < 8.7 satellite radii) and also an escaping sodium source (radius > 8.7 satellite radii) which forms a sodium cloud that should be concentrated near the satellite's orbit. Brown and Hill suggest that a likely source for the atomic sodium is sodium ions from the planetary magnetosphere that are captured and neutralized by Europa's surface and then sputtered from the surface by the dominant oxygen and sulfur ions in the magnetosphere. Europa therefore appears to have a bound and escaping atmosphere like Io with neutral clouds that likely form at least partial gas tori about Jupiter.

The presence of bound atmospheres, extended coronae, and neutral gas clouds for at least one Galilean satellite other than Io is therefore a reality. We have therefore undertaken in the past quarter a very preliminary assessment of the general situation for all Galilean satellites and a more specific preliminary assessment for Europa. A number of physical and orbital parameters for the four Galilean satellites and for Jupiter have therefore been calculated and updated and are summarized in Table 10. These parameters are important in determining the orbital dynamics of neutral atoms near the satellite and in the larger circumplanetary environment. From Io outward, the average Lagrange radius (within which the satellite's gravity dominates over the planet's gravity and within which a bound corona may exist) is given in Table 10, respectively, in satellite radii as 5.90, 8.70, 12.05 and 20.90. In the sodium observations of Brown and Hill (1995) for Europa, there is an apparent change in the slope of the deduced column density profile at about 8.7 satellite radii which may be a signature that indicates the boundary between a bound component and an escaping component of the atmosphere. A similar slope change exists for the sodium atmosphere of Io. From Io outward, the two-body escape speeds for the four Galilean satellites are 2.563 km/s, 2.020 km/s, 2.741 km/s and 2.446 km/s, respectively. It is therefore

somewhat easier for a nonthermal gas source to escape from Europa than from the other three Galilean satellites. For atomic sodium and potassium, the escape of the gas from the Lagrange sphere will furthermore be modulated, as a function of the geocentric satellite phase angle, by the presence of the solar radiation acceleration in the D-lines. This modulation was demonstrated earlier for escaping sodium at Io (Smyth 1983). Note, however, that the maximum solar radiation acceleration measured as a percentage of Jupiter's gravity at the four satellite orbits increases from Io outward, having, respectively, values of 1.76%, 3.90%, 8.69%, and 22.0% for sodium and 1.73%, 4.34%, 10.9% and 32.6% for potassium. Relative to Io, therefore, the modulation by solar radiation acceleration of the escape rates of Na and K from the satellite Lagrange spheres will vary progressively more dramatically for the outer three Galilean satellites. In addition, the modification by solar radiation acceleration of the orbital dynamics and hence spatial morphology of the neutral sodium and potassium gas clouds for each satellite in the circumplanetary space beyond the Lagrange sphere will increase dramatically as one moves outward from Io. The interplay of these dynamical changes and the spacetime variable lifetime of sodium and potassium within the plasma torus will further add to the complexity of the three-dimensional distribution of sodium and potassium. The situation for atomic oxygen will be less complex since solar radiation acceleration is not important. Investigations of current and future sodium observations for Europa therefore provide a new and direct link to studying the structure of this satellite atmosphere, the escape of its gases, and the role of these gases in supplying additional plasma sources for the planetary magnetosphere.

REFERENCES

- Bagenal, F. (1985) Plasma Conditions Inside of Io's Orbit: Voyager Measurements, JGR **90**, 311-324.
- Bagenal, F. (1989) Torus-Magnetosphere Coupling, in *Time Variable Phenomena in the Jovian System*, NASA SP-494, pp. 196-210.
- Bagenal, F., Shemansky, D. E., McNutt Jr., R. L., Schreier, R. and Eviatar, A. (1992) The Abundance of O^{++} in the Jovian Magnetosphere, Geophys. Res. Letts. **19**, 79-82.
- Bergstralh, J. T., Matson, D. L. and Johnson, T. V. (1975) Sodium D-Line Emission from Io: Synoptic Observations from Table Mountain Observatory, Astrophys. J. Lett. **195**, L-131-L135.
- Bergstralh, J. T., Young, J. W., Matson, D. L. and Johnson, T. V. (1977) Sodium D-Line Emission from Io: A Second Year of Synoptic Observation from Table Mountain Observatory, Astrophys. J. Lett. **211**, L51-L55.
- Brown, M. E. (1995) Discovery of Sodium Around Europa BAAS **27**, 1161.
- Brown, M. E. (1996) Periodicities in the Io Plasma Torus, J. Geophys. Res., in press.
- Brown, M. E. and Hill, R. X. (1995) Discovery of an Extended Sodium Corona Around Europa, preprint, 1995.
- Brown, R. A. (1981) The Jupiter Hot Plasma Torus: Observed Electron Temperature and Energy Flow, Ap. J. **244**, 1072-1080.
- Carlson, R. W. (1995) private communication.
- Carlson, R. W., Matson, D. L. and Johnson, T. V. (1975) Electron Impact Ionization of Io's Sodium Emission Cloud, GRL **2**, 469-472.
- Clarke, J. T., Ajello, J., Luhmann, J. Schneider, N. and Kanik, I. (1994) Hubble Space Telescope UV Spectral Observations of Io Passing into Eclipse, J. Geophys. Res. **99**, 8387-8402.
- Combi, M. R. and Smyth, W. H. (1988a) Monte Carlo Particle Trajectory Models for Neutral Cometary Gases. I. Models and Equations, Ap. J. **327**, 1026-1043.
- Combi, M. R. and Smyth, W. H. (1988b) Monte Carlo Particle Trajectory Models for Neutral Cometary Gases. II. The Spatial Morphology of the Lyman - α Coma, Ap. J., **327**, 1044-1059.
- Connerney, J. E. P., Baron, R., Satoh, T. and Owens, T. (1993) Images of Excited H_3^+ at the Foot of the Io Flux Tube in Jupiter's Atmosphere, Science **262**, 1035-1038.
- Cummings, W. D., Dessler, A. J., Hill, T. W. (1980) Latitudinal Oscillations of Plasma within the Io Torus, J. Geophys. Res. **85**, 2108-2114.
- Fang, T.-M., Smyth, W. H. and McElroy, M. B. (1976) The Distribution of Long-Lived Gas Clouds Emitted by Satellites in the Outer Solar System, Planet. Space Sci. **25**, 577-588.

- Goldberg, B. A., Carlson, R. W., Matson, D. L., and Johnson, T. V. (1978) A New Asymmetry in Io's Sodium Cloud, BAAS, 10, 579.
- Goldberg, B. A., Yu. Mekler, R. W. Carlson, T. V. Johnson, and D. L. Matson (1980) Io's Sodium Emission Cloud and the Voyager 1 Encounter. Icarus 44, 305-317.
- Goldreich, P. and Lynden-Bell, D. (1969) Io, a Jovian Unipolar Inductor, Ap. J. 156, 59-78.
- Hall, D. T. Strobel, D. F., Feldman, P. D. McGrath, M. A. and Weaver, H. A. (1995) Detection of an Oxygen Atmosphere on Jupiter's Moon Europa, Nature 373, 677-679.
- Ip, W.-H. (1990) Neutral Gas-Plasma Interaction: The Case of the Plasma Torus, Adv. Space Res. 10, 15-23.
- Macy, W. W., Jr. and Trafton, L. M. (1980) The Distribution of Sodium in Io's Cloud: Implications. Icarus 41, 131-141.
- Marconi, M. L. and Smyth, W. H. (1995) Iogenic Plasma Source: Corotational Lag, Energy, and Transport in the Plasma Torus, BAAS 27, 1154.
- Matson, D. L., Goldberg, B. A., Johnson, T. V. and Carlson R. W. (1978) Images of Io's Sodium Cloud. Science 199, 531-533.
- Mendillo, M., Baumgardner, J., Flynn, B. and Hughes, W.J. (1990) The Extended Sodium Nebula of Jupiter, Nature, 348, 312-314.
- McGrath, M. A. (1988) Ion Bombardment of Io and Mercury, Ph.D. Thesis, Dept. of Astronomy, University of Virginia.
- Morgan, J.S. (1985a) Temporal and Spatial Variations in the Io Torus, Icarus 62, 389-414.
- Morgan, J.S. (1985b) Models of the Io Torus, Icarus 63, 243-265.
- Murcray, F. J. (1978) Observations of Io's Sodium Cloud, Ph. D. Thesis, Dept. of Physics, Harvard University.
- Murcray, F. J. and R. M. Goody (1978). Pictures of the Io Sodium Cloud. Ap. J. 226, 327-335.
- Prangé, R., Rego, D., Southwood, D., Zarka, P., Miller, S. and Ip, W. (1996) Rapid Energy Dissipation and Variability of the Io-Jupiter Electrodynamical Circuit, Nature 379, 323-325.
- Pilcher, C. B., Smyth, W. H., Combi, M. R., and Fertel, J. H. (1984) Io's Sodium Directional Features: Evidence for a Magnetospheric-Wind-Driven Gas Escape Mechanism, Ap. J. 287, 427-444.
- Scherb, F. and Smyth, W. H. (1993) Variability of [O I] $\lambda 300\text{-}\text{\AA}$ Emission Near Io JGR 98, 18729-18736.
- Schneider, N. M. (1988) Sodium in Io's Extended Atmosphere. Ph.D. Thesis, Department of Planetary Sciences, University of Arizona.

- Schneider, N. M., Hunten, D. M., Wells, W. K., and Trafton, L. M. (1987) Eclipse Measurements of Io's Sodium Atmosphere, Science **238**, 55-58.
- Schneider, N. M., Hunten, D. M., Wells, W. K., Schultz, A. B. and Fink, U. (1991a) The Structure of Io's Corona, Ap. J. **368**, 298-315.
- Schneider, N. M. and Trauger, J. T. (1995) The Structure of the Io Torus. Ap.J., **450**, 450-462.
- Schneider, N. M., Trauger, J. T., Wilson, J. K., Brown, D. I., Evans, R. W. and Shemansky, D. E. (1991b) Molecular Origin of Io's Fast Sodium, Science **253**, 1394-1397.
- Sieveka, E. M. and Johnson, R. E. (1984) Ejection of Atoms and Molecules from Io by Plasma-Ion Impact, Ap. J. **287**, 418-426.
- Smyth, W. H. (1979) Io's Sodium Cloud: Explanation of the East-West Asymmetries. Ap. J., **234**, 1148-1153.
- Smyth, W. H. (1983) Io's Sodium Cloud: Explanation of the East-West Asymmetries. II. Ap. J., **264**, 708-725.
- Smyth, W. H. (1992) Neutral Cloud Distribution in the Jovian System, Adv. in Space Res. **12**, 337-346.
- Smyth, W. H., and Combi, M. R. (1987a) Correlating East-West Asymmetries in the Jovian Magnetosphere and the Io Sodium Cloud, Geophys. Res. Lett. **14**, 973-976.
- Smyth, W. H. and Combi, M. R. (1987b) Time Variability of the Sodium Cloud, poster paper at the international conference "Time-Variable Phenomena in the Jovian System," Flagstaff, AZ August 25-27.
- Smyth, W. H. and Combi, M. R. (1987c) Nature of Io's Atmosphere and its Interaction with the Planetary Magnetosphere. BAAS, **19**, 855.
- Smyth, W. H., and Combi, M. R. (1988a) A General Model for Io's Neutral Gas Cloud. I. Mathematical Description, Ap. J. Supp. **66**, 397-411.
- Smyth, W. H., and Combi, M. R. (1988b) A General Model for Io's Neutral Gas Cloud. II. Application to the Sodium Cloud, Ap. J. **328**, 888-918.
- Smyth, W. H. and Combi, M. R. (1991) The Sodium Zenocorona, J. Geophys. Res., **96**, 22711-22727.
- Smyth, W. H. and Combi, M. R. (1995) A Consistent Sodium Flux-Speed Distribution at Io's Exobase, BAAS **27**, 1155.
- Smyth, W. H. and Combi, M. R. (1996) Io's Sodium Exosphere and Spatially Extended Cloud: A Consistent Flux Speed Distribution, Icarus, submitted.
- Smyth, W. H. and Goldberg, B. A. (1996) Correlating System III Longitudinal Asymmetries in the Jovian Magnetosphere and the Io Sodium Cloud, paper in preparation.
- Smyth, W. H., and M. B. McElroy (1977) The Sodium and Hydrogen Gas Clouds of Io, Planet. Space Sci. **25**, 415-431.

Smyth, W. H., and M. B. McElroy (1978) Io's Sodium Cloud: Comparison of Models and Two-Dimensional Images, Astrophys. J. 226, 336-346.

Summers, M. E., Strobel, D. F., Yung, Y. L., Trauger, J. T. and Mills, F. (1989) The Structure of Io's Thermal Corona and Implications for Atmospheric Escape. Ap. J. 343, 468-480.

Wilson, J. K. and Schneider, N. M. (1995) Io's Sodium Directional Feature: Evidence for Ionospheric Rip-off, BAAS 27, 1154.

Table 1
SO₂ Loss Processes in the Plasma Torus Near Io

		<u>Relative Rate (%)</u>	<u>Lifetime (hr)</u>
1.	SO ₂ + e → SO + O + e	72.55	1.4
	S + O ₂ + e	14.51	7.2
2.	SO ₂ + e → SO ₂ ⁺ + 2e	4.44	24
	SO ⁺ + O + 2e	1.15	91
	S ⁺ + O ₂ + 2e	0.33	310
	SO + O ⁺ + 2e	0.03	3300
3.	SO ₂ + O ⁺ → SO ₂ ⁺ + O	2.03	52
4.	SO ₂ + O ⁺⁺ → (SO ₂ ⁺) [*] + (O ⁺) [*]	0.04	≥ 2700
5.	SO ₂ + S ⁺ → SO ₂ ⁺ + S(³ P)	0.01	≥ 19000
6.	SO ₂ + S ⁺⁺ → (SO ₂ ⁺) [*] + (S ⁺) [*]	1.27	≥ 82
7.	SO ₂ + S ⁺⁺⁺ → SO ₂ ⁺ + S ⁺⁺ (³ P)		
	SO ₂ ⁺ + S ⁺⁺ (¹ D)		
	SO ₂ ⁺ + S ⁺⁺ (¹ S)	0.18	580
	SO ₂ ⁺ + S ⁺⁺ (³ D ₀)		
	SO ₂ ⁺ + S ⁺		
8.	SO ₂ + hν → SO + O	2.64	40
	S + O ₂	0.80	130
	SO ₂ ⁺ + e	0.02	6800

Table 2
Hubble Space Telescope Observations of Io
March and May 1992

Faint Object Spectrograph (FOS) far- and near-UV spectra of Io

March 22, 1992

1.4" x 4.3" aperture centered on Io

1 G130H (1150-1600 Å) spectrum

1 G190H (1575-2330 Å) spectrum

Spatial and spectral resolution are determined by the size of the emitting region. Detection of OI and SI emissions from Io and SO₂ gas absorption bands from 1900-2300 Å in the albedo, and ion emissions from the torus.

Good S/N: SI 1900, SIII 1713/1729. Problems with scattered light in the short-wavelength data, which is low S/N for neutral emissions and probably only marginally useful.

Faint Object Spectrograph (FOS) spatial scans of Io

March 20, 1992

1.4" x 4.3" aperture

2 scans of 8" length [supposed to be centered on Io]

1 with G130H (1150-1600Å)

1 with G190H (1575-2330Å)

These observations missed Io the first time due to failed guide star acquisition. They were repeated on May 16, 1992 successfully (see below). However, these data have good torus lines, and could yield some information on the radial distribution of torus emission, ion density, etc.

High Resolution Spectrograph spatial scans of Io

March 18, 1992

2" x 2" aperture

2 scans of 8" length centered on Io

1 with G160M (1800-1840 Å) centered on SI 1800 Å multiplet

1 with G160M (1280-1315 Å) centered on SI/OI 1300 Å multiplets

Some preliminary work has been done on these data and find that the 1800 Å emission is peaked in a region of ~1.7" (in remarkable agreement with the FOS spectra results mentioned above). Not clear whether emission is detected outside this region, but think 1820 is there. Can probably see the optical thickness effects. Data are noisy. Time-tagged with 10 s integration times. 1300 will probably be useless due to Earth contamination, but not clear. Line width of 1800 line can be used to see if the 1300 Å data makes sense.

FOS spatial scans of Io

May 16, 1992

1.4" x 4.3" aperture

2 scans of 8" length centered on Io

1 with G130H (1150-1600Å)

1 with G190H (1575-2330Å)

Will help determine spatial structure of the OI and SI Io UV emissions, and possibly of the SO₂ gas absorption bands.

Table 3
Atomic Oxygen and Sulfur Line Emission Rates

Species	Vacuum Wavelength (Å)	Transition Array	Multiplet	Emission Rate* (cm ³ sec ⁻¹)
OI	1304 multiplet	2s ² 2p ³ (4S ⁰)3s	3S ⁰	
	1302.70	(J=1 → 2)		4.63 x 10 ⁻¹⁰
	1304.86	(J=1 → 1)		4.65 x 10 ⁻¹⁰
	1306.83	(J=1 → 0)		4.66 x 10 ⁻¹⁰
OI	1356 multiplet	2s ² 2p ³ (4S ⁰)3s	5S ⁰	
	1355.60	(J=2 → 2)		1.30 x 10 ⁻¹⁰
	1358.52	(J=2 → 1)		1.30 x 10 ⁻¹⁰
	1359.79	(J=2 → 0)		1.31 x 10 ⁻¹⁰
OI	6302.11	2s ² 2p ⁴ (1D → 3P)		2.99 x 10 ⁻⁹
OI	5578.89	2s ² 2p ⁴ (1S → 1D)		2.09 x 10 ⁻⁹
SI	1299 multiplet	3s ² 3p ³ (2P)4s''	3p ⁰	
	1295.65	(J=2 → 2)		6.26 x 10 ⁻¹⁰
	1296.17	(J=1 → 2)		2.08 x 10 ⁻¹⁰
	1302.33	(J=2 → 1)		3.53 x 10 ⁻¹⁰
	1302.86	(J=1 → 1)		2.12 x 10 ⁻¹⁰
	1303.10	(J=0 → 1)		2.83 x 10 ⁻¹⁰
	1305.88	(J=1 → 0)		8.75 x 10 ⁻¹⁰
SI	1256 multiplet	3s ² 3p ³ (4S) 6d	3D ⁰	
	1247.10	(J=1 → 2)		5.39 x 10 ⁻¹³
	1247.13	(J=2 → 2)		8.10 x 10 ⁻¹²
	1247.15	(J=3 → 2)		4.53 x 10 ⁻¹¹
	1253.29	(J=1 → 1)		1.37 x 10 ⁻¹¹
	1253.32	(J=2 → 1)		4.12 x 10 ⁻¹¹
	1256.09	(J=1 → 0)		5.67 x 10 ⁻¹¹
SI	1389 multiplet	3s ¹ 3p ⁵	3p ⁰	
	1381.55	(J=1 → 2)		2.57 x 10 ⁻¹²
	1385.51	(J=0 → 1)		3.48 x 10 ⁻¹⁰
	1388.43	(J=2 → 2)		4.46 x 10 ⁻¹²
	1389.15	(J=1 → 1)		1.39 x 10 ⁻¹²
	1392.59	(J=1 → 0)		1.28 x 10 ⁻¹²
	1396.11	(J=2 → 1)		7.90 x 10 ⁻¹²

Table 3 (continued)

Species	Vacuum Wavelength (Å)	Transition Array	Multiplet	Emission Rate* (cm ³ sec ⁻¹)
SI	1429 multiplet	$3s^2 3p^3 (4S)3d$	$3D^0$	
	1425.03	(J=3 → 2)		2.59×10^{-9}
	1425.19	(J=2 → 2)		4.63×10^{-10}
	1425.22	(J=1 → 2)		3.08×10^{-11}
	1433.28	(J=2 → 1)		2.35×10^{-9}
	1433.31	(J=1 → 1)		7.84×10^{-10}
	1436.97	(J=1 → 0)		3.26×10^{-9}
SI	1479 multiplet	$3s^2 3p^3 (2D)4s'$	$3D^0$	
	1474.00	(J=3 → 2)		5.50×10^{-10}
	1474.38	(J=2 → 2)		9.85×10^{-11}
	1474.57	(J=1 → 2)		6.58×10^{-12}
	1483.04	(J=2 → 1)		5.01×10^{-10}
	1483.23	(J=1 → 1)		1.67×10^{-10}
	1487.15	(J=1 → 0)		6.95×10^{-10}
SI	1814 multiplet	$3s^2 3p^3 (4S)4s$	$3S^0$	
	1807.31	(J=1 → 2)		2.85×10^{-9}
	1820.34	(J=1 → 1)		2.91×10^{-9}
	1826.24	(J=1 → 0)		3.04×10^{-9}
SI	1900 multiplet	$3s^2 3p^3 (4S)4$	$5S^0$	
	1900.29	(J=2 → 2)		8.73×10^{-10}
	1914.70	(J=2 → 1)		8.81×10^{-10}
	1921.23	(J=2 → 0)		8.85×10^{-10}
SI	10820 multiplet	$3s^2 3p^4 (1D \rightarrow 3P)$		
	10824.10	(J=2 → 2)		8.39×10^{-9}
	11308.96	(J=2 → 1)		8.47×10^{-9}
	11540.69	(J=2 → 0)		8.50×10^{-9}

* Emission rate determined for an electron temperature of 60,000 K.

Table 4

GROUND BASED OBSERVATIONS OF [O I] 6300 Å EMISSION NEAR IO

Observational Program:

- PI: F. Scherb
- McMath-Pierce Telescope on Kitt Peak
- High-Resolution Solar-Stellar Spectrograph (resolving power $\sim 1.2 \times 10^5$)
- Integration Time: 10-15 minutes
- Viewing Aperture: 5.2 arcsec x 5.2 arcsec (centered on Io)

Synoptic Observation Chronology:

<u>Year</u>	<u>Number of East Observations</u>	<u>Number of West Observations</u>	<u>Reference</u>
1990-1992	12	23	Scherb & Smyth 1993a
1993	10	3	(work in progress)
1994	82	82	(work in progress)
	<hr/>	<hr/>	
Total	104	108	

Future Observational Program:

<u>Year</u>	<u>Program Elements</u>
1996	<ul style="list-style-type: none"> • Continue Synoptic Observations (June 23-July 7)

TABLE 5. 1990 - 1993 OBSERVATIONS OF [O I] 6300 Å EMISSION NEAR IO

<u>Date</u>	<u>Start Time</u> <u>(UT)</u>	<u>Io Phase</u> <u>Angle (deg)</u>	<u>Io System III</u> <u>Angle (deg)</u>
1990 February 17	0427	319.61	133.29
	0437	321.01	137.93
	0452	323.12	144.89
	0502	324.52	149.53
	0513	326.06	154.63
	0702	341.38	205.21
1991 February 11	0655	278.18	271.92
	0708	280.02	277.94
	0722	281.99	284.43
	0733	283.54	289.54
	0743	284.95	294.17
	0754	286.50	299.27
	0809	288.61	306.23
	0820	290.16	311.33
	0830	291.56	315.97
1991 May 5	0424	226.58	122.88
	0435	228.13	127.98
	0446	229.67	133.08
	0457	231.22	138.18
	0509	232.91	143.75
	0520	234.45	148.85
	0621	243.02	177.15
	0639	245.55	185.51
1991 May 6	0441	71.70	78.39
	0452	73.26	83.48
	0503	74.82	88.56
	0534	79.23	102.89
	0545	80.80	107.97
	0556	82.36	113.05
	0607	83.93	118.14
	0618	85.49	123.22
1992 February 29	1023	90.28	247.81
	1034	91.83	252.92
	1046	93.52	258.48
	1147	102.12	286.76
1993 May 8	0955	174.38	292.22
1993 May 19	0842	243.45	34.88
	0858	245.72	42.27
1993 May 20	0422	49.88	221.78
	0436	51.84	228.28
	0452	54.08	235.71
	0509	56.47	243.61
	0525	58.71	251.03
	0540	60.82	258.00
	0556	63.06	265.42
	0621	66.57	277.03
	0744	78.22	315.55
	0803	80.89	324.37

TABLE 6. 1994 OBSERVATIONS OF [O I] 6300 Å EMISSION NEAR IO

<u>Date</u>	<u>Start Time</u> <u>(UT)</u>	<u>Io Phase</u> <u>Angle (deg)</u>	<u>Io System III</u> <u>Angle (deg)</u>	
July 12	0457	122.62	62.96	
	0508	124.17	68.06	
	0519	125.72	73.16	
	0530	127.27	78.26	
	0541	128.82	83.36	
	0551	130.23	87.99	
	0607	132.49	95.41	
	0623	134.76	102.82	
	0639	137.00	110.24	
	0656	139.40	118.11	
July 13	0344	316.63	335.25	
	0359	318.76	342.20	
	0415	321.02	349.61	
	0431	323.28	357.02	
	0447	325.54	4.43	
	0503	327.80	11.84	
	0519	330.06	19.25	
	0540	333.02	28.98	
	0601	335.99	38.71	
July 14	0326	156.62	274.82	
	0345	159.31	283.61	
	0401	161.58	291.02	
	0417	163.84	298.42	
July 15	0431	10.01	251.14	in eclipse
	0450	12.68	259.96	in eclipse
	0506	14.92	267.38	in eclipse
	0522	17.17	274.81	in eclipse
	0539	19.55	282.70	
	0604	23.06	294.30	
	0620	25.31	301.73	
	0636	27.55	309.16	
July 16	0355	207.84	181.97	
July 19	0335	95.16	13.81	
	0351	97.40	21.23	
	0407	99.65	28.65	
	0423	101.90	36.07	
	0438	104.01	43.03	
	0454	106.26	50.45	
	0510	108.51	57.88	
	0526	110.76	63.30	
	0542	113.01	72.71	
	0557	115.12	79.67	
	0613	117.38	87.09	
	0629	119.63	94.51	
	0645	121.88	101.92	

<u>Date</u>	<u>Start Time (UT)</u>	<u>Io Phase Angle (deg)</u>	<u>Io System III Angle (deg)</u>
July 20	0414	304.86	338.08
	0430	307.12	345.49
	0446	309.39	352.90
	0501	311.51	359.84
	0517	313.77	7.25
	0533	316.03	14.66
	0549	318.30	22.07
	0604	320.41	29.02
	0620	322.67	36.43
	0636	324.93	43.84
	0651	327.05	50.79
July 21	0417	147.80	287.36
	0433	150.06	294.77
	0539	159.41	325.32
July 27	0349	285.14	315.46
	0436	291.81	337.21
	0452	294.07	344.61
	0507	296.20	351.55
	0523	298.46	358.96
	0539	300.73	6.37
	0555	302.99	13.77
	0608	304.83	19.79
July 28	0304	121.33	242.46
	0320	123.58	249.88
	0342	126.69	260.07
	0358	128.94	267.48
	0413	131.06	274.43
	0429	133.32	281.84
	0445	135.58	289.25
	0501	137.85	296.66
	0541	143.50	315.19
	0557	145.77	322.59
	0614	148.17	330.46
July 30	0251	166.35	130.34
	0311	169.19	139.59
August 1	0343	220.86	48.02
	0416	225.56	63.26
	0432	227.84	70.66
	0448	230.12	78.05
	0503	232.25	84.98
	0519	234.53	92.37
	0535	236.81	99.77
	0551	239.08	107.16
	0606	241.22	114.09
	0622	243.50	121.49

<u>Date</u>	<u>Start Time</u> <u>(UT)</u>	<u>Io Phase</u> <u>Angle (deg)</u>	<u>Io System III</u> <u>Angle (deg)</u>
August 2	0306	58.85	338.03
	0325	61.52	346.85
	0341	63.76	354.28
	0356	65.86	1.25
	0412	68.11	8.67
	0428	70.35	16.10
	0444	72.59	23.53
	0459	74.70	30.49
	0515	76.94	37.91
	0531	79.19	45.34
	0546	81.30	52.30
	0602	83.54	59.72
August 3	0304	262.43	283.62
	0320	264.70	291.01
	0335	266.83	297.95
	0351	269.11	305.35
	0407	271.38	312.75
	0423	273.65	320.15
	0438	275.78	327.09
	0454	278.05	334.49
	0510	280.31	341.89
	0526	282.58	349.23
	0541	284.71	356.23
	0557	286.98	3.64
August 5	0251	307.49	171.43
	0307	309.75	178.84
	0323	312.01	186.25
	0339	314.27	193.67
	0403	317.66	204.79
	0433	321.88	218.69
	0525	329.21	242.79
	0541	331.46	250.21
August 6	0254	150.41	120.69
	0309	152.54	127.63
	0325	154.80	135.03
	0341	157.07	142.43
	0357	159.34	149.83
	0413	161.61	157.23
	0428	163.74	164.17
	0444	166.01	171.57

Table 7

1987 Io Sodium Emission Spectra from Catalina Observatory

File FR87I	UT Date	Decimal Midpoint (hrs)	Io Orbital Longitude	Io Magnetic Longitude	Slit Orientation	Slit Location
232	13 Oct	5.38	40.2	84.7	E/W	Io
236	13 Oct	7.48	58.0	143.1	E/W	Io
237	13 Oct	7.67	59.6	148.2	E/W	N
238	13 Oct	7.88	61.4	154.2	E/W	Io
239	13 Oct	8.07	63.0	159.3	E/W	S
247	13 Oct	9.77	77.4	206.6	E/W	Io
248	13 Oct	9.97	79.1	212.1	E/W	N
249	13 Oct	10.17	80.8	217.7	E/W	Io
250	13 Oct	10.35	82.3	222.8	E/W	S
258	13 Oct	11.67	93.5	259.4	E/W	Io
259	13 Oct	11.83	94.9	264.0	E/W	Io
338	15 Oct	5.18	85.9	333.1	E/W	Io
339	15 Oct	5.37	87.4	338.2	E/W	N
340	15 Oct	5.57	89.1	343.8	E/W	Io
341	15 Oct	5.78	91.0	349.8	E/W	S
350	15 Oct	6.47	96.8	8.8	E/W	Io
356	15 Oct	6.98	101.2	23.2	E/W	Io
358	15 Oct	7.32	104.0	32.4	E/W	N
360	15 Oct	7.58	106.3	39.8	E/W	Io
361	15 Oct	7.78	107.9	45.4	E/W	S
371	15 Oct	9.00	118.3	79.2	E/W	Io
372	15 Oct	9.18	119.8	84.3	E/W	N
378	15 Oct	9.58	123.2	95.4	E/W	Io
379	15 Oct	9.77	124.8	100.5	E/W	S
382	15 Oct	10.15	128.0	111.2	E/W	Io
383	15 Oct	10.42	130.3	118.6	E/W	N
387	15 Oct	10.68	132.6	126.0	E/W	Io
388	15 Oct	11.07	135.8	136.6	E/W	Io
389	15 Oct	11.30	137.8	143.1	E/W	S
390	15 Oct	11.52	139.6	149.2	E/W	N
394	15 Oct	11.80	142.0	157.0	E/W	Io
397	15 Oct	12.37	146.8	172.8	E/W	Io
466	16 Oct	3.68	276.7	29.3	E/W	Io
474	16 Oct	4.53	283.9	52.9	E/W	Io
475	16 Oct	4.70	285.3	57.5	E/W	N
476	16 Oct	4.90	287.0	63.1	E/W	Io
477	16 Oct	5.08	288.5	68.2	E/W	S
482	16 Oct	5.43	291.5	77.9	E/W	Io
488	16 Oct	6.13	297.4	97.4	E/W	Io
489	16 Oct	6.32	299.0	102.5	E/W	N
490	16 Oct	6.50	300.6	107.6	E/W	Io
491	16 Oct	6.87	303.7	117.8	E/W	S
496	16 Oct	7.07	305.4	123.3	E/W	Io
497	16 Oct	7.25	306.9	128.4	E/W	N
498	16 Oct	7.43	308.5	133.5	E/W	Io
499	16 Oct	7.60	309.9	138.1	E/W	S
503	16 Oct	7.92	312.6	146.9	N/S	Io
504	16 Oct	8.15	314.6	153.4	E/W	Io
509	16 Oct	8.35	316.3	159.0	E/W	Io
510	16 Oct	8.85	320.5	172.9	E/W	N
514	16 Oct	9.18	323.3	182.2	E/W	Io
515	16 Oct	9.22	323.6	183.1	E/W	Io

Table 7 (Continued)

516	16 Oct	9.42	325.3	188.6	E/W	S
520	16 Oct	9.75	328.1	197.9	E/W	Io
521	16 Oct	9.93	329.7	203.0	E/W	N
524	16 Oct	10.28	332.7	212.7	E/W	Io
525	16 Oct	10.47	334.2	217.8	E/W	Io
526	16 Oct	10.68	336.1	223.8	E/W	S
530	16 Oct	11.47	342.7	245.6	N/S	Io
533	16 Oct	11.75	345.1	253.5	E/W	Io
534	16 Oct	11.95	346.8	259.0	E/W	Io
535	16 Oct	12.13	348.4	264.1	E/W	Io
536	16 Oct	12.45	351.1	272.9	E/W	Io
562	17 Oct	3.92	122.3	342.7	E/W	Io
565	17 Oct	4.45	126.9	357.6	E/W	N
566	17 Oct	4.63	128.4	2.7	E/W	Io
567	17 Oct	4.82	130.0	7.8	E/W	S
571	17 Oct	5.10	132.4	15.6	N/S	Io
574	17 Oct	5.52	135.9	27.2	E/W	Io
575	17 Oct	5.70	137.5	32.3	E/W	N
579	17 Oct	6.05	140.4	42.0	E/W	Io
580	17 Oct	6.25	142.1	47.6	E/W	S
581	17 Oct	6.43	143.7	52.7	E/W	Io
583	17 Oct	6.68	145.8	59.6	E/W	N
588	17 Oct	6.98	148.4	68.0	E/W	Io
589	17 Oct	7.27	150.8	75.8	E/W	S
591	17 Oct	7.48	152.6	81.9	N/S	Io
595	17 Oct	7.95	156.6	94.8	E/W	Io
597	17 Oct	8.25	159.1	103.2	E/W	N
598	17 Oct	8.43	160.7	108.3	E/W	Io
600	17 Oct	8.72	163.1	116.2	E/W	S
605	17 Oct	9.03	165.8	125.0	E/W	Io
626	17 Oct	11.90	190.1	204.6	E/W	Io
627	17 Oct	12.13	192.1	211.1	E/W	Io
628	17 Oct	12.35	193.9	217.1	E/W	Io
629	17 Oct	12.55	195.6	222.7	E/W	Io
663	18 Oct	3.95	326.1	290.8	E/W	Io
664	18 Oct	4.17	328.0	296.9	E/W	N
665	18 Oct	4.37	329.7	302.4	E/W	Io
666	18 Oct	4.53	331.1	307.0	E/W	S
669	18 Oct	4.82	333.5	314.9	N/S	Io
674	18 Oct	5.30	337.6	328.4	E/W	Io
675	18 Oct	5.52	339.4	334.4	E/W	N
676	18 Oct	5.68	340.8	339.0	E/W	Io
677	18 Oct	5.90	342.7	345.0	E/W	S
682	18 Oct	6.33	346.3	357.1	N/S	Io
685	18 Oct	6.63	348.9	5.4	E/W	Io
686	18 Oct	6.80	350.3	10.0	E/W	Io
701	18 Oct	9.12	10.0	74.4	E/W	Io
702	18 Oct	9.32	11.7	80.0	E/W	Io
704	18 Oct	9.57	13.8	86.9	E/W	Io
709	18 Oct	10.57	22.3	114.7	E/W	Io
710	18 Oct	10.77	24.0	120.3	E/W	N
712	18 Oct	11.00	25.9	126.8	E/W	Io
713	18 Oct	11.20	27.6	132.3	E/W	S
716	18 Oct	11.50	30.2	140.7	N/S	Io
719	18 Oct	11.75	32.3	147.6	E/W	Io
720	18 Oct	11.93	33.9	152.7	E/W	N
721	18 Oct	12.12	35.4	157.8	E/W	Io
722	18 Oct	12.30	37.0	162.9	E/W	S

Table 8

GROUND BASED OBSERVATIONS OF SODIUM D-LINE EMISSIONS NEAR IO

Observational Program:

- Observer: N. M. Schneider
- Catalina Observatory
- High-Resolution LPL Echelle Spectrograph/CCD ($\sim 3 \text{ km s}^{-1}$ FWHM)
- Integration Time: 10 minutes
- Viewing Slit: ± 40 arcsec east-west (centered on Io)
- Io Emission Spectra Were Acquired in October 1987
- All D₁ And D₂ Observations Have Been Reduced

Observation Chronology:

<u>Date</u>	<u>Number of East Observations</u>	<u>Number of West Observations</u>	<u>Total No. of Observations</u>
13 Oct	11	0	11
15 Oct	21	0	21
16 Oct	0	31	31
17 Oct	19	4	23
18 Oct	12	12	24
	<hr/>	<hr/>	<hr/>
Total	63	47	110

Table 9. Summary of Modeling Studies for the Spatial Distribution of Sodium Near Io and its Orbit

Spatial Region	Topic Studied	Sodium Source								Sodium Lifetime		Orbital Dynamics			Reference
		Mono-energetic Atom Ejection	Maxwell-Boltzman Flux Distribution	Cascade Flux Speed Distribution						Plasma Torus Description	Lifetime (hrs)	Io's Mass Included	Jupiter's Mass Included	Radiation Pressure Included	
				Speed (km s ⁻¹)	T (K)	V _{peak} (km s ⁻¹)	α	V _b (km s ⁻¹)	V _{peak} (km s ⁻¹)						
I. Corona	e-w intensity asymmetry ^b	2.0-2.6	-	-	-	-	-	-	isotropic	cut-off	20	yes	yes	yes	Smyth 1983
	e-w intensity asymmetry ^b	2.6	-	-	-	-	-	-	isotropic	2-D	variable	yes	yes	yes	Smyth and Combi 1987a
	e-w intensity asymmetry ^b	-	460; 12,300	0.71; 3.65	7/3	<0.4; 2.2	<0.5; 2.9	46.6	band, isotropic	2-D	variable	yes	yes	yes	Smyth and Combi 1988
	column-density profile ^c	2.6	-	-	-	-	-	-	isotropic	2-D	variable	yes	yes	yes	Smyth and Combi 1987b,c
	column-density profile ^c	-	-	-	3	0 ^d	-	∞	isotropic	cut-off	3, ∞	yes	no	no	McGrath 1988
	column-density profile ^c	-	1000	1.04	-	-	-	-	isotropic	uniform	∞	yes	no	no	Summers et al. 1989
	column-density profile ^c	3.0	-	-	-	-	-	-	isotropic	uniform	?	yes	no	no	Ip 1990
	column-density profile ^e	-	1500	1.28	-	-	-	-	isotropic	uniform	∞	yes	no	no	Schneider et al. 1991
II. Cloud	general spatial nature	3.5	-	-	-	-	-	-	isotropic	uniform	30, 47	yes	yes	no	Carlson et al. 1975
	general spatial nature	-	5000	2.3	-	-	-	-	isotropic	long-lived limit	-	no	yes	no	Fang et al. 1976
	evolution and 2-D nature	2, 3	-	-	-	-	-	-	isotropic	cut-off	50	yes	yes	no	Smyth and McElroy 1977
	1-D brightness morphology ^f	-	-	-	3	4	4	∞	I-L hemisphere ^g	uniform	28	yes	yes	no	Matson et al. 1978
	2-D brightness morphology ^h	2.6, 3	-	-	-	-	-	-	I, I-T hemisphere ⁱ	cut-off	15, 20	yes	yes	no	Smyth and McElroy 1978
	e-w orbital asymmetry ^j	2.6	-	-	-	-	-	-	I-T hemisphere ⁱ	cut-off	20	yes	yes	yes	Smyth 1979
	radial and vertical structure	(3.5,7.9,11,13) ^k	-	-	-	-	-	-	I hemisphere	uniform	56	no	yes	no	Macy and Trafton 1980
	1-D brightness morphology	-	-	-	3 ^l	4 ^l	4 ^l	∞ ^l	I-L hemisphere ^l	1-D	variable	yes	yes	no	Goldberg et al. 1980
	e-w orbital asymmetry	2.6	-	-	-	-	-	-	I hemisphere	cut-off	20	yes	yes	yes	Smyth 1983
	2-D brightness morphology	2.6	-	-	-	-	-	-	band, isotropic	2-D	variable	yes	yes	yes	Smyth and Combi 1988
III. Directional Feature	spacetime structure ^m	~20	-	-	-	-	-	-	O, ~L to Io's motion	2-D	variable	yes	yes	yes	Pilcher et al. 1984
	collision cross sections	-	-	-	3	0 ⁿ	-	-	~L to Io's motion	-	-	-	-	-	Sieveka and Johnson 1984
	nearer zenocorona structure	-	-	~20± 12P	-	-	-	-	tangential ± isotropic	photoionization	~400 hr	no	no; Sun yes	yes	Smyth and Combi 1991
	spacetime structure	-	-	20± 10-20 ^q	-	-	-	-	tangential ± isotropic	none	∞	no	yes	no	Wilson and Schneider 1995

^a regarding Io's exobase, L=leading, I=inner, T=trailing, O=outer.^b east-west intensity asymmetry data of Bergstralh et al. (1975, 1977).^c early (i.e., partial) Na eclipse data set from Schneider et al. (1987).^d used cut-off energy: $E_{min} \leq E < \infty$; $E_{min} = k T_{exobase}$; $T_{exobase} = 1500$ K (i.e. a 1.04 km s⁻¹ cut-off speed).^e complete eclipse data set from Schneider (1988) and Schneider et al. (1991).^f two sodium cloud images of Matson et al. (1978).^g I-L hemisphere centered 30° longitude (0° longitude facing Jupiter, 90° longitude is the leading point in the orbit).^h fifty-six sodium cloud images of Murcray (1978) and Murcray and Goody (1978).ⁱ I-T hemisphere centered on -40° longitude.^j east-west orbital asymmetry data of Goldberg et al. (1978).^k velocity components equally weighted.^l distribution parameters from Carlson (1995); I-L hemisphere centered on 45° longitude.^m from images of Pilcher et al. (1984).ⁿ used cut-off energy of 0.5 eV (i.e., Na cut-off speed of 2.0 km s⁻¹).^p tangential speed to Io's orbit at Io position ± most probable speed of an isotropic Maxwell-Boltzmann.^q tangential speed to Io's orbit at Io position ± most probable speed of an isotropic Gaussian.

Table 10. Physical and Orbital Parameters for the Galilean Satellites and Jupiter

	<u>Io</u>	<u>Europa</u>	<u>Ganymede</u>	<u>Callisto</u>	<u>Jupiter</u>
Radius (km)	1815	1569	2631	2400	71398 ^a
GM Value (km ³ s ⁻²)	5961	3201	9887	7181	126686537
Secondary Body/Primary Body Mass Ratio	4.705x10 ⁻⁵	2.527x10 ⁻⁵	7.804x10 ⁻⁵	5.668x10 ⁻⁵	9.547907x10 ⁻⁴
Mass ^b (10 ²² kg)	8.934	4.798	14.82	10.76	189877.9
Mass Density ^b (g cm ⁻³)	3.567	2.965	1.942	1.859	1.33 ^a
Surface Gravity (cm s ⁻²)	181.0	130.0	142.8	124.7	2485.2
Two-Body Escape Speed (km s ⁻¹)	2.563	2.020	2.741	2.446	59.57
Lagrange Sphere Radius ^c (km, [radius ^d])	10,550 [5.81]	13,650 [8.70]	31,700 [12.05]	50,150 [20.90]	53,140,440 [744.28]
Orbital Period (d, [hr], <yr>)	1.769137786 [42.46]	3.551181041 [85.23]	7.15455296 [171.71]	16.6890184 [400.54]	<11.86223>
Orbital Semimajor Axis (10 ⁵ km, [Radius ^d])	4.216 [5.90]	6.709 [9.40]	10.70 [14.99]	18.83 [26.37]	7783.284 [1118.29]
Orbital Speed (km s ⁻¹)	17.33	13.74	10.88	8.205	13.064
Orbital Inclination to Primary Body Equator (deg)	0.04	0.47	0.21	0.51	1.305
System III Period (hr, [ang. freq. in deg/hr])	12.9526 [27.79]	11.2330 [32.05]	10.5338 [34.18]	10.1771 [35.37]	9.92492 [36.27]
System III Corotation Speed (km s ⁻¹)	56.81	104.2	177.3	322.9	-
Corotational Electric Field ^e at Satellite Orbit (mV m ⁻¹)	154	60.9	23.9	7.73	-
Corotational Electric Field ^e at Satellite (mV m ⁻¹)	118	53.8	22.5	7.53	-
Maximum Potential Across the Satellite (kV)	428	169	119	36.2	-
Primary Body Gravitational Acceleration (cm s ⁻²)	71.27	28.15	11.07	3.573	-
Na Solar Radiation Acceleration ^f (cm s ⁻² , [% primary ^g])	1.25 [1.76]	1.10 [3.90]	0.961 [8.69]	0.787 [22.0]	-
K Solar Radiation Acceleration ^f (cm s ⁻² , [% primary ^g])	1.23 [1.73]	1.22 [4.34]	1.20 [10.9]	1.17 [32.6]	-

^a Equatorial radius; polar radius is smaller (93.5%) and the mass density reflects this non-spherical shape.

^b Value of the Constant of Gravity adopted: $G=6.672 \times 10^{-20} \text{ km}^3 \text{ kg}^{-1} \text{ s}^{-2}$.

^c Average value for the L₁ and L₂ colinear Lagrange points.

^d "radius" denotes radius of the secondary (smaller) body; "Radius" denotes radius of the primary (larger) body.

^e Based on an O₄ model main magnetic-dipole moment of 4.28 gauss (R_J)³, where R_J is the equatorial radius of Jupiter.

^f Maximum solar radiation acceleration calculated for the satellite at the elongation point of its orbit.

^g Percent based on the primary-body gravitational acceleration evaluated at the orbit of the secondary body.

FIGURE CAPTIONS

Figure 1. SO₂ Lifetime at Io's Location in the Plasma Torus. The lifetime, given in units of hours, is calculated for Voyager 1 plasma conditions with a tilted-offset dipole planetary magnetic field, a nominal east-west electric field, and an inherently asymmetric plasma torus in System III longitude similar to that observed by Morgan (1985 a,b).

Figure 2. SO₂⁺ Production Rate in the Plasma Torus. The L-shell profile for the production rate of SO₂⁺ from SO₂ is shown for electron impact ionization (solid line) and for O⁺ charge exchange (dashed-dot line) for an Io geocentric phase angle of 270° and an Io System III longitude angle of 230°. A SO₂ source strength of 8.9×10^{27} molecules s⁻¹ and an isotropic flux from the Io exobase (2600 km radius) with an initial speed of 2.6 km s⁻¹ were assumed.

Figure 3. SO₂⁺ Production Rate in the Plasma Torus. The L-shell profile for the production rate of SO₂⁺ from SO₂ is shown for electron impact ionization (solid line) and for O⁺ charge exchange (dashed-dot line) for an Io geocentric phase angle of 90° and an Io System III longitude angle of 300°. A SO₂ source strength of 8.9×10^{27} molecules s⁻¹ and an isotropic flux from the Io exobase (2600 km radius) with an initial speed of 2.6 km s⁻¹ were assumed.

Figure 4. Abundance of the SO₂⁺ Ion in the Plasma Torus. Three L-shell profiles for the abundance of SO₂⁺ are shown by the solid lines. These profiles were constructed by taking the product of the same SO₂⁺ production rate profile (shape shown by the dashed line, but absolute value enhanced by a factor of 1000 to ease the comparison) with different residence lifetimes for SO₂⁺. The instantaneous production rate was calculated using the single-species SO₂ neutral cloud with a source rate of 8.9×10^{27} sec⁻¹ (Scherb and Smyth 1993) for Io at eastern elongation and at a System III longitude of 200°. The SO₂⁺ residence lifetime used includes electron recombination (which dominates for $L < 5.2$) and electron impact dissociation which dominates for $L > 5.2$), the latter which is not known and has been approximated by the electron impact dissociation lifetime for SO₂. The abundance profile extending from L-shell values of about 4 to 7 is for the minimum residence lifetime of SO₂⁺ in the centrifugal plane. The other two abundance profiles are ten times (10 X) and one hundred times (100 X) the minimum abundance profile, but are shown only for $L < 5.4$, inside of which the plasma torus is confined $\sim \pm 0.11$ planetary radii of the centrifugal equator (because of a rapid decrease in the ion temperature) and inside of which the SO₂⁺ ion at 200° System III longitude is mostly above or below the plasma and hence has a much larger effective residence lifetime. A rough estimate shows that the scaling factor for the minimum abundance profile may be in the range of ~ 20 -110 which is large enough to match or exceed the SO₂⁺ abundance (+ symbol) estimated from PLS data acquired by the Voyager 1, given the uncertainties in the absolute radial position as determined by the east-west electric field. This suggests that the SO₂⁺ abundance measured by Voyager 1 could be produced by the escape of SO₂ from Io if the residence time of SO₂⁺ in the torus were ~ 100 hr.

Figure 5. Atomic Oxygen 1304 Å Emission Near Io. A model calculation for the 1304 Å brightness in Rayleighs is shown near Io for an isotropic oxygen source of 3.2×10^{27} atoms s⁻¹ ejected at 2.6 km s⁻¹ from an assumed satellite exobase of 2600 km in radius. Io has a geocentric phase angle of 90° (i.e., at eastern elongation) and an Io System III longitude of 50°. On the sky viewing plane, the horizontal axis (x) is the distance from Io along the projected Io-Jupiter line, and the vertical axis (z) is the projected distance from Io above and below the satellite orbital plane. Io is shown to scale by the filled circle located at (0,0).

Figure 6. 1990-1993 Observations of [O I] 6300 Å Emissions Near Io. The [O I] 6300 Å emission brightnesses for the 48 observations are shown as a function of the Io System III longitude angle. The brighter emissions occur for the data when Io is west (+ symbols) of Jupiter rather than east (x symbols) of Jupiter.

Figure 7. Angular Distribution of the [O I] 6300 Å Emission Data Near Io. The angular distributions in Io System III longitude of the 1990-1993 observations and the 1994 observations are shown separately and are divided into observations for Io east of Jupiter (x symbol) and for Io west of Jupiter (+ symbol).

Figure 8. Voigt Fit to the Solar Spectrum. The solar spectrum, the excellent fit to the solar spectrum using the new Voigt fitting program of F. Scherb, and the very small residue of the Voigt fit are all shown for wavelengths near 6300 Å. The line center of the emission line (6300.30 Å) for no Doppler shift is shown above the profile by the "0", with the arrows about this position indicating a Doppler shift range of ± 0.5 Å which is a typical (but not the maximum) range for the motion of the Io emission feature because of Doppler motions.

Figure 9. Observation of the [O I] 6300 Å Emission from Io. The small Io and terrestrial [O I] 6300 Å emission features measured on May 5, 1991 using the solar-stellar spectrograph on the McMath-Pierce telescope at Kitt Peak are indicated above the large Io reflected solar spectrum along with the excellent Voigt fit to the total spectrum and the very small residue of the Voigt fit.

Figure 10. Observed Variability of the 6300 Å Emission Near Io. The observed emission brightness is shown as a function of Io System III longitude when Io is west of Jupiter. The brightness as seen in the 5.2 arcsec x 5.5 arcsec aperture centered on Io is referenced to the disk area of Io.

Figure 11. Observed Variability of the 6300 Å Emission Near Io. The observed emission brightness is shown as a function of Io System III longitude when Io is east of Jupiter. The brightness as seen in the 5.2 arcsec x 5.5 arcsec aperture centered on Io is referenced to the disk area of Io.

Figure 12. Calculated Variability of the 6300 Å Emission at Io's Position in the Plasma Torus. The 6300 Å emission brightness, in relative units, is shown as a function of the satellite geocentric phase angle and the Io System III longitude angle. The plasma torus description adopted in the calculation is inherently symmetric in System III longitude and is for an offset and tilted dipole magnetic field in the presence of a nominal ($\epsilon = 0.025$) east-west electric field.

Figure 13. Calculated Lifetime for SO₂ at Io's Position in the Plasma Torus. The electron impact dissociation lifetime, in units of hours, is shown as a function of the satellite geocentric phase angle and the Io System III longitude angle. The plasma torus description is the same as adopted in Figure 12.

Figure 14. Spatial and Spectral Information for Sodium Near Io. Three data products derived from one of the sodium emission observations (namely, FR87I 340 in Table 7) acquired in 1987 by N. M. Schneider along an east-west oriented slit centered on Io are shown for both the D₁ and D₂ emission lines.

Figure 15. Variation of the Sodium D₂ Brightness Profile Near Io for the 1987 Emission Data Set. The spatial profiles of the brightness for 48 observations are positioned about the circle in accordance with their measured Io geocentric phase angles. Io's location is where the dotted circle cuts each profile and the intensity (kR) is plotted vertically.

Figure 16. Variation of the Sodium D₂ Velocity Centroid for the Line Profile for the 1987 Emission Data Set. The spatial profiles of the velocity centroid for 48 observations are positioned about the circle in accordance with their measured Io geocentric phase angles. The centroid velocity of the line profile is zero (i.e. relative to Io's projected motion) where the dotted circle cuts each spatial profile and the velocity (km s⁻¹) of the centroid is plotted vertically.

Figure 17. A Molecular-Ion Jet Source for High Speed Sodium. A gray-scale image generated by the molecular-ion jet source model for high speed sodium is shown. The model corresponds to image number w32339 taken by Schneider et al. (1991b). Models of other images in the sequence reproduce the changing morphology of the jet. For this case Io, indicated by the small dot on the right, was at a geocentric orbital phase angle of 209 degrees and had an Io System III longitude angle of 297 degrees. The black circle at the center represents Jupiter.

SO₂ LIFETIME IN THE IO PLASMA TORUS

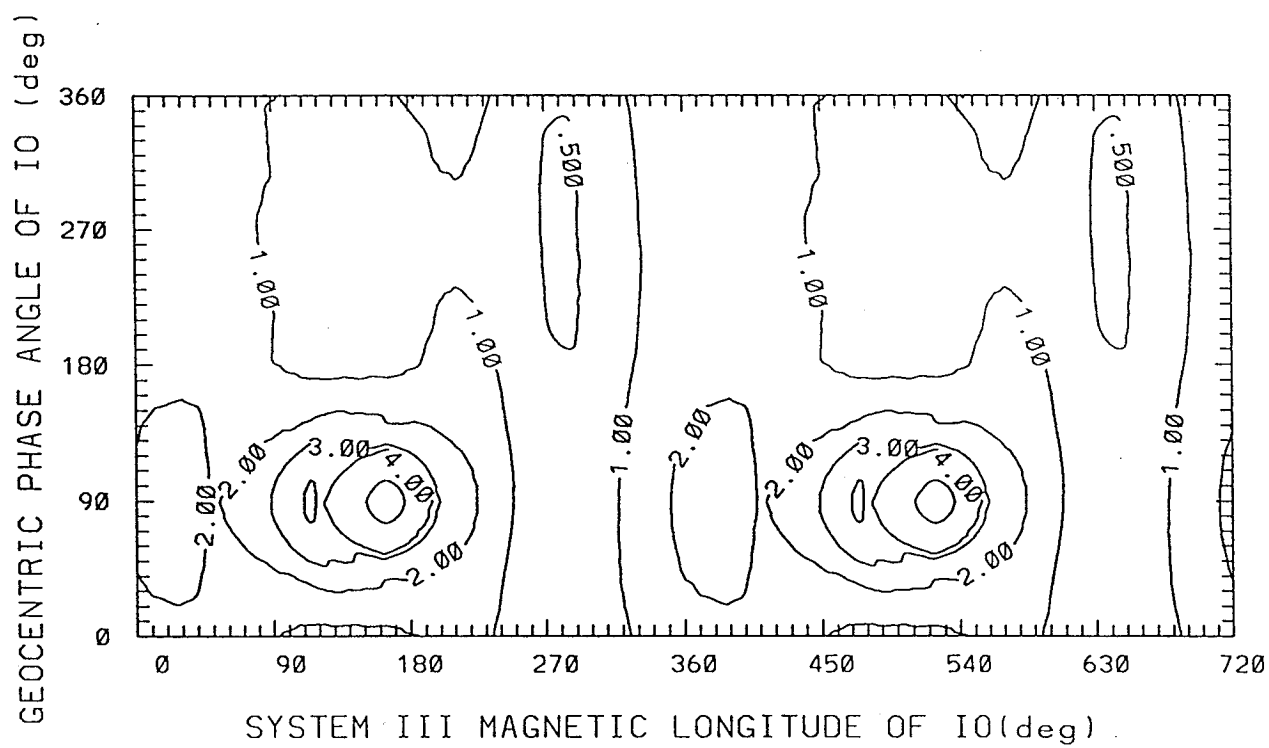


Figure 1

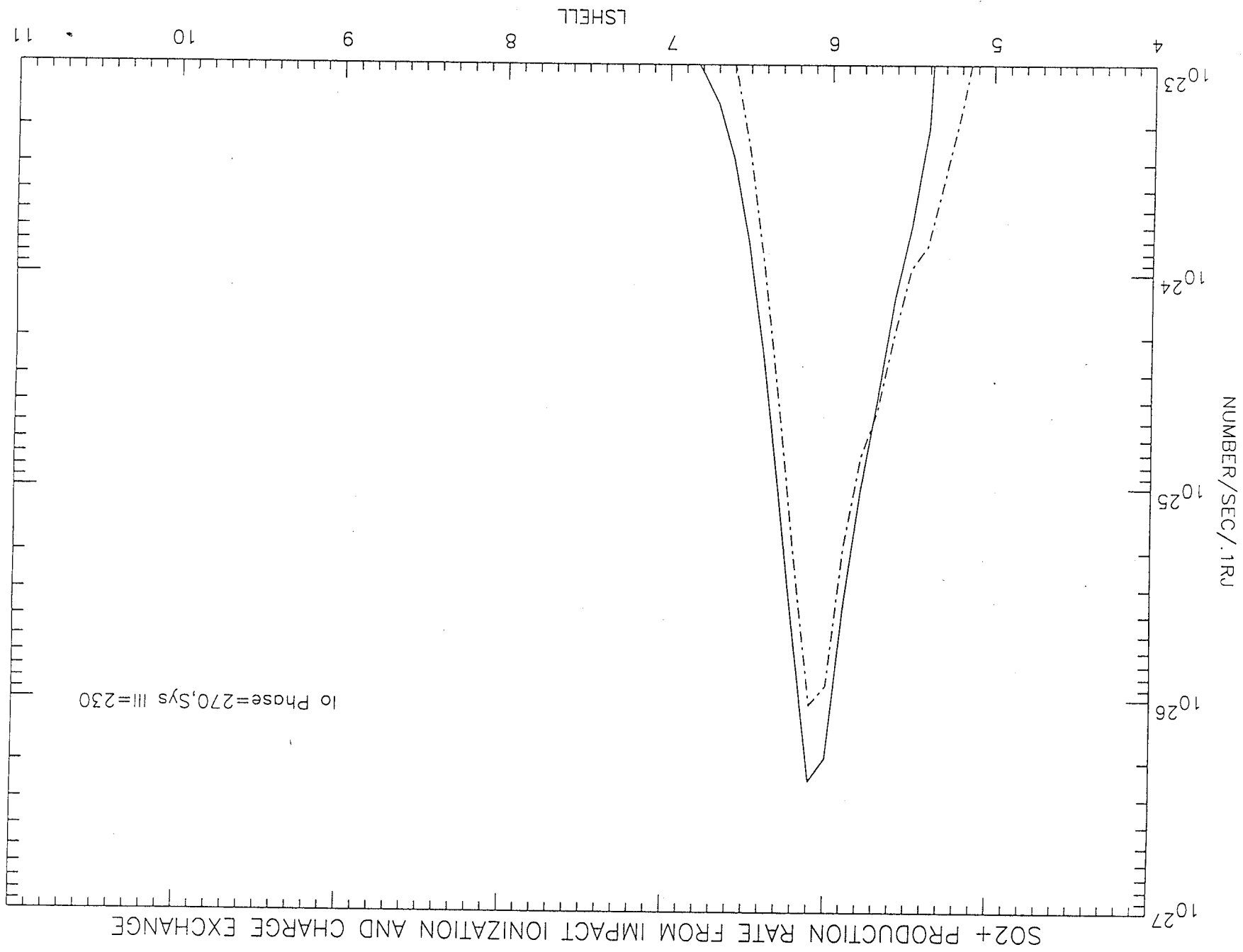


Figure 2

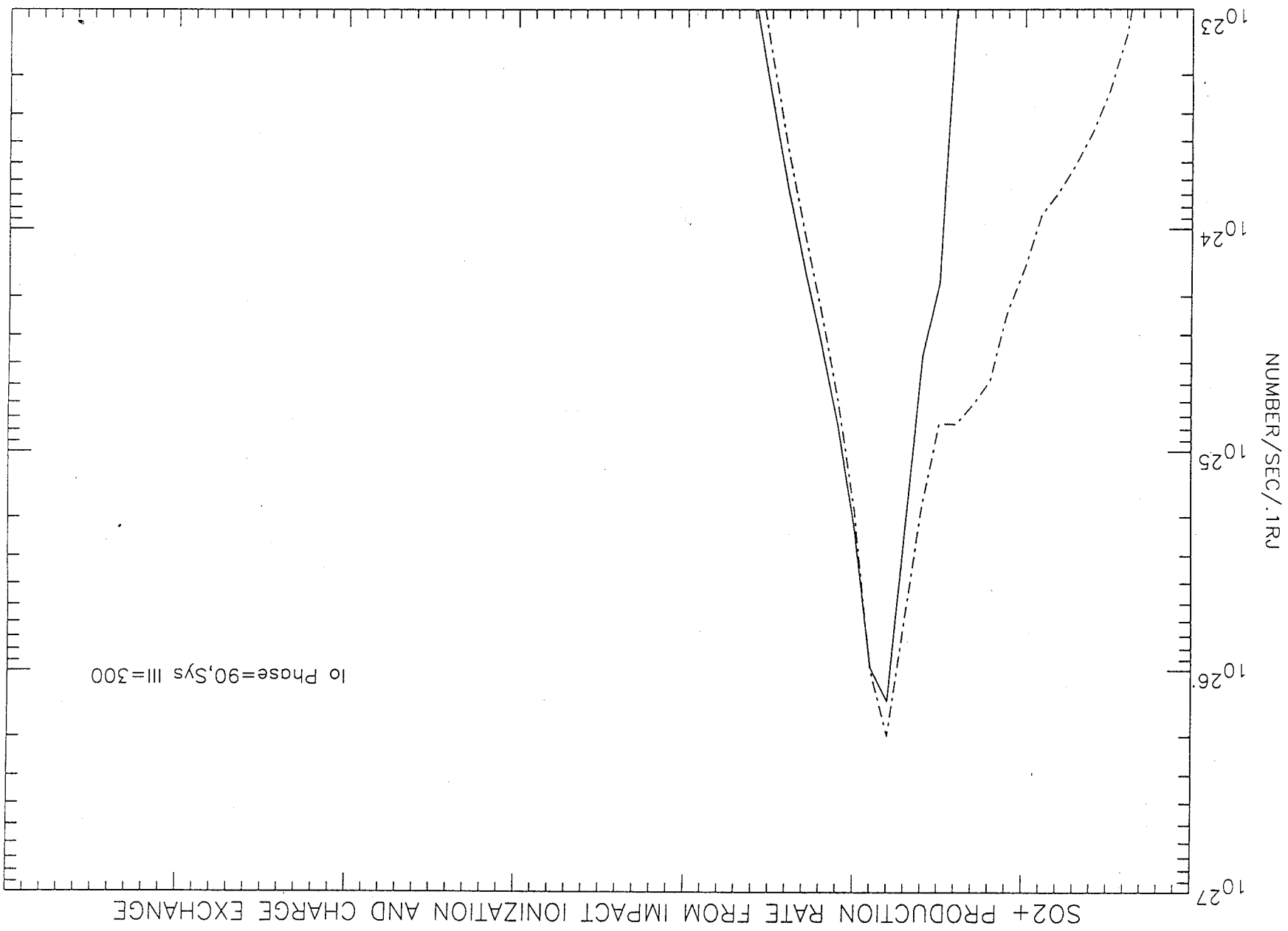


Figure 3

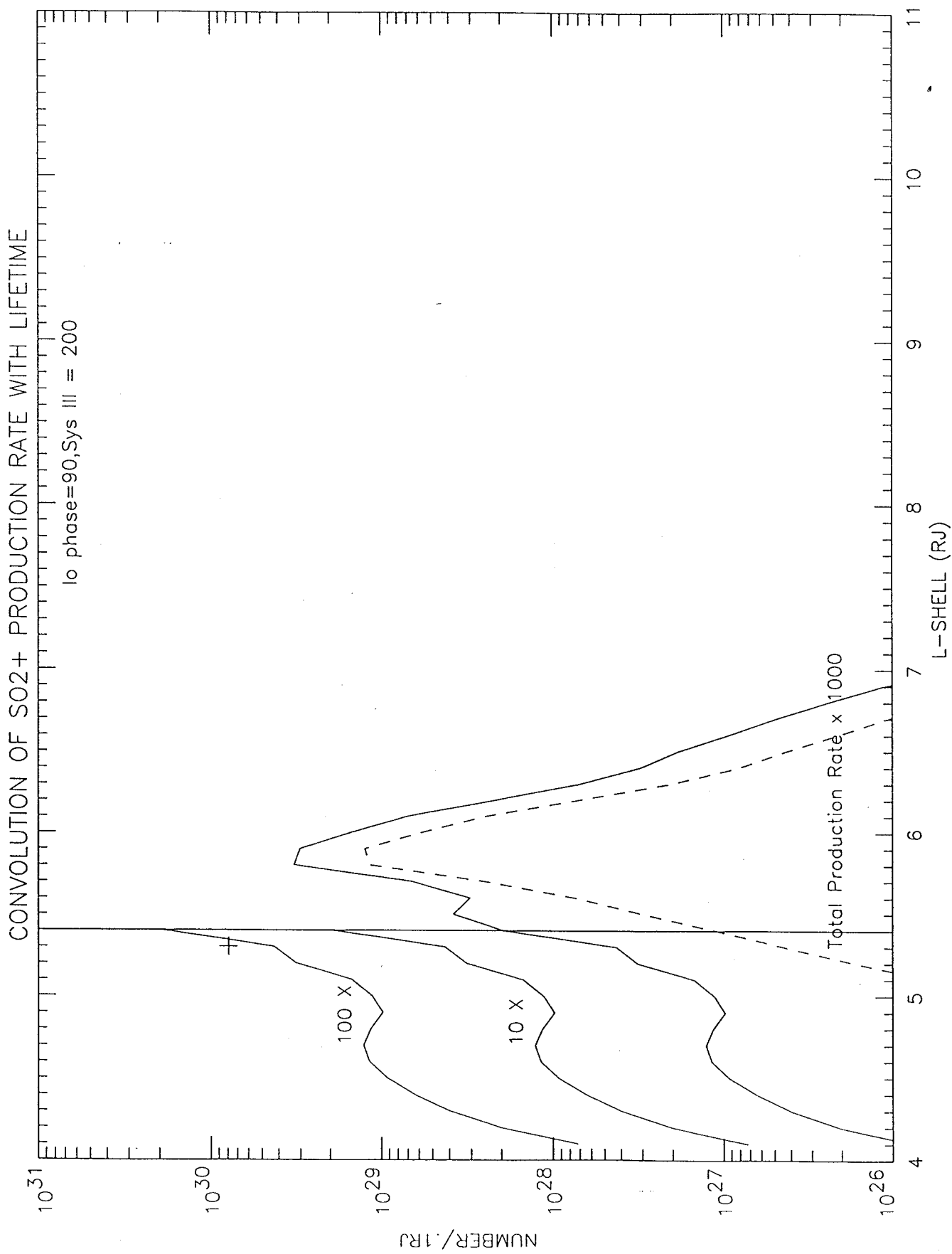


Figure 4

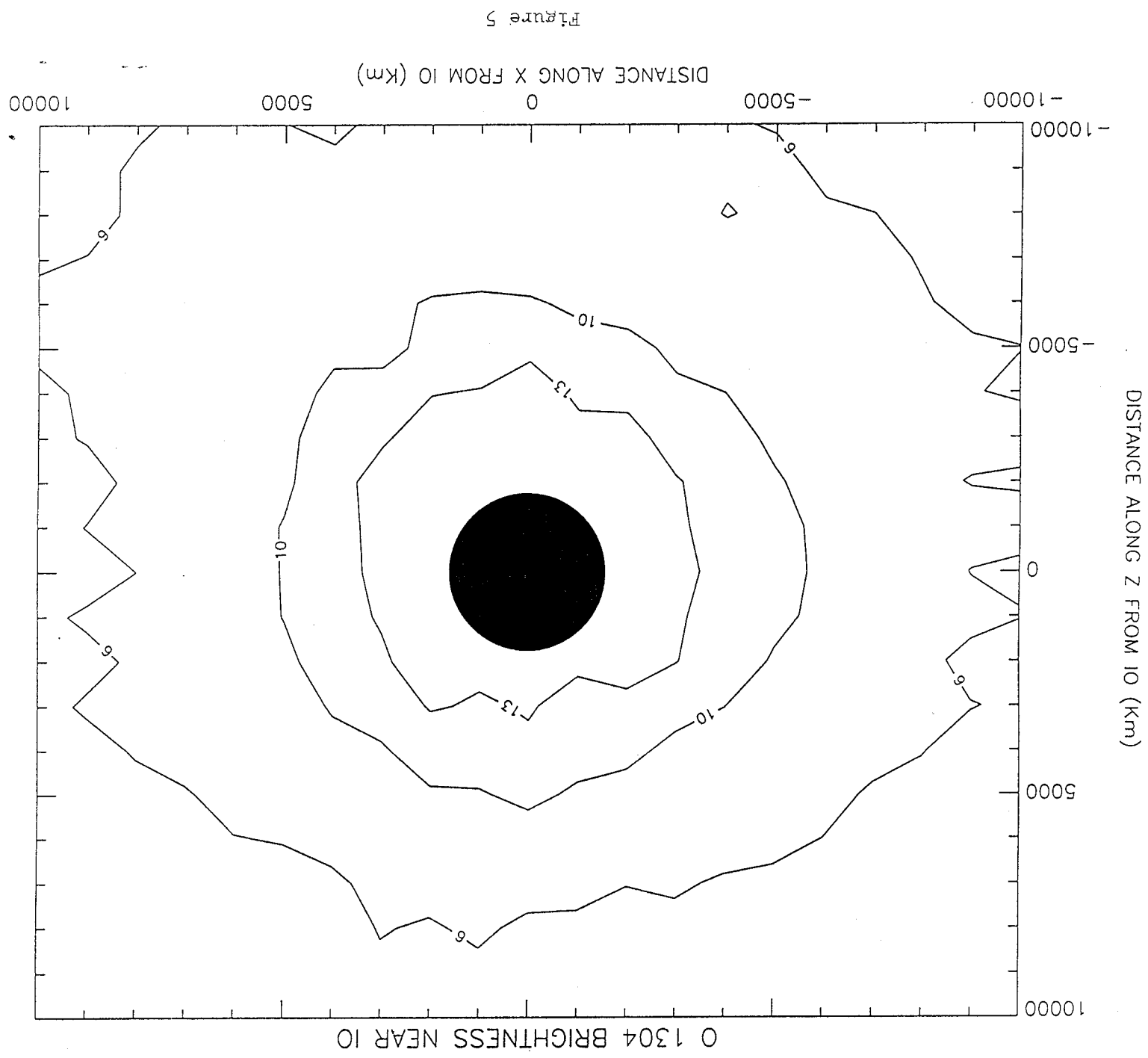


Figure 5

1990-1993 OBSERVATIONS OF [O I] 6300 Å EMISSION NEAR IO

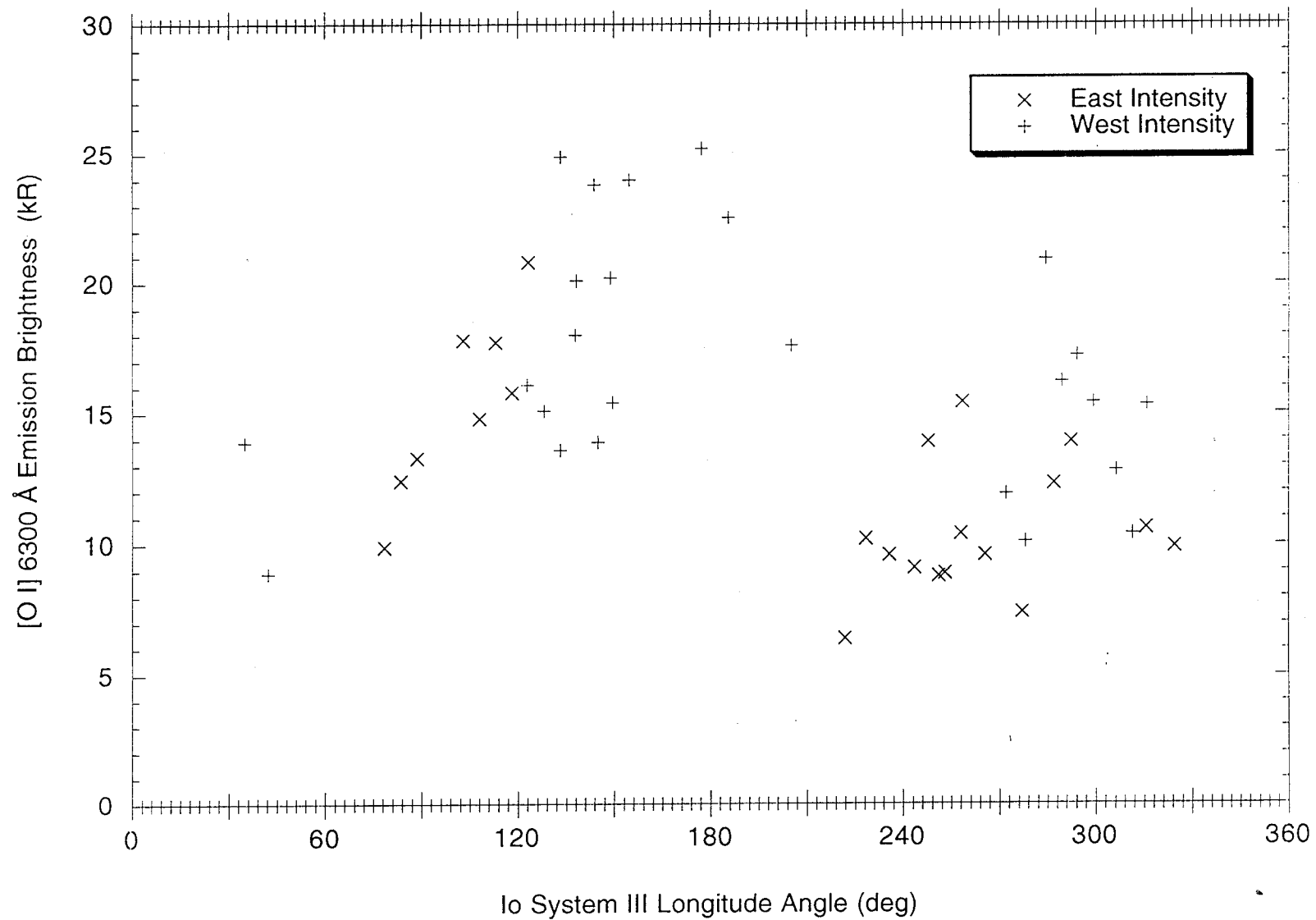


Figure 6

ANGULAR DISTRIBUTION OF THE [O I] 6300 Å EMISSION DATA NEAR IO

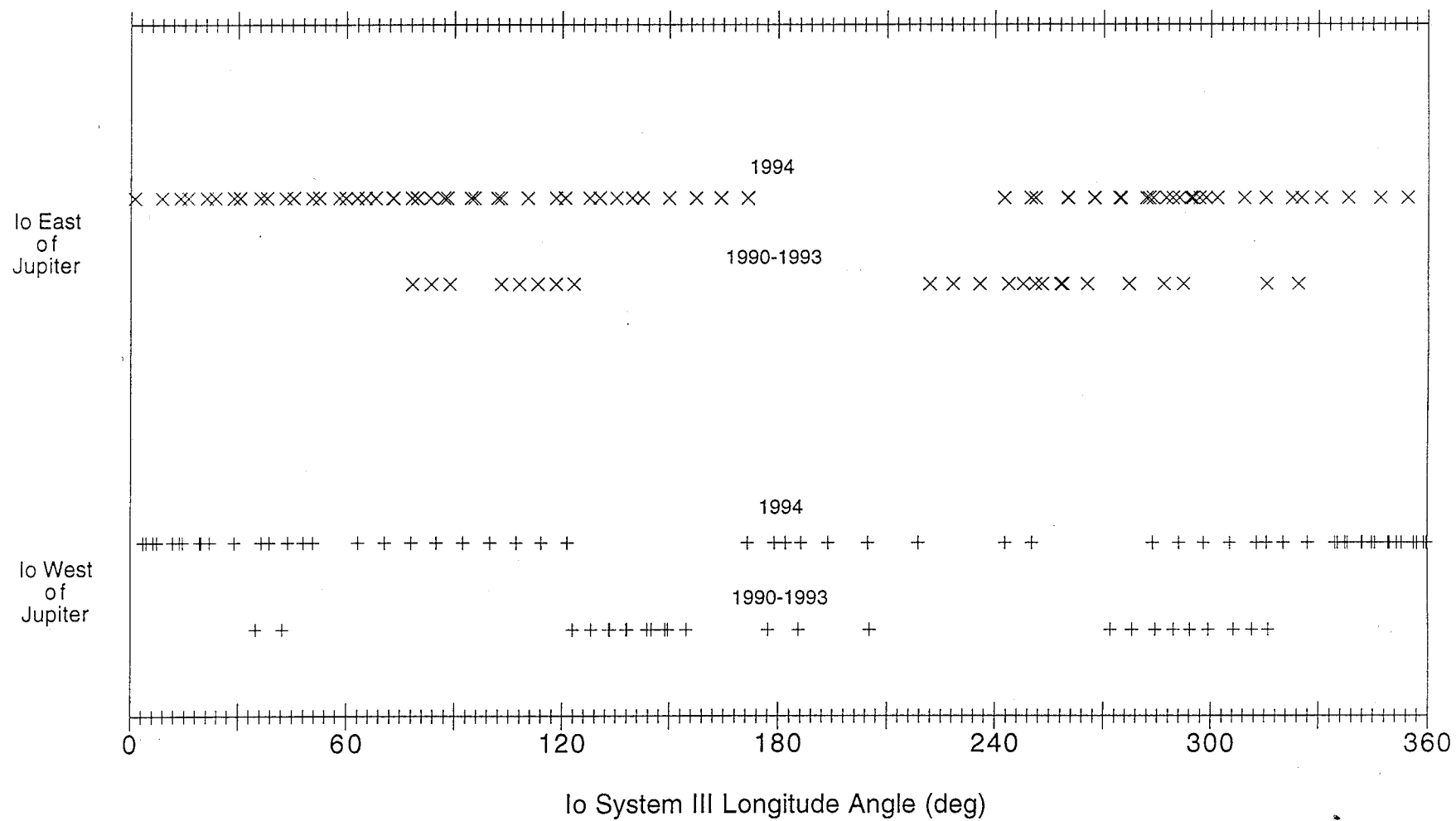


Figure 7

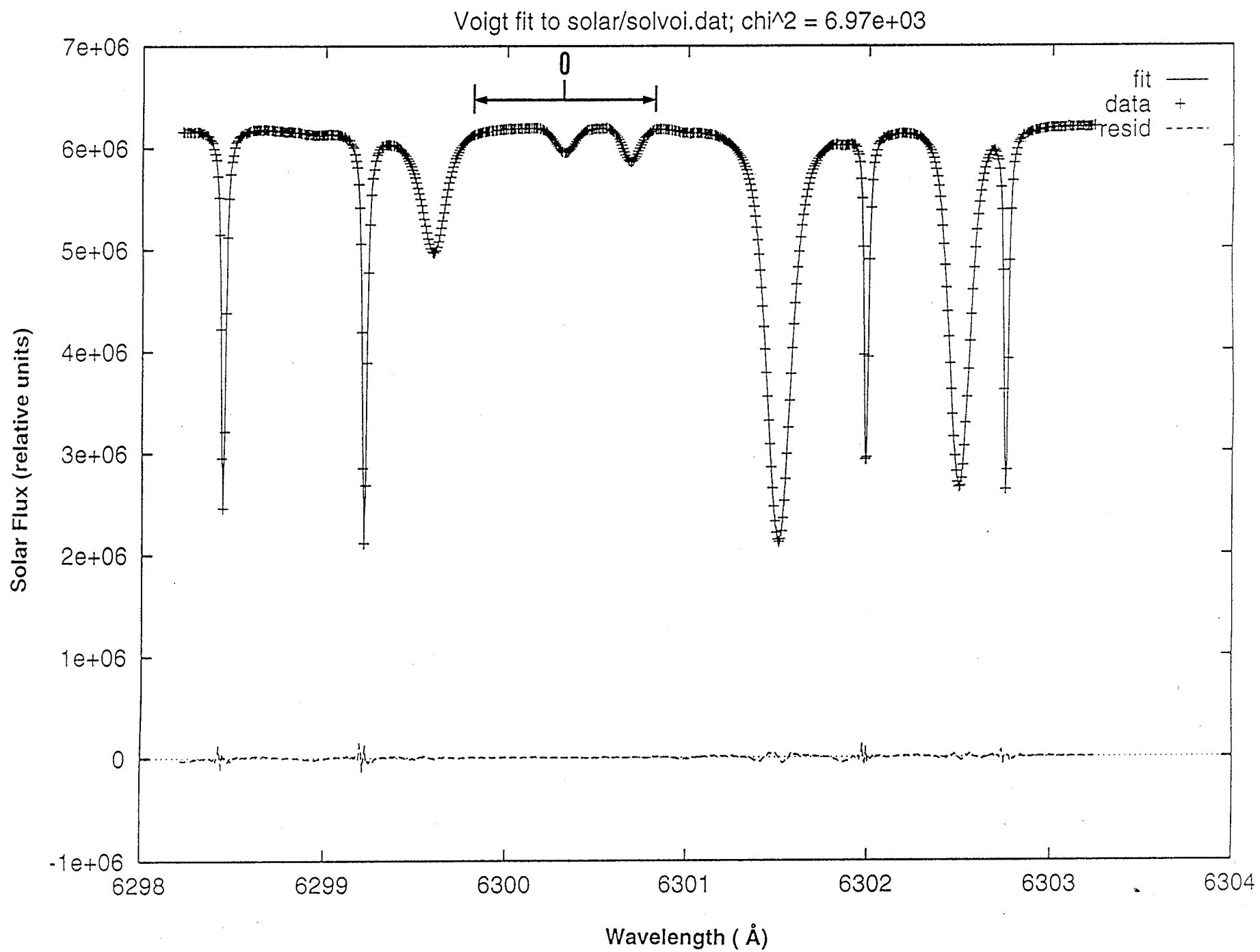
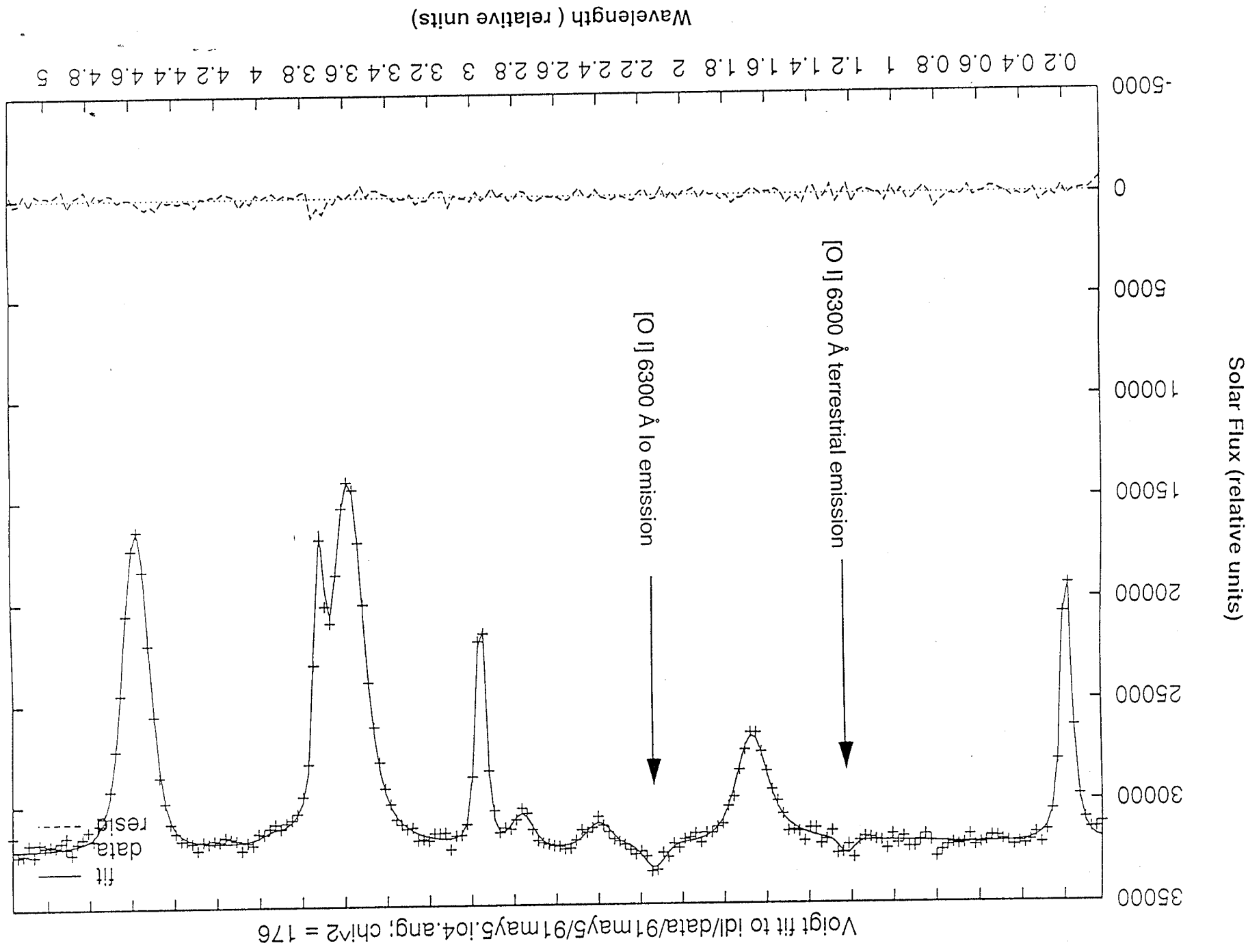


Figure 8



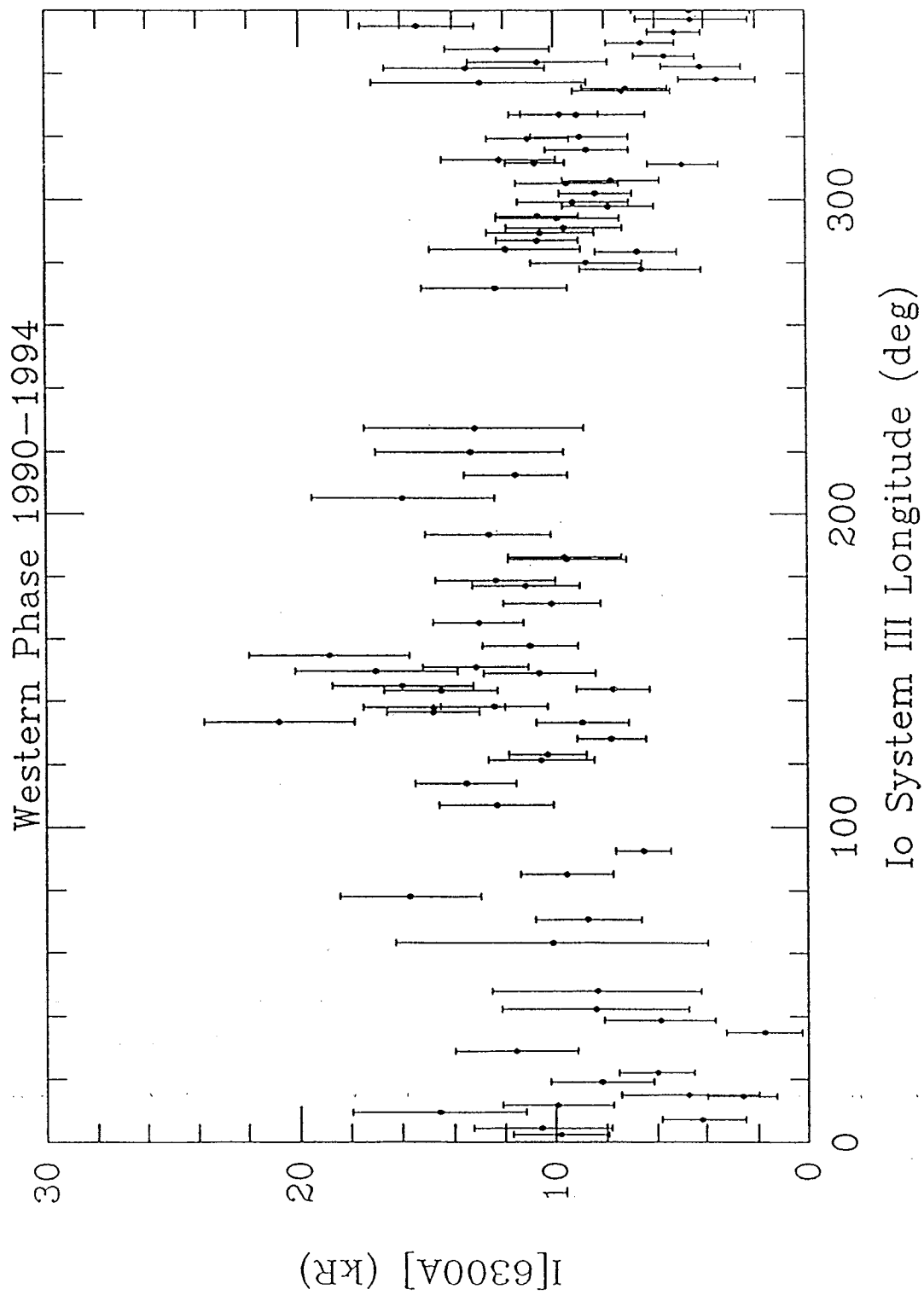


Figure 10

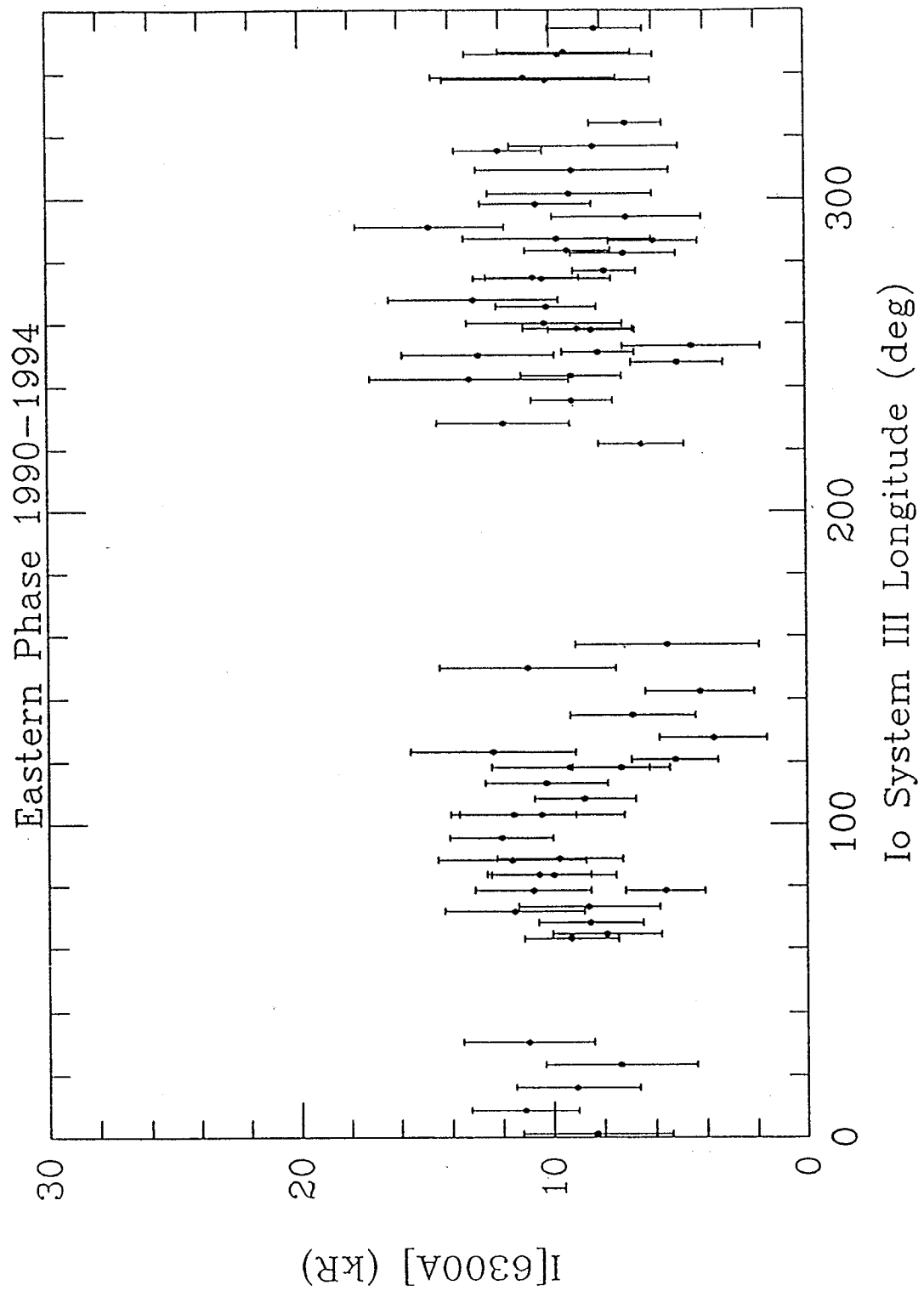


Figure 11

O(1D) 6300 EMISSION AT IO ($\times 10^{**6}$) (no asym, $\epsilon = .025$)

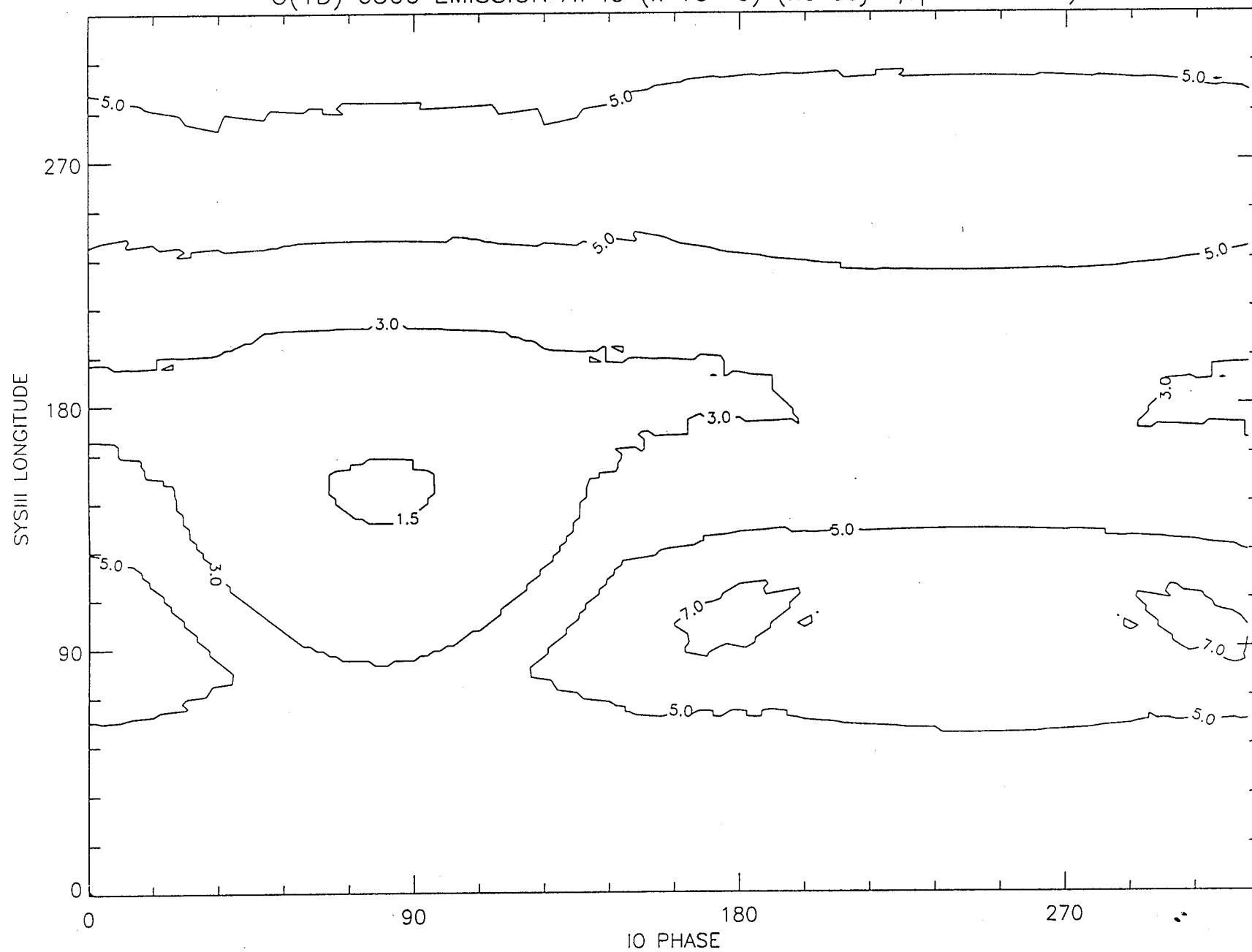


Figure 12

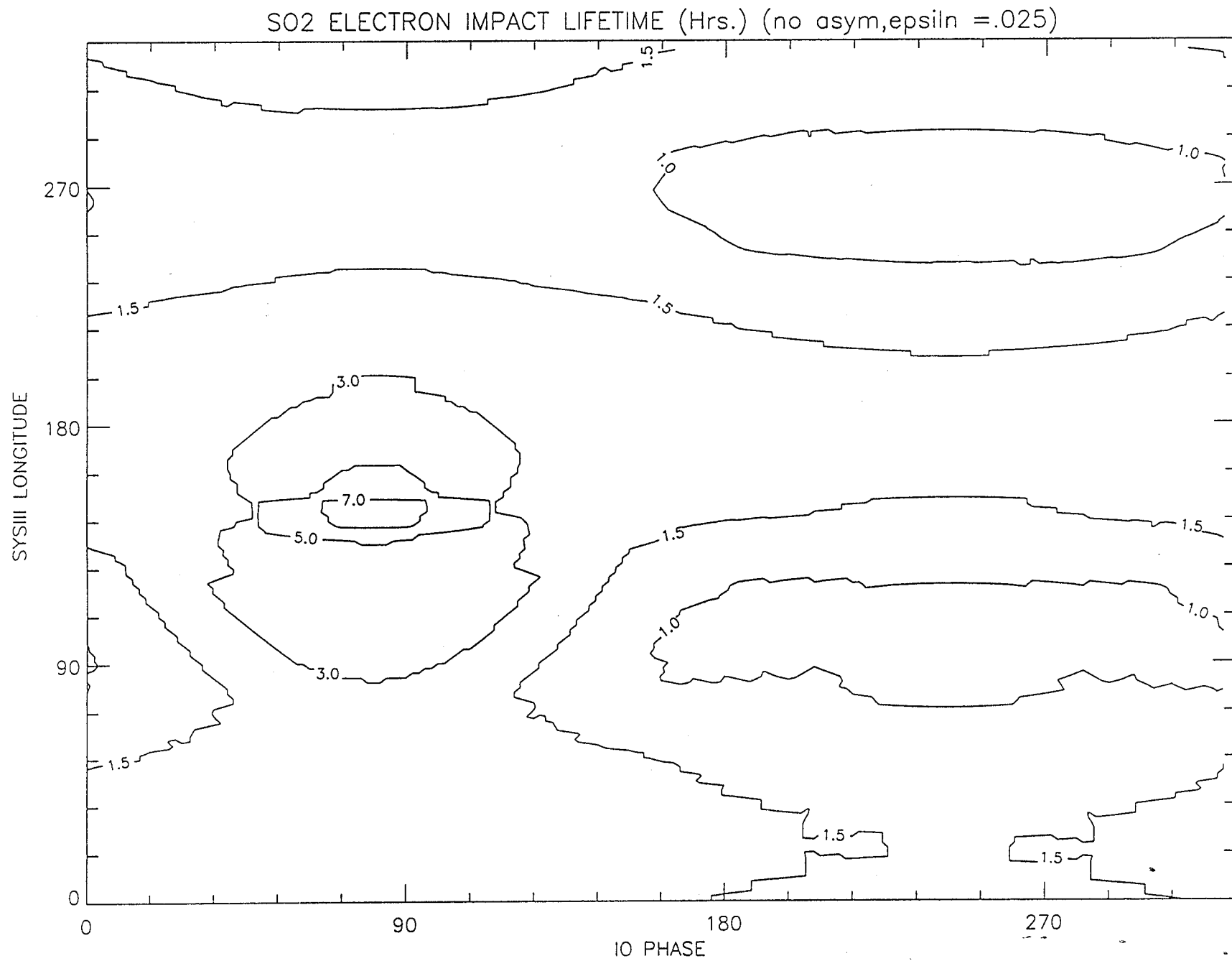


Figure 13

fr87i340 10 88.2325

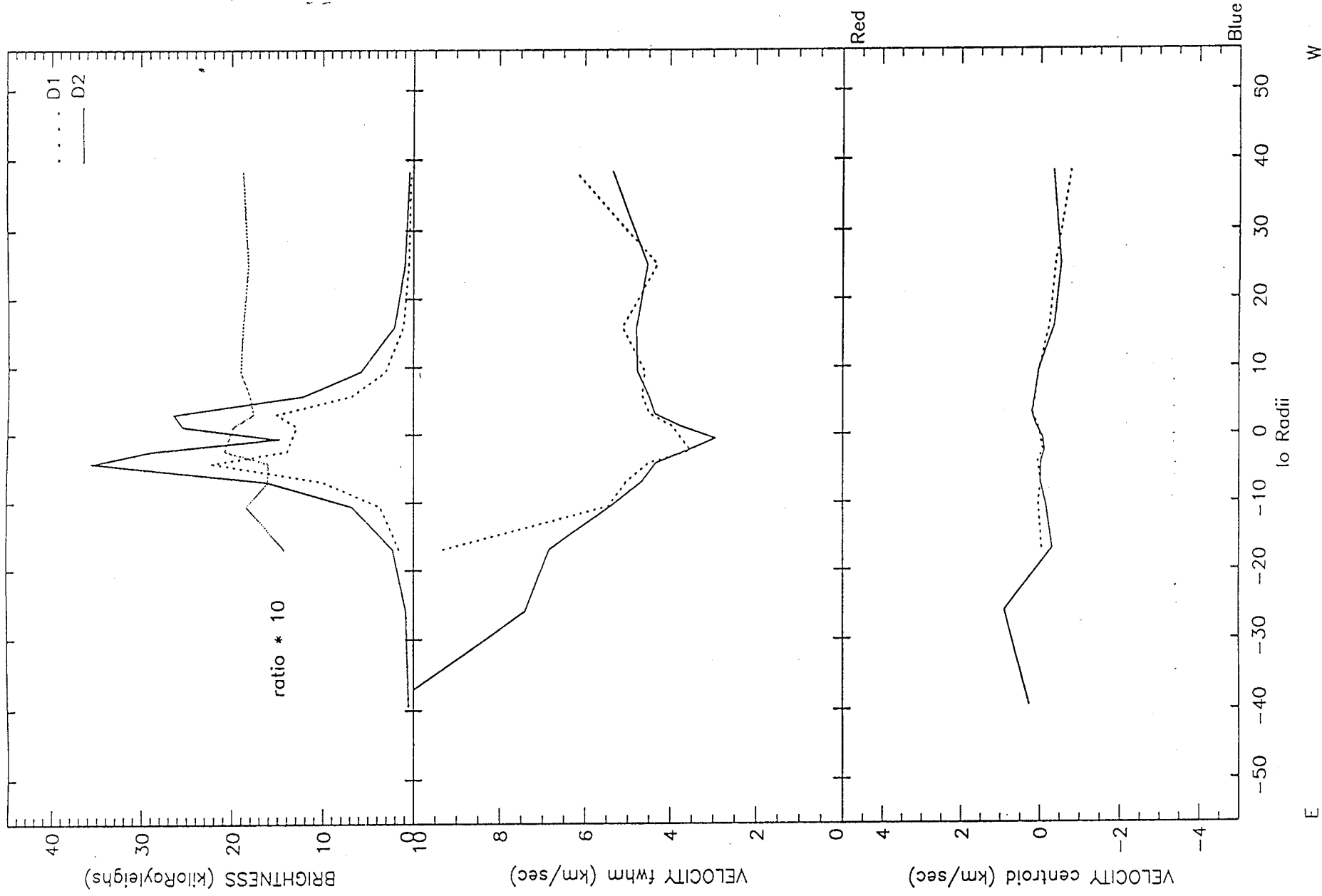


Figure 14

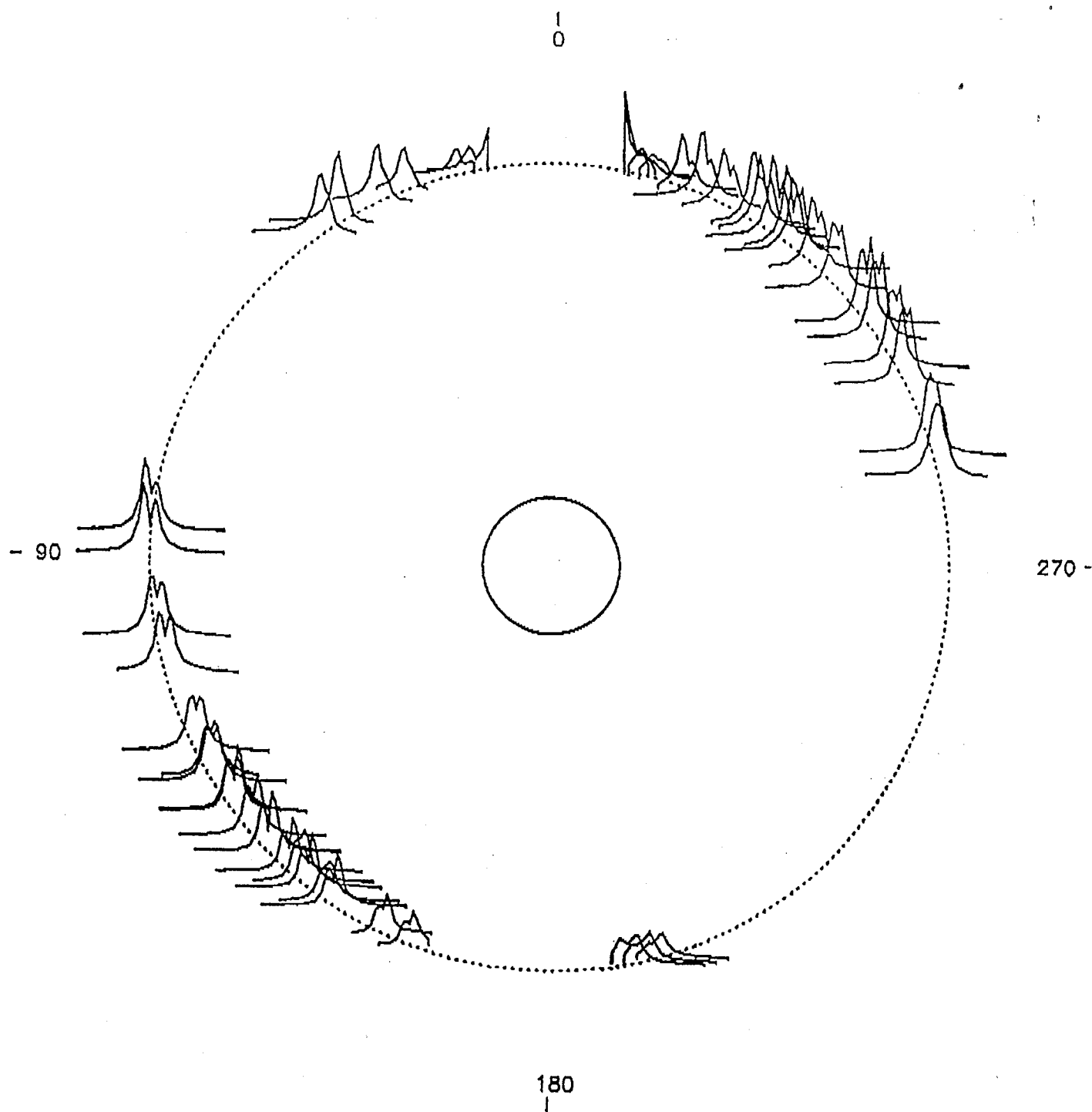


Figure 15

1
0

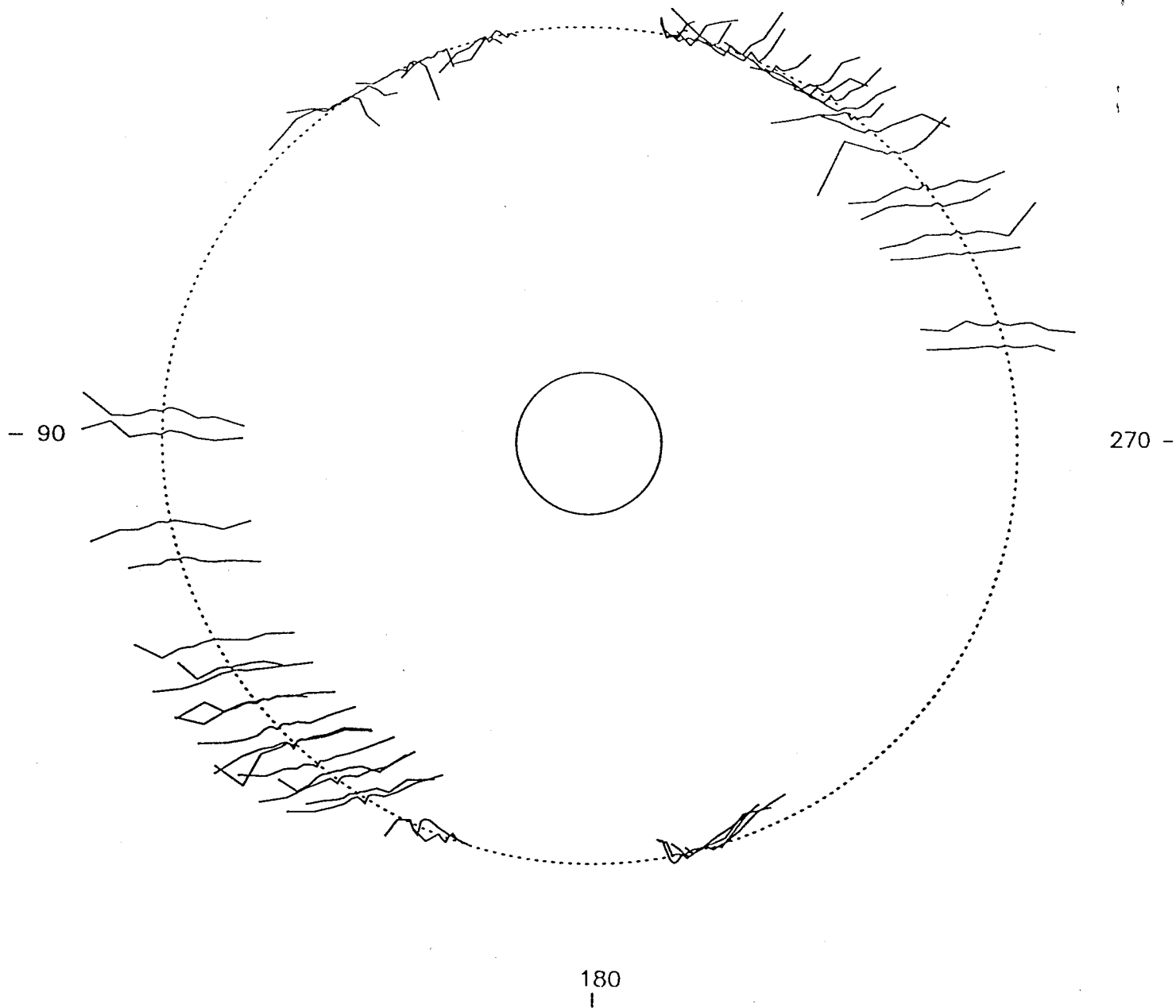


Figure 16

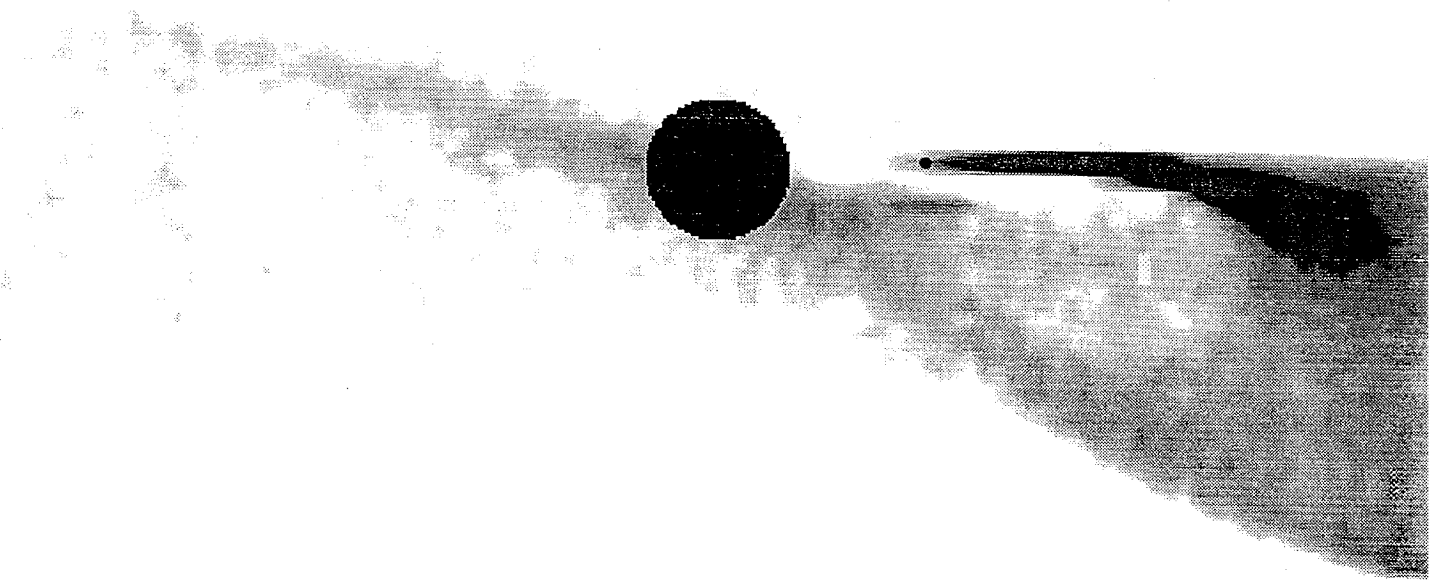


Figure 17

APPENDIX

Io's Sodium Corona and Spatial Extended Cloud :

A Consistent Flux Speed Distribution

Io's Sodium Corona and Spatially Extended Cloud :

A Consistent Flux Speed Distribution

William H. Smyth¹

Michael R. Combi²

Revised May 3, 1996

1. Atmospheric and Environmental Research, Inc., Cambridge, MA 02139

2. Space Physics Research Laboratory, University of Michigan, Ann Arbor, Michigan 48109

Number of manuscript pages : 46

Number of Figures : 11

Number of Tables : 5

Key words : Io, satellite exospheres, gas tori

Running heading : Io's Sodium Corona and Spatially Extended Cloud

For editorial correspondence and proofs please contact:

William H. Smyth

Atmospheric and Environmental Research, Inc.

840 Memorial Drive

Cambridge, MA 02139

Telephone number : (617) 547-6207

Fax number : (617) 661-6479

Internet : smyth@aer.com

ABSTRACT

A data set, composed of different groundbased observations for Io's sodium corona and spatially extended sodium cloud and covering the spatial range from Io's nominal exobase of 1.4 satellite radii to east-west distances from Io of ± 100 satellite radii (R_{Io}), is used to investigate the velocity distribution of sodium at the exobase. The data set is composed of the novel 1985 eclipse measurements of Schneider *et al.* (1991) acquired from ~ 1.4 to $\sim 10 R_{Io}$ from Io, the 1985 east-west emission data of Schneider *et al.* (1991) acquired from ~ 4 to $\sim 40 R_{Io}$ from Io, and sodium cloud image data acquired from ~ 10 to $\sim 100 R_{Io}$ from Io by a number of different observers in the 1976 to 1983 time frame. A one-dimensional east-west profile that contains Io is constructed from the data set and is analyzed using the sodium cloud model of Smyth and Combi (1988a,b). When the directional feature in the trailing cloud is either north or south of this east-west line (i.e., not at the null condition), an isotropic modified [incomplete ($\alpha=7/3$) collisional cascade] sputtering flux speed distribution at the satellite exobase with a peak at 0.5 km sec^{-1} provides an excellent fit to the data set for a sodium source of $1.7 \times 10^{26} \text{ atoms sec}^{-1}$. In particular, the model calculation reproduces (1) the essentially symmetric column density distributions exhibited by the eclipse measurements about Io within the Lagrange sphere radius ($5.85 R_{Io}$, i.e., the gravitational grasp of the satellite), (2) the change in the slope of the column density observed just beyond the Lagrange sphere radius in the east-west profile of the forward cloud, but not in the trailing cloud, and (3) the distinctly different east-west brightness profiles exhibited by the forward and trailing clouds in the emission data at the more distant ($\sim \pm 20$ - $100 R_{Io}$) portions of the cloud. In contrast, the speed dispersion at the exobase for either an isotropic Maxwell-Boltzmann flux speed distribution or an isotropic classical ($\alpha=3$) sputtering flux speed distribution (which has a higher velocity-tail population than the Maxwell-Boltzmann, but not as high as the incomplete collisional cascade sputtering distribution) is shown to be inadequate to fit the data set. To fit the enhanced trailing east-west profile observed when the directional feature is at the null condition, an additional

enhanced high-speed ($\sim 15\text{-}20\text{ km sec}^{-1}$) sodium population is required which is nonisotropically ejected from the satellite exobase so as to preferentially populate the trailing cloud. The need for such a nonisotropic high-speed population of sodium is essentially consistent with the earlier modeling analysis of the directional features (Pilcher *et al.* 1984), the more recent medium-velocity component required in modeling the sodium zenocorona (Smyth and Combi 1991; Flynn *et al.* 1992), and the very recent modeling of the directional feature reported by Wilson and Schneider (1995). A complete sodium source rate speed distribution function at Io's exobase from $0\text{-}100\text{ km sec}^{-1}$ is then constructed by combining the isotropic modified [incomplete ($\alpha=7/3$) collisional cascade] sputtering flux speed distribution, the nonisotropic directional feature (lower-velocity zenocorona) source ($\sim 15\text{-}20\text{ km sec}^{-1}$), and the higher-speed ($\sim 20\text{-}100\text{ km sec}^{-1}$) charge-exchange source required to simulate the sodium zenocorona far from Jupiter.

1. INTRODUCTION

Atomic sodium in the Jupiter system originating from a satellite source at Io has been observed from groundbased facilities in the D₁ (5889.95 Å) and D₂ (5895.92 Å) emission lines during the past twenty-five years. Using an observing slit, the sodium emission which is excited by solar resonance scattering was first discovered in 1972 by Brown (1974) very near Io where its intensity is brightest [\sim many 10's of kiloRaleighs (kR)] and where the sodium density is dominated by low-speed (~ 2 km sec⁻¹ or less) ballistic atom orbits in the satellite "corona". By occulting the bright region near Io, image observations (Murcray 1978; Murcray and Goody 1978; Matson *et al.* 1978) were first acquired in 1976 and 1977 for fainter (\sim few to 0.5 kR) sodium more distant from Io but still near its circular orbit (radius of 5.9 Jupiter radii) about the planet and revealed the presence of a predominant "forward cloud" and a less spatially extensive "trailing cloud" that moved with the satellite. This sodium has been characterized primarily by a source of low-speed (~ 2.6 -4 km sec⁻¹) atoms that have sufficient energy to just escape from Io with an excess velocity of only ~ 1 km sec⁻¹ (or so) and thereby remain gravitationally bound to Jupiter fairly near the satellite orbit. Additional observations (Pilcher *et al.* 1984; Goldberg *et al.* 1984) of even fainter (~ 1 to 0.2 kR) sodium in the early 1980's discovered a "directional feature" attached to Io in the trailing cloud that oscillated north and south about the satellite plane with a phase and period determined by the Io System III longitude angle. This sodium source was characterized by atoms with speeds ~ 20 km sec⁻¹ ejected nonisotropically from the satellite so as to populate the trailing cloud and the circumplanetary space at larger radial distances beyond Io's orbit. From earlier slit measurements (Trafton and Macy 1978) in 1974, fainter (~ 30 Rayleighs) sodium emissions well beyond Io's orbit had been observed at a radial distance of ~ 60 planetary radii, while from more recent images (Mendillo *et al.* 1990), very faint (~ 1 Rayleigh) sodium emissions were observed at radial distances of ~ 400 -500 planetary radii. Sodium at these larger radial distances is called the "magneto-nebula" or "sodium zenocorona" and is thought to be populated primarily by an nonisotropic charge-exchange source of high speed (~ 15 -100 km sec⁻¹) atoms at Io

with velocity skewed in the forward direction of corotational plasma motion past the satellite, and secondarily by a narrow forward sodium jet produced by a spatially distributed molecular ion source (Wilson and Schneider 1994). Most of this sodium escapes the Jupiter system, forms a sodium pause in the sunward direction at ~ 2300 planetary radii because of solar radiation acceleration, and is eventually lost by photoionization to the solar wind (Smyth and Combi 1991).

The observations of sodium emissions on many different spatial scales in the Jupiter system thus indicate that its atomic source at Io's exobase must have a wide dispersion of speeds. Modeling of these observations has in the past been mostly undertaken separately for only one of these spatial regions at a time. Although the higher velocity dispersions for the sodium zenocorona may be reasonably well understood because of its large spatial structure and the lack of any significant sodium lifetime impact of the magnetosphere, a consistent source for the slower sodium in Io's corona and in the forward and trailing clouds near its orbit has not been established. The recent determination of the sodium spatial profile in the Io corona obtained from the groundbased eclipse data of Schneider (1988; Schneider *et al.* 1987, 1991) coupled with earlier emission observations, however, now provides a viable observational base from which it is possible to pursue the nature of this slower sodium. The investigation of a consistent exobase sodium source for Io's corona and the forward and trailing clouds near its orbit is therefore undertaken in this paper. A consistent flux speed distribution at the exobase is determined, and the corresponding sky-plane spatial distribution of sodium near Io is presented. Sodium source information obtained from previous modeling analysis of Io's corona and the forward and trailing clouds is first summarized in section 2. The observational data base to be investigated in this paper is presented in section 3. Modeling of an east-west spatial profile determined from this observational data base is undertaken in section 4. Discussion and conclusions are presented in section 5.

2. EARLIER SODIUM MODELING

The major modeling analysis studies for the spatial distribution of sodium near Io and its orbit are summarized in Table 1. The summary is divided into three observed spatial regions: (1)

the Io corona located within the satellite Lagrange sphere (average radius of $5.81 R_{Io}$ or ~ 3 arcsec), (2) the neutral cloud located beyond the Lagrange sphere and near Io's orbit, and (3) the north-south oscillating directional features, observed to trail Io in its orbit. Modeling analysis studies for the Io corona are, furthermore, subdivided into early observations of the average intensity in a $8 \text{ arcsec} \times 3 \text{ arcsec}$ slit centered on Io reported by Bergstralh *et al.* (1975, 1977) that indicated an east-west intensity asymmetry of ~ 1.25 and later observations for a one-dimensional column density profiles within the Lagrange sphere reported by Schneider *et al.* (1987, 1991).

2.1 Corona: East-West Intensity Asymmetry

In Table 1, the early studies of Smyth (1983) for sodium atoms ejected monoenergetically from Io's exobase established that small scale structures in the D-line intensity profile observed as a function of the Io geocentric phase angle (Bergstralh *et al.* 1975, 1977) could arise from modulation of the atoms' escape rate from Io caused by the action of solar radiation acceleration in the D-lines. These modulations occur primarily for exobase speeds near 2.0 km sec^{-1} and 2.1 km sec^{-1} , which are near the escape-speed threshold of the Lagrange sphere. Later studies of Smyth and Combi (1987a) showed that the main reason for the east-west intensity asymmetry was, however, an east-west electric field which altered the plasma properties at Io's orbit so as to increase the sodium lifetime and hence sodium abundance when Io was preferentially east of Jupiter. More complex modeling studies of Smyth and Combi (1988b) constrained the flux velocity dispersion for sodium at Io's exobase by simultaneously fitting the average east-west intensity asymmetry and also the general spatial morphology of the forward sodium cloud, located on a much larger spatial scale well beyond the Lagrange sphere. These studies showed that the sodium ejection speed at the exobase required to fit the east-west intensity asymmetry is double-valued, having a lower value $\leq 1 \text{ km sec}^{-1}$ and a higher value in the range $2.6\text{--}3.65 \text{ km sec}^{-1}$. For a Maxwell-Boltzmann flux distribution, the lower and higher most probable speed values were 0.71 km sec^{-1} ($T=460 \text{ K}$) and 3.65 km sec^{-1} ($T=12,300 \text{ K}$). Neither distribution was, however, suitable for properly populating the forward cloud. The lower value produces essentially only

ballistic atoms orbits which could not populate the forward cloud, while the higher value was significantly larger than the nominal $\sim 2.6 \text{ km sec}^{-1}$ characteristic monoenergetic velocity required to reproduce the proper spatial morphology of the forward cloud as a function of the Io geocentric phase angle. For a Maxwell-Boltzmann flux distribution with a nominal thermal exobase temperatures in the range $\sim 1000\text{-}2000 \text{ K}$, the calculated east-west intensity ratio was much higher than the observed value with the atoms still contributing primarily to the corona density and again far too deficient in energy to contribute any significant sodium to the forward cloud. For the preferred ($\alpha=7/3$) modified-sputtering distribution of Smyth and Combi (1988b) with a source strength of $\sim 2 \times 10^{26} \text{ atoms/s}$, the lower and higher speed values were $\leq 0.5 \text{ km sec}^{-1}$ and $\sim 2.9 \text{ km sec}^{-1}$, respectively, with the latter value being preferred because of its closer proximity to the $\sim 2.6 \text{ km sec}^{-1}$ characteristic velocity for the forward cloud. Interestingly, however, it is actually the lower value that will be shown in this paper to reproduce the correct spatial profile for sodium both within the Lagrange sphere and beyond in the more distant neutral cloud.

2.2 Corona: Column Density Profile

In Table 1, modeling studies of Smyth and Combi (1987b,c) determined that typical forward cloud brightness data for the sodium cloud could be properly simulated well beyond the Lagrange sphere radius of $\sim 5.81 R_{\text{Io}}$ by an sodium source of $\sim 1 \times 10^{26} \text{ atoms/s}$ ejected monoenergetically from Io's exobase with a characteristic velocity of $\sim 2.6 \text{ km sec}^{-1}$. They also established that this same sodium source reproduced the column density profile of Schneider *et al.* (1987) within the Lagrange sphere down to a radius of $\sim 3.5 R_{\text{Io}}$. For a radius smaller than $\sim 3.5 R_{\text{Io}}$, the calculated profile was lower than the observed profile, indicating that lower (ballistic and escape) velocity components are required, in addition, as part of a more realistic flux velocity dispersion. A similar behavior for the simulated column density profile, with an even more dramatic departure from the observed profile both inside and outside the Lagrange sphere, was also later shown by a model calculation of Ip (1990) who assumed an exobase speed of 3 km sec^{-1} but did not include the gravity of Jupiter so as to properly include the near zero escape speed

conditions for sodium at the Lagrange sphere. Adopting for the sodium atoms at the exobase a simple (i.e., binding-energy velocity $v_b = 0$) classical sputtering energy distribution with a low energy cut-off and also excluding Jupiter's gravity, McGrath (1988) modeled the column density within the Lagrange sphere and produced a profile with a slope slightly less steep than the observation for an infinite sodium lifetime and a slope somewhat steeper than the observation for a sodium lifetime of 3 hr. Alternatively adopting a Maxwell-Boltzmann flux distribution, assuming an infinite sodium lifetime, and similarly also excluding Jupiter's gravity, Summers *et al.* (1989) and Schneider *et al.* (1991) modeled the column density within the Lagrange sphere region and produced a profile that reasonably well matched the observed profile for an exobase temperature, respectively, of 1000 K based on the partial eclipse data set (Schneider *et al.* 1987) and of 1500 K based on the complete eclipse data set (Schneider *et al.* 1991). Although these different flux velocity distributions reasonably fit the observations within the Lagrange sphere, it is clear from the earlier studies of Smyth and Combi (1988b) that the Maxwell-Boltzmann distributions are energetically deficient and inappropriate for populating the neutral cloud and that the more energetically promising sputtering distribution cannot be investigated adequately near or beyond the Lagrange sphere radius without properly including the gravity of Jupiter, solar radiation acceleration, and the spacetime variable lifetime of sodium in the plasma torus. The study will be undertaken in section 4.

2.3. Sodium Cloud

The early studies in Table 1 for the sodium cloud were general in nature, probing its poorly documented spatial and angular extent about the planet. Based upon the solar resonance scattering excitation mechanism for sodium (Bergstrahl *et al.* 1975) and limited angular extent data determined by slit-averaged intensity data, Carlson *et al.* (1975) undertook monoenergetic (3.5 km sec⁻¹) model calculations and estimated that the sodium cloud lifetime (assumed to be spatially uniform) was likely determined by electron impact ionization by the (then very poorly characterized) plasma in planetary magnetosphere. This general picture for the cloud was

confirmed by more extensive model calculations performed by Fang *et al.* (1976) and Smyth and McElroy (1977), the latter of which explored the time evolution and two-dimensional nature of the cloud for exobase velocities near the Io Lagrange escape speed. The acquisition of sodium cloud images in late 1976 and early 1977 brought this subject into dramatic focus. For a classical sputtering flux distribution that peaked at 4 km sec^{-1} , Matson *et al.* (1978) successfully modeled a one-dimensional east-west brightness profile (derived from a cloud image), which extended from Io in the forward cloud to $\sim 80 R_{\text{Io}}$ and in the trailing cloud to $\sim 40 R_{\text{Io}}$ but which excluded sodium emission within Io's corona. The analysis (Smyth and McElroy 1978) of the much larger sodium cloud image data set (Murcray 1978) also indicated that the forward cloud could be characterized by an exobase ejection speed of $\sim 2.6 \text{ km sec}^{-1}$ and that its changing intensity pattern could be understood as the changing viewing perspective of an approximately steady state cloud on the sky plane as Io moved on its orbit around Jupiter. The observed predominance of the forward sodium cloud over the trailing cloud was accomplished in all these models by limiting the exobase source area to a hemisphere (see Table 1) and by limiting the assumed spatially uniform lifetime so as to dynamically select sodium atom orbits that would primarily populate the forward cloud. Additional modeling studies by Macy and Trafton (1980) of the radial and vertical cloud structure on a larger spatial scales indicated source dispersion speeds at least up to 13 km sec^{-1} were, however, required to explain a variety of other observations. Additional model studies (Smyth 1979, 1983) showed that the troublesome east-west orbital asymmetry of the sodium cloud (Goldberg *et al.* 1978) was not source related but due to the perturbing action of solar radiation acceleration on the sodium atom orbits. Adopting a one-dimensional radially dependent sodium lifetime in the plasma torus based upon limited Voyager spacecraft data and an asymmetric exobase source for a classical sputtering distribution with a peak velocity at 4 km sec^{-1} , Goldberg *et al.* (1980) successfully modeled another one-dimensional east-west brightness profile acquired during the Voyager 1 encounter for distances extending from Io in the forward cloud to $\sim 80 R_{\text{Io}}$ and in the trailing cloud to $\sim 30 R_{\text{Io}}$. Later modeling by Smyth and Combi (1988) using a more accurate two-dimensional

spacetime-dependent sodium lifetime in the plasma torus and an isotropic (or near isotropic) exobase sodium source of $\sim 2 \times 10^{26}$ atoms sec^{-1} demonstrated that the predominant forward cloud was caused by the highly radially-dependent sink for sodium in the plasma torus and not by a nonisotropic source. The deduced characteristic or peak exobase speed for the more definitive modeling of the forward sodium cloud above is, therefore, in the range ~ 2.6 to 4 km sec^{-1} and is much larger than required to characterize the sodium column density profile in Io's corona. A different flux speed distribution is therefore needed for consistency and is addressed in section 4.

2.4 Directional Feature

In Table 1, observations acquired in 1980 and 1981 by Pilcher *et al.* (1984) for weaker D-line emissions in the trailing portion of the sodium cloud allowed them to discover an elongated feature in the brightness distribution that on the sky plane was directed away from Jupiter and was inclined sometimes to the north and sometimes to the south of the satellite's orbital plane. The north/south direction of the feature was shown to be correlated with Io's magnetic longitude and suggested a formation mechanism involving the oscillating plasma torus. Modeling analysis by Pilcher *et al.* indicated that the feature resulted from a high-velocity ($\sim 20 \text{ km sec}^{-1}$) sodium source that was at near right angles to Io's orbital motion with a source strength required on the outer satellite hemisphere of $\sim 1 \times 10^{26}$ atoms sec^{-1} . This peculiar directionality of the source was investigated by Sieveka and Johnson (1984) who concluded that it was produced by direct collisional ejection of neutral sodium from the exosphere by the corotating plasma flow past Io, as exhibited in their discussion of interaction potentials for these collisional processes. More recent modeling by Smyth and Combi (1991) of the sodium zenocorona showed that it required a two component exobase source: a similar high-velocity ($\sim 20 \text{ km sec}^{-1}$) sodium source of $\sim 1 \times 10^{26}$ atoms sec^{-1} for the spatial distribution nearer the planet and an even higher-velocity ($\sim 57 \text{ km sec}^{-1}$) sodium source of $\sim 2 \times 10^{26}$ atoms sec^{-1} for the spatial distribution further from the planet. Both source components, however, were based on ion-neutral charge exchange processes in Io's exosphere and were therefore composed of a speed tangential to Io's orbit at Io's position plus an

isotropic Maxwell-Boltzmann distribution with a most probable speed of about one-third of the tangential speed in the Jupiter frame (i.e., one-third of ~ 37 and ~ 74 km sec $^{-1}$, respectively). The lower component is therefore symbolically denoted in the Io frame by 20 ± 12 km sec $^{-1}$ in Table 1. Very recently, successful modeling of the directional features has also been reported by Wilson and Schneider (1995) who have used a similar lower component source denoted in Table 1 by 20 ± 10 km sec $^{-1}$, where the isotropic portion of their source may be variable in magnitude.

3. OBSERVATIONAL DATA BASE FOR MODELING

To describe the entire sodium spatial distribution in Io's corona and beyond in the extended neutral clouds, three different sodium observations obtained on very different spatial scales are to be combined. For the sodium spatial distribution within Io's corona and beyond in the near extended cloud, we have selected the ground-based observations obtained at the Catalina Observatory 1.5 meter telescope using the LPL echelle spectrograph by Schneider (1988; Schneider *et al.* 1987, 1991) in 1985 when the Galilean satellites of Jupiter underwent mutual eclipse. As reported in Schneider *et al.* (1991), two different types of observations were acquired, eclipse observations and emission observations, and were interleaved over six nights in the late summer and early fall. The dates, times, orbital angular parameters of Io, spectral ID numbers, and the numbering of these observations as adopted in this paper are summarized in Table 2. The eclipse observations provided for the first time accurate information about the density gradient of atomic sodium in the corona within the Lagrange sphere of Io (i.e., a radius of $5.81 R_{Io}$) for the radial interval from ~ 1.4 to $6 R_{Io}$. The emission observations acquired along an east-west aligned slit centered on Io yielded the most accurate spatial information from the Lagrange sphere outward into the nearer portion (i.e., ~ 6 – $40 R_{Io}$ from Io's center) of the sodium cloud. To describe sodium in the neutral cloud at larger distances from Io, we have selected a number of sodium cloud image observations acquired between 1976 and 1983 for Io in the vicinity of its orbital elongation points. As illustrated in Figure 1, these sodium cloud images were used to extract east-west D $_2$ brightness

profiles that overlap the spatial range of the emission data and extend it to $\pm 100 R_{Io}$. The closer spatial regions of the eclipse data and the near Io emission data are, however, masked in the cloud images by a circular (or nearly circular) occulting mask of $\sim 10 R_{Io}$ in radius centered on Io. A description of the eclipse, emission, and image cloud observations relevant to establishing the composite observational base for our modeling analysis is given below.

3.1 Eclipse Observations

Eclipse observations measured the absorption feature at the D-line wavelengths as seen from Earth in the spectra of the reflected sunlight from the disk of another Galilean satellite (either Europa or Ganymede for measurements of interest here) that was produced by sodium in Io's atmosphere as Io eclipsed the sun from the viewpoint of the other Galilean satellite. Since the equivalent width of each absorption profile can be directly converted to a column abundance of sodium along the optical path, successive measurements during one solar eclipse of either Europa or Ganymede by Io were used to produce a spatial profile of the column density near Io. Of particular interest in this paper are the five higher quality eclipse profiles of Schneider *et al.* (1991) listed in Table 2. Four of the five eclipse profiles were acquired when Io was east of Jupiter (i.e., an Io geocentric phase angle within 90 ± 90 degrees), and only one was acquired when Io was west of Jupiter (i.e., within 270 ± 90 degrees).

The column density profiles for all five of the eclipse observations are presented collectively in Figure 2 and follow directly from the information given by Schneider *et al.* (1991) in their Table 3. Only one lower-bound data point from eclipse 4 at a distance from the center of Io of $1.17 R_{Io}$ is excluded since it is well within the nominal exobase radius of $1.4 R_{Io}$. The spatial profile for eclipse 2 obtained on September 14 when Io was very near eastern elongation is highlighted by the filled circles in Figure 2 and seen to be similar to the other four spatial profiles. For the five profiles, the error bars for the eclipse 2 data points are the smallest, being no larger than the size of the filled circles within the Lagrange radius and no more than about a factor of two larger outside this distance. A comparison of the two sides of each eclipse measurement shows no

detectable difference in the slopes of their separate profiles within the Lagrange sphere radius of Io, thus effectively reduces all the eclipse data to one radially symmetric profile. This symmetric profile deduced by Schneider *et al.* is shown by the dashed line in Figure 2 and has the power law fit $N(1.4 \leq r \leq 5.85) = 2.55 \times 10^{12} r^{-2.48}$ for the data points within the Lagrange radius, where N is the column density in units of atoms cm^{-2} and r is the distance from the Io's center in units of the R_{Io} . This power law fit undercuts the data points outside the Lagrange radius where the eclipse observations are less reliable. Although the eclipse data beyond the Lagrange sphere contain more vertical scatter, they appear to suggest that the sodium profile may have a reduced slope near this boundary, as will be verified by the emission observations. This slope change will be seen to be caused by the dominant planetary gravitational field beyond the Lagrange radius of Io.

3.2 Emission Observations

Emission observations measured the solar resonance scattered D-line intensity emitted by sodium atoms in the near cloud environment of Io. In addition to spectral information, which is only briefly considered in this paper, these observations provide a one-dimensional spatial profile for the D-line emission brightnesses along a slit that is oriented east-west (i.e., perpendicular to the spin axis of Jupiter) and that is centered on Io and contains (or very nearly contains) its disk. Of interest in this paper are nine higher quality emission observations listed in Table 2, for which seven were obtained when Io was east of Jupiter and only two when Io was west of Jupiter.

The D_2 brightness profiles for the nine emission observations, where each observation has both an east and west profile relative to Io's location, are all shown in Figure 3. This information, previously published only in a graphical format (Schneider *et al.* 1991), is summarized numerically in Table 3 as provided by Schneider (1990, 1995 private communication). The nonuniform spatial coverage in Table 3 occurs because of different distance intervals adopted to obtain good average brightness values (given different signal to noise ratios) and because of signal drop-out associated with constraints imposed on positioning the slit profile on the CCD detector during interleaved eclipse and emission measurements. In Figure 3, the spatial profile for emission

4, obtained on September 14 when Io was nearest eastern elongation, is highlighted, with its east profile (filled diamond) and west profile (open diamond) shown separately. Excluding all data points inside of $4 R_{Io}$ where the seeing and instrumental effects artificially flatten the profile, the power law fit is $I_{D_2}(r \geq 4) = 101 r^{-1.45}$ for the remaining emission brightness data in Figure 3, where I_{D_2} is the D_2 brightness in kiloRayleighs (kR) and r is the distance from the center of Io in R_{Io} units. The D_2 brightness of ~ 100 kR as r approaches Io's surface is consistent (see Brown and Yung 1976) with the maximum sodium column density of $\sim 1 \times 10^{12}$ atoms cm^{-2} deduced from the eclipse data in Figure 2. Again excluding emission data inside of $4 R_{Io}$, brightnesses for the different profiles in Figure 3 vary by a factor of ~ 3 to almost 5 at the same distance from Io but have error bars given in Table 3 that are as small as $\pm 10\%$ for the larger brightness values and no larger than $\pm 30\%$ for the smallest brightness values. The brightness error bars for the September 14 data points in Figure 3, for example, are vertically smaller than the diamond symbols at $4 R_{Io}$, comparable to the diamond symbols at $10 R_{Io}$, and about a factor of two taller than the diamond symbols at $35 R_{Io}$. This suggests that the large variation in the emission brightness in Figure 3 is real and likely correlated with the Io geocentric phase angle, the Io System III longitude, and the east-west asymmetry of the plasma torus as has been observed to be the case for the spatially more extensive sodium cloud image data. These correlations will indeed be shown to be the case when the sodium cloud image observations are presented and are compared to the emission data.

3.3 Sodium Cloud Image Data

A large number of sodium cloud images in the D_1 and D_2 emission lines were acquired in the 1975-1984 time interval (Murcray 1978; Murcray and Goody 1978; Matson *et al.* 1978; Goldberg *et al.* 1980, 1984; Morgan 1984, private communication) with emission brightnesses measured about Io to distances of $100 R_{Io}$ and larger, as illustrated in Figure 1. In these images, Io was centered behind an occulting mask typically 10 to 12 arc sec across (i.e., covering a radial distance from the center of Io of about $10 R_{Io}$) in order to block the bright disk-reflected sunlight

from the satellite's surface. The sodium brightness distribution in the immediate vicinity of the mask was usually spatially distorted in the resulting image but was consistently measured to be a few kiloRayleighs (kR), similar to the brightnesses of the emission data at $10 R_{Io}$ in Figure 3. Beyond the immediate vicinity of the mask, the structure of the sodium cloud emission brightness on the sky plane has been historically divided into a forward cloud, so-called because it appears ahead of the satellite in its orbit [i.e., in Figure 1 located right (west) of Io in image A and left (east) of Io in images B and C], and a corresponding trailing cloud that appears behind the satellite.

The change of the spatial brightness morphology of the forward sodium cloud with Io geocentric phase angle is well known (Murcray 1978; Murcray and Goody 1978; Smyth and McElroy 1978; Goldberg *et al.* 1984). As illustrated in Figure 1, the forward cloud changes its east-west orientation relative to the satellite's location as Io moves about Jupiter. This change in orientation is due primarily to the projection upon the two-dimensional sky plane of a three-dimensional cloud that is tilted inside of the tangent line to Io's orbit at the satellite's location by about 35 degrees (Smyth and McElroy 1978). When Io is east of Jupiter (i.e., left of Jupiter) and has a phase angle less than about 65 degrees, the forward sodium cloud is therefore observed to the east of Io. When Io is east of Jupiter and has phase angle between about 65 and 85 to 90 degrees (i.e., at its east symmetric turning point), the forward sodium cloud is swinging through and approximately aligned along the observer's line of sight, and the east and west profiles about Io are fairly symmetric. When Io is east of Jupiter and has a phase angle greater than about 85 to 90 degrees, the forward sodium cloud is observed to the west of Io as shown in Image A of Figure 1. Similarly when Io is west of Jupiter and has a phase angle less than about 235 degrees (its west symmetric turning point), the forward sodium cloud is observed to west of Io, and when the phase angle is greater than about 235 degrees, the forward sodium cloud is observed to east of Io, as shown in image B and C of Figure 1. The lack of mirror symmetry in the Io phase angles for the

east and west symmetric turning points is related to the perturbing action of solar radiation acceleration on the sodium atom trajectories (Smyth 1979,1983).

In the trailing cloud, the time-dependent change in the north-south inclination of the fainter directional feature is well known (Pilcher *et al.* 1984; Goldberg *et al.* 1984; Goldberg and Smyth 1996). The directional feature is north in image A (Io System III longitude of 247 degrees), south in image B (Io System III longitude of 104 degrees), and a slightly north but near the null east-west location in image C (Io System III longitude of 178 degrees). The north-south inclination of the directional feature was shown by Pilcher *et al.* (1984) to be correlated with the System III longitude of Io. The directional feature changes from a south to north inclination (a first null point) at an Io System III longitude near 165 degrees and change from north to south inclination (a second null point) for a second rather poorly defined Io System III longitude somewhere between about 320 and 25 degrees. When the directional feature is near the null location in Figure 1, an increase in both the spatial extension and brightening of the trailing cloud along the east-west oriented (dashed) line is readily apparent. In addition, since the trailing cloud is associated with a high-speed sodium source ($\sim 15\text{-}20 \text{ km sec}^{-1}$), an increase in the Doppler width of the spectral line for the trailing cloud brightness along an east-west slit through Io is also expected near the null location, as will be seen to be the case for the emission data of Schneider *et al.* (1991).

To develop a suitable observational data base for our modeling purposes with the same spatial format as for the 1985 east-west emission profiles of Schneider *et al.* (1991), we have extracted one-dimensional east-west D_2 brightness profiles through Io from selected sodium cloud images and have thereby extended the spatial range of the observed emission data coverage to $\pm 100 R_{Io}$ from the satellite. For the D_2 images of Murcray (1978), analysis by Smyth and McElroy (1978 see their Fig. 4) indicated that when Io was near eastern elongation the one kR brightness level in the forward cloud along an east-west line through the satellite occurred on the sky plane about $60 R_{Io}$ ahead of Io. Examination of a number of additional images indicates that the observed brightness of the forward cloud at this distance appears many times to be lower, although

generally it has been difficult to be precise because the cloud images are usually not measured to brightnesses less than about 0.2 to 0.5 kR. Using fourteen images of the sodium cloud for Io near its orbital elongation points that are summarized in Table 4, a range (or a bounding envelope) of values for the east-west D_2 brightness profile of the forward and trailing clouds has been determined and is shown in Figure 4 by the different shaded areas. The shaded areas are therefore appropriate bounds for the brightness profiles when Io is somewhat near the elongation point of its orbit. The forward and trailing cloud orientation depicted in Figure 4 is chosen for Io near eastern elongation in order to facilitate its later comparison with the 1985 emission data profiles, mostly acquired for Io east of Jupiter. For the trailing cloud profile in Figure 4, two different shaded areas have been extracted from the sodium cloud image information in Table 4 to quantify its D_2 east-west brightness profile. The two areas are for the two basic orientations of the directional feature: (1) lower area, when the directional feature is inclined either north or south and (2) upper area, when the directional feature is at the null or near null location. As expected, the shaded area for the directional feature near the null location is both brighter and less steep than the shaded area for the directional feature with either a significant north or south inclination. At larger distances from Io ($>30 R_{Io}$), note that both shaded D_2 brightness areas for the trailing sodium cloud are also dimmer and more closely confined to Io than the shaded brightness area for the forward cloud.

3.4 Comparison of the Emission Data and the Sodium Cloud Image Data

Information characterizing the forward and trailing D_2 brightness profiles for the nine 1985 emission profiles is summarized in the last seven columns of Table 2 and provides a simple basis for their inner-comparison and also their comparison with the known characteristics of the sodium cloud image observations. The first of these seven columns indicates whether the forward or trailing cloud profile is dominant (i.e., brighter at larger distances), the second column indicates the north, null, or south inclination of the directional feature as determined by the System III longitude angle of Io, and the third column indicates if there is an enhanced Doppler signature observed in the line profile of the forward or trailing D_2 brightness profile. The last four of these columns

provide the values of the exponent, β , and amplitude, A , for the power-law fit $[I_{D_2}(r \geq 4) = A r^{-\beta}]$ to the D_2 brightness profiles located east and west of Io. These fits omit data points inside $4 R_{Io}$ of Io's center where the emission data are artificially flattened. This information in Table 2 is discussed below and used to show that the east-west sodium brightness profiles from the emission data are quite consistent with the Io sodium cloud image data.

As expected from the sodium cloud image observations, the forward sodium cloud is generally more spatially extended and brighter than the trailing cloud. From the information for the emission profiles in Table 2, this is seen to be the case for emission 1 (Io phase angle 61.4°) acquired just before the east symmetric turning point and also for the three observations for emission 7 (Io phase angle 117.2°), emission 8 (Io phase angle 121.6°) and emission 9 (Io phase angle 143.1°), acquired well after the east symmetric turning point. For emission 2 (Io phase angle 72.2°), acquired during the east symmetric turning point, the forward and trailing profiles are similar, as expected. The reverse behavior is, however, exhibited (i.e., the trailing profile is brighter than the forward cloud) for emission 3 (Io phase angle 276.6°), emission 4 (Io phase angle 87.7°), and emission 6 (Io phase angle 294.7°). For all three of these observations, it should be noted in Table 2 that the directional feature in the trailing cloud is at or near the null location and, in addition, that higher-speed sodium is detected in the line profile by an enhanced full width half maximum (FWHM) in the trailing cloud profile but not in the forward cloud. For these three observations, the directional feature at the null location therefore provides an explanation for both the enhanced trailing brightness profile and the enhanced FWHM of the line profile in the trailing cloud. It should be noted that emission 5 (Io phase angle 100.6°), which was acquired only about 1.5 hours after emission 4 (i.e., 42.4° later in Io System III longitude), exhibits no enhancement in the FWHM of the line profile in the trailing cloud as might be expected since the directional feature would then be inclined somewhat to the south. Interestingly, emission 9 (Io phase angle 143.1°) which exhibits the normal behavior of a more dominant forward cloud also has a directional feature

at the null condition but does not exhibit any FWHM enhancement in the line profile of the trailing cloud. This may perhaps be caused by the large departure (i.e., 53.1°) of the satellite from eastern elongation where projection effects on the sky plane and the reduction in the solar resonance scattering intensity due to the smaller sunward velocities of the sodium atoms may play a role.

An additional comparison for nearly mirror image observations of the sodium cloud on the sky plane can be made using Table 3 for emission 7 (Io phase angle 117.2°) and emission 6 (Io phase angle 294.7°). The brightness of the forward cloud at a distance of $10\text{-}16 R_{\text{Io}}$ can be seen to be larger for Io east of Jupiter, which is consistent with the well known east-west intensity asymmetry first discovered near Io by Bergstrahl *et al.* (1975, 1977) and more recently identified at larger distances from Io by Goldberg and Smyth (1996). This intensity asymmetry is caused by an east-west asymmetry in the plasma torus properties. A similar mirror image comparison between emission 4 (Io phase angle 87.7°) and emission 3 (Io phase angle 276.6°) is not considered due to the questions of an absolute calibration for emission 3 (Schneider 1990, private communication).

For the power-law fit analysis of the nine emission observations in Table 3, the spatially-projected locations of the forward cloud (F), the symmetric turning point (S) of the cloud, and the trailing cloud (T) are identified for the east and west profiles. The power law slopes of all the forward clouds are similar and have an exponent value of ~ 1.6 . The power law slopes of the trailing clouds after the symmetric turning point, but excluding the September 14 emission 5 observation (Io phase angle 100.6°) acquired 1.5 hours after the null condition, are also similar and have a steeper slope with an exponent value of ~ 2.0 . The power law slopes of the clouds at the symmetric turning point, excluding the September 14 emission 4 observation (Io phase angle 87.7°) at the null condition, are similar and have an exponent value of ~ 1.8 . The two power law slopes of the trailing clouds on September 14 (emission 4 and 5) do not follow the pattern and have smaller exponent values of ~ 1.23 and 1.27 . The less steep behavior of these trailing profiles is due to the enhancement of the directional feature at the null condition (emission 4) and to its fading presence 1.5 hours later (emission 5). Not including the two emission observations on August 27

for Io east of Jupiter, which are at or near the symmetric turning point and have the reverse east-west projected orientation of their forward and trailing clouds, the remaining five profiles for Io east of Jupiter are presented graphically in Figure 3 along with their power law fits in Table 2.

For the forward cloud in Figure 3, the emission brightness profiles are fairly tightly confined and can be seen to have a slightly less steep slope than the shaded area as determined from the sodium cloud images. The lower boundary of the shaded area intersects the emission data profiles just inside of $10 R_{Io}$, which is near the Lagrange radius of Io where the slope of the eclipse data in Figure 2 appears to become less steep. For Io near the elongation point, only two emission profiles occur and are too short to overlap the sodium cloud image area, with the one for an Io phase angle of 87.7 degrees extending only to a west distance of $\sim 10 R_{Io}$ and the other for an Io phase angle of 100.6 degrees containing only one point at a west distance of $\sim 15 R_{Io}$. For Io somewhat beyond eastern elongation, the remaining three emission data profiles (i.e., for Io phase angles of 117.2, 121.6, and 143.1 degrees) extend to $\sim 30 R_{Io}$ and fall slightly below the sodium cloud image profile area, which is more representative of conditions near elongation.

For the trailing cloud in Figure 3, the emission data profiles have significantly different slopes and completely overlap the two shaded areas as determined from the sodium cloud image data. The brightest and least steep of these profiles is for the emission 4 (Io phase angle 87.7°) which has a power law fit that is along the top boundary of the upper area for the sodium cloud image data. This trailing cloud emission profile was acquired for the directional feature at the null condition and exhibited a much larger FWHM value in the trailing cloud line profile for the data points at these larger distances from Io. The next brightest profile is for the emission 5 (Io phase angle 100.6°) which was acquired ~ 1.5 hours later on the same day and does not show an asymmetry in the FWHM value. This trailing cloud emission profile has a power law fit that is essentially along the top boundary of the lower area for sodium cloud image data (corresponding to inclined directional features) and suggest that the fading presence of the directional feature is still present. The remaining three trailing emission profiles (i.e., Io phase angles of 117.2, 121.6, and

143.1°) are for Io somewhat beyond eastern elongation and lie near or just below the bottom boundary of the lower area for sodium cloud images. These three profiles are rather tightly confined and have a very similar slope (exponent ~2) as noted earlier.

4. ANALYSIS OF THE OBSERVATIONS

Modeling analysis of the one-dimensional sodium distribution described in the previous section will now be undertaken. Collectively, the eclipse measurements for the corona near Io, the emission measurements that extend into the near sodium cloud, and the sodium cloud image derived profiles that reach to distances of $\pm 100 R_{Io}$, provide a set of spatially overlapping observations that will be used to study and constrain the initial velocity dispersion of the sodium source atoms at the exobase. In the modeling analysis, one-dimensional profiles are calculated using the numerical sodium cloud model of Smyth and Combi (1988a,b), where the electron impact ionization sink for sodium is determined for a 7 degree tilted corotating plasma torus with an offset-dipole planetary magnetic field in the presence of a nominal (i.e., $\sim 2.8 \text{ mV m}^{-1}$ in Io's frame) east-west electric field. A System III longitudinal asymmetry, although present in the torus ion emission, is not included but deferred to a later time when the electron dependence is available.

To investigate the nature of the initial velocity dispersion of the sodium source, two different source flux speed distributions discussed earlier by Smyth and Combi (1988b; see their Appendix D) are considered: (1) a Maxwell-Boltzmann flux distribution and (2) a modified-sputtering flux distribution. The Maxwell-Boltzmann flux distribution $\phi(v;T)$ is based on the Maxwell-Boltzmann velocity distribution and is defined as follows:

$$\phi(v;T) = \phi_0 \left(\frac{R_s}{R_E} \right)^2 \frac{2}{v_T} \left(\frac{v}{v_T} \right)^3 e^{-\left(\frac{v}{v_T} \right)^2} \quad (1)$$

where $v_T = \sqrt{2kT/m}$ is the most probable speed of the velocity distribution for an atom of mass m . The Maxwell-Boltzmann flux distribution is proportional to the local velocity integrated flux ϕ_0

referenced here to the satellite radius R_s not the exobase radius R_E and depends upon one parameter, the exobase temperature T (or alternatively v_T), which determines both the most probable speed $v_m = \sqrt{3kT/m}$ of the flux distribution and the speed dispersion of the flux distribution. The modified-sputtering flux distribution $\phi(v; \alpha, v_M, v_b)$ is proportional to the local velocity integrated flux ϕ_0 and depends upon three parameters: an exponent α , a velocity parameter v_b , and the velocity parameter v_M :

$$\phi(v; \alpha, v_M, v_b) = \phi_0 \left(\frac{R_s}{R_E} \right)^2 \frac{1}{v_b D(\alpha, v_M/v_b)} \left(\frac{v}{v_b} \right)^3 \left(\frac{v_b^2}{v^2 + v_b^2} \right)^\alpha \left[1 - \left(\frac{v^2 + v_b^2}{v_M^2} \right)^{1/2} \right] \quad (2)$$

where $D(\alpha, v_M/v_b)$ is a normalization constant (see Smyth and Combi 1988b). The exponent α primarily determines the dispersion of the distribution, which has a greater high-speed population as α decreases. The exponent α has a value of 3 for a classical sputtering distribution (i.e., a complete collisional cascade process) and a value of 7/3 for a Thomas-Fermi modified-sputtering flux distribution (i.e., the limit of a single elastic collisional ejection process), where the latter distribution is based upon a Thomas-Fermi differential scattering cross section. The velocity parameter v_b is related nonlinearly to the most probable speed v_m of the flux speed distribution and primarily determines v_m (see Smyth and Combi 1988b, Appendix D). The velocity parameter v_M primarily determines the maximum speed for the flux distribution and depends upon the maximum relative speed (and masses) of the plasma torus ion and sodium atom. For different values of their parameters, two Maxwell-Boltzmann flux distributions and three modified-sputtering flux distributions are shown in Figure 5 and will be utilized in the subsequent modeling analysis.

In calculating the column density and the D_2 emission brightness in the numerical sodium cloud model, a smaller two-dimensional sky-plane grid centered on Io ($\pm 15 R_{Io}$) is used to cover a spatial scale near the satellite more appropriate to the eclipse data while a much larger two-

dimensional sky-plane grid centered on Io is used to cover a larger spatial scale more appropriate for the emission data and the sodium cloud image data. A one-dimensional profile for the eclipse data is obtained from the smaller two-dimensional sky-plane grid by extracting an average radial profile. This average radial profile will be called the calculated eclipse profile and will be denoted by the filled circles in Figures 6-9. A one-dimensional east-west D2 brightness profile (and also a corresponding column density profile) for the emission data and the sodium cloud image data is obtained from the larger two-dimensional sky-plane grid by selecting only the east-west grid elements that occur in the grid row containing Io. In Figures 6-9, the calculated east-west brightness and column density profiles are denoted by filled triangles for the forward cloud profile and by filled squares for the trailing cloud profile. To construct an eclipse or east-west profile, monoenergetic model calculations are performed for 18 different nonuniformly-spaced speeds ranging from 0.4 km sec^{-1} to 10 km sec^{-1} . Profiles for speeds beyond 10 km sec^{-1} are determined by an inverse speed extrapolation of the model results. The individual profiles for the different speeds are appropriately weighted for a given source flux speed distribution and then added to obtain the final spatial profile. Model calculations are performed for an Io geocentric phase angle of 92.9 degrees and an Io System III longitude angle of 48.6 degrees. These satellite conditions are similar to those for the emission 4 and eclipse 2 observations of Table 2, which are the observation closest to the eastern elongation point. This choice is also appropriate for all the eclipse data within the Lagrange sphere, which has no discernible dependence on these two Io related angles, and for the Io sodium cloud image data which have east-west profile areas in Figure 4 that are representative of the satellite near its orbital elongation points. Modeling analysis results are summarized in Table 5 and discussed below.

For the first Maxwell-Boltzmann flux distribution in Figure 5 with a most probable speed of $v_m = 1.3 \text{ km sec}^{-1}$ (i.e., an exobase temperature of $\sim 1560 \text{ K}$) and with a flux ϕ_0 of $3.0 \times 10^8 \text{ atoms cm}^{-2} \text{ sec}^{-1}$ (i.e., a total source of $\sim 1.2 \times 10^{26} \text{ atoms sec}^{-1}$), the model calculated eclipse profile (filled circles) in Figure 6a provides an excellent fit within the Lagrange sphere to the

eclipse observations (open circles) and also compares very favorably with the east-west column density profiles calculated for the forward (filled triangle) and trailing cloud (filled squares). This fit verifies and is similar to the earlier 1500 K Maxwell-Boltzmann flux distribution fit of Schneider *et al.* (1991) discussed in Section 2. Beyond the Lagrange sphere in Figure 6a, however, all three of these calculated profiles fall below the eclipse observations, which is considered less accurate at these distances. At and beyond about $8 R_{Io}$, the calculated east-west forward (filled triangle) and trailing (filled squares) profiles rise above the calculated eclipse profile (filled circles) because the column density is no longer spherically symmetric about Io , with the forward cloud profile having the largest column density and showing a distinct change in its slope compared to the trailing cloud profile. The corresponding model profiles for the D_2 emission brightness are given in Figure 7a. For both the forward and trailing profiles, the calculated eclipse and calculated east-west profiles are in good agreement with each other inside the Lagrange radius, with a maximum brightness of about 200 kR near the exobase. The calculated east-west profile threads the three emission 4 data points for the forward cloud, but falls well below the emission 4 data points in the trailing cloud. For both the forward and trailing clouds at larger radial distances, the calculated east-west profiles fall well below the areas for both the forward and trailing cloud images. This behavior indicates that there is a large deficiency in the high-speed population of this source flux speed distribution at the exobase.

Model calculations were therefore performed for the second Maxwell-Boltzmann flux distribution in Figure 5 with a higher most probable speed of $v_m = 2.0 \text{ km sec}^{-1}$ (i.e., an exobase temperature of $\sim 3690 \text{ K}$) and with a flux ϕ_0 of $1.8 \times 10^8 \text{ atoms cm}^{-2} \text{ sec}^{-1}$ (i.e., a total source of $\sim 0.75 \times 10^{26} \text{ atoms sec}^{-1}$) and are shown in Figure 6b and Figure 7b. For the D_2 emission brightness profiles in Figure 7b, the calculated east-west profile now threads the center of the forward cloud image area for a radial distance up to about $70 R_{Io}$ and the lower trailing cloud image area for a radial distance of about $25 R_{Io}$ before it falls off too steeply. This improved fit at larger radial distances, however, reduces the D_2 emission brightness at the exobase to about 80 kR in

Figure 7b and causes the calculated eclipse profile in Figure 6b to fall below the measured eclipse profile for radial distances inside of about $3 R_{Io}$. The Maxwell-Boltzmann flux distribution therefore cannot fit both the corona profile near Io and the sodium cloud east-west profiles at large distances from the satellite. A flux distribution that has a broader dispersion with enhanced populations for both the low-speed and high-speed atoms is required. The three modified-sputtering flux distributions in Figure 5, which have a broader dispersion, are thus considered in the remainder of the paper with model calculations presented in Figures 8 and 9.

Model calculations for a classical sputtering flux distribution ($\alpha=3$) and a modified-sputtering flux distribution ($\alpha=7/3$) are presented in Figure 8a and Figure 8b for the eclipse observations and in Figure 9a and Figure 9b for the east-west D₂ emission brightness profiles. For these two flux distributions, the most probable speeds are, respectively, 1.0 km sec^{-1} and 0.5 km sec^{-1} , and the sodium fluxes ϕ_0 are, respectively, $3.2 \times 10^8 \text{ atoms cm}^{-2} \text{ sec}^{-1}$ (i.e., a total source of $\sim 1.3 \times 10^{26} \text{ atoms sec}^{-1}$) and $4.2 \times 10^8 \text{ atoms cm}^{-2} \text{ sec}^{-1}$ (i.e., a total source of $\sim 1.7 \times 10^{26} \text{ atoms sec}^{-1}$). From the exobase to radial distances of $\sim 8 R_{Io}$, just beyond the Lagrange radius, both sputtering flux distributions provide a very good fit in Figures 8a and 8b to the observed eclipse column density profile (open circles) and correspond to an exobase D₂ emission brightness of about 150 kR in Figures 9a and 9b. For the classical sputtering flux distribution in Figure 9a, the calculated D₂ emission brightness profile for the forward profile is slightly above the measured data point (open circles) inside the Lagrange radius, matches the two measured data points beyond the Lagrange radius, and then threads the forward cloud image area nicely between about $20 R_{Io}$ and $80 R_{Io}$ before it falls too rapidly and drops below this area. An excellent fit for the forward profile is, however, provided by the modified sputtering distribution ($\alpha=7/3$) in Figure 9b where the calculated D₂ emission brightness profile matches the measured data points (open circles) both inside and beyond the Lagrange radius as well as nicely threading the forward cloud image area all the way to $100 R_{Io}$. For the trailing cloud, the calculated D₂ emission brightness profile for the classical sputtering flux distribution in Figure 9a, matches the measured data point

inside the Lagrange radius, is slightly below the two measured data points outside the Lagrange radius, and then threads the lower of the two trailing cloud image areas nicely between about $15 R_{Io}$ and $35 R_{Io}$ before it falls too rapidly and drops below this area.. An excellent fit for the trailing profile is, however, provided by the modified sputtering distribution ($\alpha=7/3$) in Figure 9b where the calculated D_2 emission brightness matches the measured data point inside the Lagrange radius, is slightly below the two measured data points outside the Lagrange radius, and then threads the lower (non-null) trailing cloud image area nicely all the way to $100 R_{Io}$. It is particularly noteworthy that the isotropic ejection of sodium from the exobase with a modified sputtering flux distribution with $\alpha=7/3$ provides an complete fit to the combined eclipse, emission, and forward/trailing sodium cloud image profile data for this non-null condition from 1.4 to $100 R_{Io}$.

In order to fit the trailing cloud (upper area) profile for the directional feature at the null condition, it is then clear that a flux distribution is required with an even more enhanced higher-speed population ($\sim 20 \text{ km sec}^{-1}$) than the modified sputtering flux distribution with $\alpha=7/3$. Since the modified sputtering flux distribution for $\alpha=7/3$ corresponds to the limit of a single collision cascade process described by a Thomas-Fermi cross section (see Smyth and Combi 1988b), reducing the value of α to a smaller value becomes somewhat physically questionable but will be used here for the purposes of simply illustrating the impact of a more enhanced higher-speed sodium population in the model calculation. As discussed earlier, this higher-speed sodium is thought to be a nonisotropic ejection from Io's exobase which is attributed to some combination of direct collision ejection and lower-velocity charge exchange ejection. Choosing the modified sputtering flux distribution with $\alpha=2$ in Figure 5 which has a most probable speed of 0.4 km sec^{-1} and selecting an isotropic exobase source rate of $1.9 \times 10^{26} \text{ atoms sec}^{-1}$ (i.e., a flux ϕ_0 of $4.7 \times 10^8 \text{ atoms cm}^{-2} \text{ sec}^{-1}$), the model-data comparison is shown in Figure 8c for the eclipse column density and in Figure 9c for the east-west D_2 emission brightness. The sputtering flux distribution provides a reasonably good fit to the observed column density data points in Figure 8c with only a

small departure very near the exobase and produces a column density profile beyond $10 R_{Io}$ that is significantly enhanced compared to the $\alpha=7/3$ case in Figure 8b. In Figure 9c, this enhancement in the forward cloud is obvious where the calculated D_2 emission brightness profile is significantly above the measured data points both inside and outside the Lagrange radius and is above or in the very top of the forward cloud image area all the way to $100 R_{Io}$. The additional enhanced high-speed population of the $\alpha=2$ modified sputtering flux distribution is too large and therefore not consistent with the observed forward profile. In contrast for the trailing cloud in Figure 9c, the calculated D_2 emission brightness profile matches the measured data points inside and outside of the Lagrange radius very well and then threads the upper of the two trailing cloud image areas nicely all the way to $\sim 90 R_{Io}$. This demonstrates that the trailing cloud can be fitted with an enhanced higher-speed population of sodium atoms in the flux distribution. It also immediately demonstrates that the flux distribution at the exobase must be nonisotropic with some of the enhanced high-speed population weighted more toward vector directions that will preferentially populate the trailing cloud rather than the forward cloud. As discussed in section 2, this nonisotropic requirement for a flux distribution for speeds of $\sim 20 \text{ km sec}^{-1}$ is consistent with the conclusion reached by earlier modeling analyses (Pilcher *et al.* 1984; Smyth and Combi 1991; Wilson and Schneider 1995) where sodium was constrained to be initially directed at near right angles to Io's orbital motion and hence was angularly deficient in the trailing apex direction, which preferentially populates the forward cloud.

5. DISCUSSION AND CONCLUSIONS

The composite spatial information for sodium obtained by combining the eclipse observations (radial distances from Io of 1.4 to $\sim 10 R_{Io}$), the emission observations (east-west distances of ± 4 to $\pm 30\text{-}40 R_{Io}$) and the sodium cloud observations (east-west distances of ± 10 to $\pm 100 R_{Io}$) has been analyzed to extract a basic description for the flux speed distribution at the satellite's exobase. An isotropic modified-sputtering flux speed distribution in Figure 5 with $\alpha=7/3$, a most probable speed of 0.5 km sec^{-1} , and a source strength of $1.7 \times 10^{26} \text{ atoms sec}^{-1}$

provided a very good fit to these composite observations when the directional feature is either north or south and hence not contributing to the east-west profile of the trailing cloud. It is remarkable that these observations, acquired by a number of ground-based programs over very different spatial scales and at different times during the 1975-1985 decade, are so self consistent. Near Io, the two-dimensional sodium column density produced by this modified sputtering distribution as calculated by the sodium cloud model in the profile analysis above is shown in Figure 10 and can be seen at larger distances from Io to become nonspherical and more confined near the satellite plane. This flattening near the satellite plane is the merging of the near Io corona into the sodium cloud and is caused naturally by orbital dynamics beyond the satellite Lagrange sphere where the gravity of Jupiter is dominant. The forward cloud portion of the east-west emission data profiles has a rather tightly confined slope that, in the absence of the trailing cloud enhancement at the null condition, is less steep and is brighter than the trailing cloud profiles. In order, however, to reproduce the extended east-west profile in the trailing sodium cloud when the directional feature is in the satellite plane (i.e., the null location), additional nonisotropic high-speed sodium is required.

The sodium atoms ejected from Io's exobase as described above by the modified sputtering flux distribution have speeds primarily in the range from 0 to a few 10's km sec⁻¹. This neutral flux distribution represents the spatially integrated effect of the incomplete collisional cascade process that occurs from the collisional interactions of heavy ions in the corotating plasma torus with neutrals in Io's atmosphere. This flux speed distribution can be alternatively described as a source rate speed distribution by multiplying it by the satellite surface area. In addition to these ion-neutral elastic collisional encounters, resonance charge exchange between plasma torus sodium ions and neutral sodium in Io's atmosphere (i.e., $\text{Na} + \text{Na}^+ \rightarrow \text{Na}^+ + \text{Na}$) is also responsible for producing a sodium source with higher speeds relative to Io. These speeds are centered about the corotational ion speed (~ 57 km sec⁻¹) relative to Io's motion and have a dispersion reaching from several 10's km sec⁻¹ to ~ 100 km sec⁻¹. Such high speed sodium (≤ 80 km sec⁻¹) has recently been observed near Io by Cremonese *et al.* (1992). As discussed in section 2, this higher-speed

nonisotropic source of sodium together with the lower speed ($\sim 15\text{-}20 \text{ km sec}^{-1}$) nonisotropic source for the directional feature is the source for the sodium zenocorona or magneto-nebula observed to distances of $\sim 400\text{-}500$ planetary radii from Jupiter. Earlier modeling studies (Smyth and Combi 1991; Flynn *et al.* 1992) indicated that the higher-speed source was $\sim 2 \times 10^{26}$ atoms sec^{-1} while the lower speed source was $\sim 1 \times 10^{26}$ atoms sec^{-1} . More recent observations and analysis (Flynn *et al.* 1994) have shown that the source strength for the higher-speed sodium source is time variable with values usually in the range $\sim 2\text{-}4 \times 10^{26}$ atoms sec^{-1} . A typical total source rate speed distribution for sodium at Io's exobase has hence been constructed by combining the modified sputtering source rate distribution determined in this paper with the two source rate distribution for the zenocorona as given by Smyth and Combi (1991). This total source rate speed distribution function is shown in Figure 11, where the lower (solid line) and upper (dashed line) curves correspond, respectively, to the sodium zenocorona higher-speed source rate of 2.2×10^{26} atoms sec^{-1} and 4×10^{26} atoms sec^{-1} . Total source rate speed distribution functions at Io's exobase expected for other atomic species, such as K, O, and S, can be constructed in a similar fashion to sodium by adopting the estimated source rates given by Smyth and Combi (1991).

Future studies for the sodium flux speed distribution at Io's exobase are anticipated using a much larger data set for east-west sodium emission observations (~ 100 profiles; Schneider 1993, private communication) acquired in 1987 and also a data set for north-south sodium emission observations (~ 140 profiles; Trafton 1995, private communication). From this much larger data base, it will be possible to analyze the combined spatial and spectral information and to refine the nonisotropic nature of the flux distribution and also to search for possible east-west and System III modulations in the flux speed distribution. Once this information is determined for sodium, the implications for the more abundant species in Io's atmosphere will be particularly important in other related studies for the many faceted and complex phenomena in the Io-Jupiter system.

ACKNOWLEDGMENTS

We are grateful to N. M. Schneider for helpful discussions and for providing the numerical data for the 1985 emission observations. This research was supported by the Planetary Atmospheres Program of the National Aeronautical and Space Administration under grant NAGW-3585 to the University of Michigan and under contracts NASW-4416, NASW-4471, and NASW-4804 to Atmospheric and Environmental Research, Inc.

REFERENCES

- Bergstralh, J. T., D. L. Matson, and T. V. Johnson 1975. Sodium D-Line Emission from Io: Synoptic Observations from Table Mountain Observatory. *Astrophys. J. Lett.* **195**, L-131-L135.
- Bergstralh, J. T., J. W. Young, D. L. Matson, and T. V. Johnson 1977. Sodium D-Line Emission from Io: A Second Year of Synoptic Observation from Table Mountain Observatory. *Astrophys. J. Lett.* **211**, L51-L55.
- Brown, R. A. 1974. Optical Line Emission from Io. In *Exploration of the Planetary System*. Proceedings IAU Symp. No. 65. Torun, Poland, September 5-8, 1973. (A. Woszczyk and C. Iwaniszewska, Eds.), pp. 527-531. D Reidel Publ. Co., Dordrecht.
- Brown, R. A., and Y. L. Yung 1976. Io, Its Atmosphere and Optical Emissions. In *Jupiter Studies of the Interior, Atmosphere, Magnetosphere, and Satellites* (T. Gehrels, Ed.), pp. 1102-1145. Univ. of Arizona Press, Tucson.
- Carlson, R. W., D. L. Matson, and T. V. Johnson 1975. Electron Impact Ionization of Io's Sodium Emission Cloud, *GRL* **2**, 469-472.
- Cremonese, G., N. Thomas, C. Barbieri, and C. Pernechele 1992. High Resolution Spectra of Io's Neutral Sodium Cloud, *Astron. Astrophys.* **256**, 286-298.
- Fang, T.-M., W. H. Smyth, and M. B. McElroy 1976. The Distribution of Long-Lived Gas Clouds Emitted by Satellites in the Outer Solar System, *Planet. Space Sci.* **25**, 577-588.

- Flynn, B., M. Mendillo, and J. Baumgardner 1992. Observations and Modeling of the Jovian Remote Sodium Emission: *Icarus* **99**, 115-130.
- Flynn, B., M. Mendillo, and J. Baumgardner 1994. The Jovian Sodium Nebula: Two Years of Ground-Based Observations. *J. Geophys. Res.* **99**, 8403-8409.
- Goldberg, B. A., R. W. Carlson, D. L. Matson, and T. V. Johnson 1978. A New Asymmetry in Io's Sodium Cloud, *BAAS* **10**, 579.
- Goldberg, B. A., Yu. Mekler, R. W. Carlson, T. V. Johnson, and D. L. Matson 1980. Io's Sodium Emission Cloud and the Voyager 1 Encounter. *Icarus* **44**, 305-317.
- Goldberg, B. A., G. W. Garneau, and S. K. LaVoie 1984. Io's Sodium Cloud. *Science* **226**, 512-516.
- Goldberg, B. A., and W. H. Smyth 1996. The JPL Table Mountain Io Sodium Cloud Data Set. Paper in preparation.
- Ip, W.-H. 1990. Neutral Gas-Plasma Interaction: The Case of the Plasma Torus, *Adv. Space Res.* **10**, 15-23.
- Macy, W. W., Jr., and L. M. Trafton 1980. The Distribution of Sodium in Io's Cloud: Implications. *Icarus* **41**, 131-141.
- Matson, D. L., B. A. Goldberg, T. V. Johnson, and R. W. Carlson 1978. Images of Io's Sodium Cloud. *Science* **199**, 531-533.

- Mendillo, M., J. Baumgardner, B. Flynn and W. J. Hughes 1990. The Extended Sodium Nebula of Jupiter. *Nature*, **348**, 312-314.
- McGrath, M. A. 1988. Ion Bombardment of Io and Mercury, Ph.D. Thesis, Dept. of Astronomy, University of Virginia.
- Murcray, F. J. 1978. Observations of Io's Sodium Cloud, Ph. D. Thesis, Dept. of Physics, Harvard University.
- Murcray, F. J., and R. M. Goody 1978. Pictures of the Io Sodium Cloud. *Ap. J.*, **226**, 327-335.
- Pilcher, C. B., W. H. Smyth, M. R. Combi, and J. H. Fertel 1984. Io's Sodium Directional Features: Evidence for a Magnetospheric-Wind-Driven Gas Escape Mechanism. *Ap. J.*, **287**, 427-444.
- Schneider, N. M. 1988. Sodium in Io's Extended Atmosphere. Ph.D. Thesis, Department of Planetary Sciences, Univ. of Arizona.
- Schneider, N. M., D. M. Hunten, W. K. Wells, and L. M. Trafton 1987. Eclipse Measurements of Io's Sodium Atmosphere. *Science*, **238**, 55-58.
- Schneider, N. M., D. M. Hunten, W. K. Wells, A. B. Schultz, and U. Fink 1991. The Structure of Io's Corona. *Ap. J.*, **368**, 298-315.
- Sieveka, E. M., and R. E. Johnson 1984. Ejection of Atoms and Molecules from Io by Plasma-Ion Impact, *Ap. J.* **287**, 418-426.

- Smyth, W. H. 1979. Io's Sodium Cloud: Explanation of the East-West Asymmetries. *Ap. J.* **234**, 1148-1153.
- Smyth, W. H. 1983. Io's Sodium Cloud: Explanation of the East-West Asymmetries. II. *Ap. J.* **264**, 708-725.
- Smyth, W. H., and M. R. Combi 1987a. Correlating East-West Asymmetries in the Jovian Magnetosphere and the Io Sodium Cloud, *Geophys. Res. Lett.* **14**, 973-976.
- Smyth, W. H., and M. R. Combi 1987b. Time Variability of the Sodium Cloud, poster paper at the international conference "Time-Variable Phenomena in the Jovian System," Flagstaff, AZ August 25-27.
- Smyth, W. H., and M. R. Combi 1987c. Nature of Io's Atmosphere and its Interaction with the Planetary Magnetosphere. *BAAS* **19**, 855.
- Smyth, W. H., and M. R. Combi 1988a. A General Model for Io's Neutral Gas Cloud. I. Mathematical Description. *Ap. J. Supp.*, **66**, 397-411.
- Smyth, W. H., and M. R. Combi 1988b. A General Model for Io's Neutral Gas Clouds. II. Application to the Sodium Cloud. *Ap. J.*, **328**, 888-918.
- Smyth, W. H., and M. R. Combi 1991. The Sodium Zenocorona. *JGR*, **96**, 22711-22727.

- Smyth, W. H., and B. A. Goldberg 1993. The Io Sodium Cloud: Space-Time Signatures of East-West and System III Longitudinal Asymmetries in the Jovian Magnetosphere. Paper presented at the Io: An International Conference, San Juan Capistrano, California, June 22-25.
- Smyth, W. H., and M. B. McElroy 1977. The Sodium and Hydrogen Gas Clouds of Io, *Planet. Space Sci.* **25**, 415-431.
- Smyth, W. H., and M. B. McElroy 1978. Io's Sodium Cloud: Comparison of Models and Two-Dimensional Images. *Astrophys. J.* **226**, 336-346.
- Summers, M. E., D. F. Strobel, Y. L. Yung, J. T. Trauger, and F. Mills 1989. The Structure of Io's Thermal Corona and Implications for Atmospheric Escape. *Ap. J.* **343**, 468-480.
- Trafton, L., and W. Macy, Jr. 1978. On the Distribution of Sodium in the Vicinity of Io, *Icarus* **33**, 322-335.
- Wilson, J. K., and N. M. Schneider 1994. Io's Fast Sodium: Implications for Molecular and Atomic Atmospheric Escape, *Icarus* **111**, 31-44.
- Wilson, J. K., and N. M. Schneider 1995. Io's Sodium Directional Feature: Evidence for Ionospheric Rip-off, *BAAS* **27**, 1154.

Table 1. Summary of Modeling Studies for the Spatial Distribution of Sodium Near Io and its Orbit

Spatial Region	Topic Studied	Sodium Source								Sodium Lifetime		Orbital Dynamics			Reference
		Mono-energetic Atom Ejection	Maxwell-Boltzman Flux Distribution	Cascade Flux Speed Distribution					Angular Nature ^a	Plasma Torus Description	Lifetime (hrs)	Io's Mass Included	Jupiter's Mass Included	Radiation Pressure Included	
		Speed (km s ⁻¹)	T (K)	V _{peak} (km s ⁻¹)	α	V _b (km s ⁻¹)	V _{peak} (km s ⁻¹)	V _{max} (km s ⁻¹)							
I. Corona	e-w intensity asymmetry ^b	2.0-2.6	-	-	-	-	-	-	isotropic	cut-off	20	yes	yes	yes	Smyth 1983
	e-w intensity asymmetry ^b	2.6	-	-	-	-	-	-	isotropic	2-D	variable	yes	yes	yes	Smyth and Combi 1987a
	e-w intensity asymmetry ^b	-	460; 12,300	0.71; 3.65	7/3	<0.4; 2.2	<0.5; 2.9	46.6	band, isotropic	2-D	variable	yes	yes	yes	Smyth and Combi 1988b
	column-density profile ^c	2.6	-	-	-	-	-	-	isotropic	2-D	variable	yes	yes	yes	Smyth and Combi 1987b,c
	column-density profile ^c	-	-	-	3	0 ^d	-	∞	isotropic	cut-off	3, ∞	yes	no	no	McGrath 1988
	column-density profile ^c	-	1000	1.04	-	-	-	-	isotropic	uniform	∞	yes	no	no	Summers et al. 1989
	column-density profile ^c	3.0	-	-	-	-	-	-	isotropic	uniform	?	yes	no	no	Ip 1990
	column-density profile ^c	-	1500	1.28	-	-	-	-	isotropic	uniform	∞	yes	no	no	Schneider et al. 1991
II. Cloud	general spatial nature	3.5	-	-	-	-	-	-	isotropic	uniform	30, 47	yes	yes	no	Carlson et al. 1975
	general spatial nature	-	5000	2.3	-	-	-	-	isotropic	long-lived limit	-	no	yes	no	Fang et al. 1976
	evolution and 2-D nature	2, 3	-	-	-	-	-	-	isotropic	cut-off	50	yes	yes	no	Smyth and McElroy 1977
	1-D brightness morphology ^f	-	-	-	3	4	4	∞	I-L hemisphere ^g	uniform	28	yes	yes	no	Matson et al. 1978
	2-D brightness morphology ^h	2.6, 3	-	-	-	-	-	-	I, I-T hemisphere ⁱ	cut-off	15, 20	yes	yes	no	Smyth and McElroy 1978
	e-w orbital asymmetry ^j	2.6	-	-	-	-	-	-	I-T hemisphere ^l	cut-off	20	yes	yes	yes	Smyth 1979
	radial and vertical structure	(3.5, 7.9, 11, 13) ^k	-	-	-	-	-	-	I hemisphere	uniform	56	no	yes	no	Macy and Trafton 1980
	1-D brightness morphology	-	-	-	3 ^l	4 ^l	4 ^l	∞ ^l	I-L hemisphere ^l	1-D	variable	yes	yes	no	Goldberg et al. 1980
	e-w orbital asymmetry	2.6	-	-	-	-	-	-	I hemisphere	cut-off	20	yes	yes	yes	Smyth 1983
	2-D brightness morphology	2.6	-	-	-	-	-	-	band, isotropic	2-D	variable	yes	yes	yes	Smyth and Combi 1988b
III. Directional Feature	spacetime structure ^m	~20	-	-	-	-	-	-	O, ~1 to Io's motion	2-D	variable	yes	yes	yes	Pilcher et al. 1984
	collision cross sections	-	-	-	3	0 ⁿ	-	-	~1 to Io's motion	-	-	-	-	-	Sieveka and Johnson 1984
	nearer zenocorona structure	-	-	~20± 12 ^p	-	-	-	-	tangential ± isotropic	photoionization	~400 hr	no	no; Sun yes	yes	Smyth and Combi 1991
	spacetime structure	-	-	20± 10-20 ^q	-	-	-	-	tangential ± isotropic	none	∞	no	yes	no	Wilson and Schneider 1995

^a regarding Io's exobase, L=leading, I=inner, T=trailing, O=outer.

^b east-west intensity asymmetry data of Bergstrahl et al. (1975, 1977).

^c early (i.e., partial) Na eclipse data set from Schneider et al. (1987).

^d used cut-off energy: $E_{min} \leq E < \infty$; $E_{min} = k T_{exobase}$; $T_{exobase} = 1500$ K (i.e. a 1.04 km s^{-1} cut-off speed).

^e complete eclipse data set from Schneider (1988) and Schneider et al. (1991).

^f two sodium cloud images of Matson et al. (1978).

^g I-L hemisphere centered 30° longitude (0° longitude facing Jupiter, 90° longitude is the leading point in the orbit).

^h fifty-six sodium cloud images of Murcray (1978) and Murcray and Goody (1978).

ⁱ I-T hemisphere centered on -40° longitude.

^j east-west orbital asymmetry data of Goldberg et al. (1978).

^k velocity components equally weighted.

^l distribution parameters from Carlson (1995, private communication): I-L hemisphere centered on 45° longitude.

^m from images of Pilcher et al. (1984).

ⁿ used cut-off energy of 0.5 eV (i.e., Na cut-off speed of 2.0 km s^{-1}).

^p tangential speed to Io's orbit at Io position ± most probable speed of an isotropic Maxwell-Boltzmann.

^q tangential speed to Io's orbit at Io position ± most probable speed of an isotropic Gaussian.

Table 2

1985 Io Eclipse and Emission Observations

Date	UT Midpoint	Io Geocentric Phase Angle Range (deg)	Io System III Longitude Range (deg)	Spectrum ID	Type of Observation		Dominant Spatial Profile	Directional Feature Orientation	Enhance Doppler Signature	D ₂ Emission Profile Exponent		Power Law Fit ^f Amplitude (kR)	
					Eclipse	Emission				East Profile	West Profile	East Profile	West Profile
August 27	0714	61.4 ± 0.7	29.9 ± 2.3	85g188	1	1	forward	null	trailing/forward	1.67 (F)	1.57 (T)	191	124
	0720	62.3 ± 11.0	32.9 ± 35.8	a			---	---	---				
	0830	72.2 ± 1.1	65.1 ± 3.4	85g196		2	symmetric	south	no	1.85 (S)	1.80 (S)	169	142
September 13	0641	276.6 ± 0.7	194.7 ± 2.3	85h032		3	trailing	null/north	trailing	---	---	---	---
September 14	0245	87.7 ± 0.7	31.4 ± 2.3	85h102	2	4	trailing	null	trailing	1.23 (S/T)	1.80 (S/F)	89	188
	0326	93.5 ± 4.2	50.5 ± 13.7	b			---	---	---				
	0416	100.6 ± 0.4	73.6 ± 1.4	85h113		5	g	south	no	1.27 (T)	---	66	---
September 15	0316	294.7 ± 0.7	353.7 ± 3.0	85h152	3	6	trailing	null	trailing	---	---	---	---
	0500	309.4 ± 11.5	41.7 ± 37.4	c			---	---	---				
September 21	0604	100.5 ± 1.6	112.5 ± 5.2	d	4		---	---	---				
September 23	0230	117.2 ± 0.7	267.6 ± 2.3	85h433	5	7	forward	north	no	2.05 (T)	1.57 (F)	342	135
	0301	121.6 ± 0.4	281.9 ± 1.2	85h436		8	forward	north	no	1.96 (T)	1.54 (F)	283	138
	0356	129.3 ± 2.0	307.3 ± 6.7	e			---	---	---				
	0534	143.1 ± 0.7	352.9 ± 2.3	85h457		9	forward	null	no	2.16 (T)	1.64 (F)	374	165

a. Eclipse 1 : 85g179, 85g181, 85g185, 85g188, 85g192, 85g193, 85g196

b. Eclipse 2 : 85h103, 85h104, 85h105, 85h106, 85h107, 85h108, 85h109, 85h110, 85h112

c. Eclipse 3 : 85h153, 85h154, 85h155, 85h157, 85h159, 85h162, 85h163

d. Eclipse 4 : 85h287, 85h288, 85h289, 85h290, 85h291, 85h292, 85h293, 85h294, 85h295

e. Eclipse 5 : 85h441, 85h442, 85h443, 85h444, 85h445, 85h446, 85h447, 85h448, 85h449, 85h450

f. Profile points inside of 4 R_{Io} are excluded; power law fit $A r^{-\beta}$, where A is the amplitude, β is the exponent, and r is in units of R_{Io}; F = forward cloud; S = symmetric turning point; T = trailing cloud.

g. Not sufficient data west of Io to compare spatial profiles (see Table 3).

Table 3. 1985 Emission Data

Radial Distance From Io (satellite radii)	D ₂ Intensity (kR)								
	Emission 1 61.4° 27 August (85g188)	Emission 2 72.2° 27 August (85g196)	Emission 4 87.7° 14 September (85h102)	Emission 5 100.6° 14 September (85h113)	Emission 7 117.2° 23 September (85h433)	Emission 8 121.6° 23 September (85h436)	Emission 9 143.1° 23 September (85h457)	Emission 3* 276.6° 13 September (85h032)	Emission 6 294.7° 15 September (85h152)
↑ West	-29.92				0.69 ± 0.17	0.93 ± 0.18	0.66 ± 0.16		1.12 ± 0.19
	-29.65							1.40 ± 0.21	
	-24.48				1.19 ± 0.19	0.84 ± 0.17	0.95 ± 0.18	2.22 ± 0.27	
	-21.76				1.38 ± 0.20	2.10 ± 0.26	1.74 ± 0.23		2.15 ± 0.26
	-16.32			1.91 ± 0.24					
	-15.78								
	-14.96								
	-10.88	3.16 ± 0.35			2.90 ± 0.33	3.29 ± 0.36	3.38 ± 0.37	4.40 ± 0.46	
	-9.52		3.17 ± 0.35						
	-6.80	5.21 ± 0.54	4.50 ± 0.47	6.41 ± 0.66	7.49 ± 0.76	7.76 ± 0.79		11.54 ± 1.16	
Io	-4.08	14.65 ± 1.47	11.29 ± 1.14	14.71 ± 1.48			7.54 ± 0.77	28.69 ± 2.87	
	-3.81								18.75 ± 2.63
	-2.18	24.31 ± 3.40	18.39 ± 2.57	24.12 ± 3.38	25.61 ± 3.59	25.01 ± 3.50	21.00 ± 2.94	45.47 ± 6.37	
	-1.09	27.46 ± 3.84	19.99 ± 2.80	27.14 ± 3.80	29.95 ± 4.19	28.72 ± 4.02	23.89 ± 3.34	48.61 ± 6.81	
	-0.82								24.85 ± 3.48
	0.00	27.44 ± 3.84	19.19 ± 2.69	27.14 ± 3.80	27.90 ± 3.91	30.16 ± 4.22	23.97 ± 3.36	45.56 ± 6.38	
	0.27								25.27 ± 3.54
	1.09	25.87 ± 3.62	19.35 ± 2.71	26.65 ± 3.73	23.03 ± 3.22	26.31 ± 3.68	22.84 ± 3.20	39.45 ± 5.52	
	1.36								22.90 ± 3.21
	2.18	25.19 ± 3.53	16.87 ± 2.36	25.68 ± 3.60	19.60 ± 2.74	22.42 ± 3.14	23.91 ± 3.35	33.60 ± 4.70	
East ↓	3.26								11.53 ± 1.61
	4.08	17.60 ± 1.77	11.92 ± 1.20	18.10 ± 1.82	11.87 ± 1.20	15.54 ± 1.56	14.83 ± 1.49	12.52 ± 1.26	20.06 ± 2.01
	5.98								4.79 ± 0.50
	6.80	8.31 ± 0.84	5.52 ± 0.57	8.17 ± 0.83	5.52 ± 0.57	7.09 ± 0.72	7.10 ± 0.73	6.02 ± 0.62	7.52 ± 0.77
	10.06								1.66 ± 0.22
	10.88	3.40 ± 0.37	1.94 ± 0.25	3.84 ± 0.41	3.21 ± 0.35	2.47 ± 0.29	2.47 ± 0.29	2.26 ± 0.27	2.73 ± 0.31
	15.50								0.77 ± 0.17
	16.32			2.84 ± 0.32	1.81 ± 0.24	1.03 ± 0.18	1.11 ± 0.19	0.82 ± 0.17	
	21.76			2.25 ± 0.27		0.68 ± 0.16	0.75 ± 0.17	0.52 ± 0.16	
	23.66				1.24 ± 0.19				0.53 ± 0.16
	24.48							1.06 ± 0.18	
	27.20		1.39 ± 0.21						
	35.36		1.27 ± 0.20					1.00 ± 0.18	
	46.24							0.83 ± 0.17	

*calibration uncertain

Table 4
East-West D₂ Brightness Profiles for Sodium Cloud Image Data

UT Date	UT Time	Image ID Number	Io Geocentric Phase Angle (deg)	Io System III Longitude (deg)	East-West Distance from Io for Specified D ₂ Brightness Level (satellite radii)							
Image Data Set Reference: Murcay (1978)					0.5 kR		1.0 kR		1.5 kR		2.0 kR	
					Forward	Trailing	Forward	Trailing	Forward	Trailing	Forward	Trailing
1976 Nov. 16	0806	ES 328B	256	262	--	--	51	29	46	24	28	14
1977 Jan 27	0024	ES 369A	86	193	60	38	50	22	44	19	32	16
	0217	ES 370D	102	245	>83	30	56	25	46	21	24	19
Image Data Set Reference: Goldberg and Smyth (1996)					0.2 kR		0.5 kR		1.0 kR		2.0 kR	
					Forward	Trailing	Forward	Trailing	Forward	Trailing	Forward	Trailing
1981 May 5	0819	SIP 418/31-33	102	300	78	69	63	40-66	45	37	24	21
May 12	0848	SIP 420/30-32	91	302	66	86	41	37	35	29	20	21
May 13	0346	SIP 421/21-23	253	108	74-103	73	70	41	41	27	29	20
	0555	SIP 421/32-33	271	168	124	65	112	44	51	30	26	19
June 6	0436	SIP 424/10-12	103	300	81	75	68	71	36	26	20	23
Image Data Set Reference: Morgan (1984)					0.3 kR		0.6 kR		0.9 kR		1.8 kR	
					Forward	Trailing	Forward	Trailing	Forward	Trailing	Forward	Trailing
1983 June 13	0714	i 8492	274	230	--	39	58	26	37	19	20	--
	0722	i 8494	275	233	--	35	52	22	40	20	20	--
	0729	i 8496	276	237	>93	36	52	22	37	17	22	--
	0827	i 8501	284	264	>93	39	61	25	42	19	23	--
	0949	i 8509	296	301	>93	47	63	26	44	17	24	--
	1010	i 8511	299	311	>93	41	63	23	44	16	19	--

Table 5
SUMMARY COMPARISON OF MODELED AND OBSERVED EAST-WEST SODIUM PROFILES
FOR DIFFERENT FLUX SPEED DISTRIBUTIONS AT IO'S EXOBASE

		Corona	Forward Cloud		Trailing Cloud (not null)		Trailing Cloud (null)		
Observations: E/W Radial Interval (R_{Io}):		1.4-6	6-10	10-100	6-10	10-100	6-10	10-100	
Distribution Speed Peak (km/s)	Exobase Source Rate (10^{26} atoms/s)	Fits Eclipse Column Profile	Fits Near Io Emission Profile	Fits Far Cloud E/W Profile	Fits Near Io Emission Profile	Fits Far Cloud E/W Profile	Fits Near Io Emission Profile	Fits Far Cloud E/W Profile	
1. <u>Maxwell Boltzmann Flux Distribution</u>									
1.3	1.24	YES	YES	too low	little low	too low	too low	too low	
2.0	0.75	too low	YES	slightly low	YES	little low	little low	too low	
2. <u>Collisional Cascade Flux Distribution</u>									
(classical sputtering)									
$\alpha = 3$	1.0	1.32	YES	YES	tiny low	YES	tiny low	little low	too low
(incomplete cascade: higher velocity tail)									
$\alpha = 7/3$	0.5	1.74	YES	YES	YES	YES	YES	little low	too low
$\alpha = 2$	0.4	1.90	tiny low	too high	too high	too high	too high	YES	YES

FIGURE CAPTIONS

FIG. 1. Io Sodium Cloud Images. Three calibrated D₂ emission images of the Io sodium cloud from the JPL Table Mountain Data Set are shown to proper scale with Jupiter and Io's orbit as viewed from earth in 1981 (Smyth and Goldberg 1993). The Io System III longitude and corresponding orientation of the trailing directional feature in image A are 247 degrees and north, in image B are 104 degrees and south, and in image C are 178 degrees and only very slightly north. An east-west spatial scale of ± 100 planetary radii about Io is shown for reference, with tick marks located at ± 50 planetary radii. Contour levels for the D₂ brightness, from outside to inside, are 0.2, 0.5, 1, 2, 4, 6, 8, and 10 kR. A occulting mask of $\sim 10 R_{\text{Io}}$ in radius is centered on Io so that brightness values within this distance are not accurate.

FIG. 2. 1985 Eclipse Data. The sodium column density is shown as a function of the radial distance from the center of Io for the five eclipse measurements acquired by Schneider *et al.* (1991). The position of the nominal exobase and the average Lagrange radius are indicated. The dashed line is a fit to the data (see text).

FIG. 3. 1985 Emission Data Profiles. The sodium D₂ emission brightness in units of kiloRayleighs is shown as a function of the east-west distance from the center of Io along the observing slit for the nine emission observations summarized in Table 2 and acquired by Schneider *et al.* (1991).

FIG. 4. East and West Brightness Profiles for Selected 1985 Emission Data and Image Cloud Data. The spatial profiles both east and west of Io for the sodium D₂ emission brightness in units of kiloRayleighs are shown as a function of the distance along the observing slit from the center of Io. Five emission observations identified by their satellite geocentric phase angle are shown by the

different symbols. These five profiles occur when Io is east of Jupiter and just past the satellite phase angle where the forward cloud has its symmetric turning point so that the trailing cloud profiles are all to the east of Io and the forward cloud profiles are all to the west of Io. A power law fit to each profile is also shown. At larger distances from Io, an envelope for the east-west D₂ emission profile acquired from sodium image data is shown by the shaded area. For the trailing profile, the shaded area is divided into two parts, where the lower area corresponds to sodium cloud data when the directional feature is oriented either north or south and where the upper area corresponds to the directional feature oriented along the east-west direction (i.e., the null condition).

FIG. 5. Flux Speed Distribution Functions for Sodium at Io's Exobase. Maxwell-Boltzmann flux speed distributions for sodium are shown for a most probable speed, v_m , of 1.3 km sec⁻¹ and 2.0 km sec⁻¹. Modified sputtering flux speed distributions are also shown for $\alpha = 3$ and a most probable speed of 1.0 km sec⁻¹, for $\alpha = 7/3$ and a most probable speed of 0.5 km sec⁻¹, and for $\alpha = 2$ and a most probable speed of 0.4 km sec⁻¹. All of the flux speed distributions are normalized to unit area under the curve.

FIG. 6. Model Calculations for the Io Eclipse Data Using a Maxwell-Boltzmann Flux Speed Distribution. The atomic sodium column density profile near Io determined from the 1985 eclipse data by Schneider *et al.* (1991) is shown by the open circles. The model calculated column density profiles are shown by solid dots for the (cylindrically-averaged) corona, by solid triangles for the forward cloud along the east-west slit direction, and by solid squares for the trailing cloud along the east-west slit direction. These column density profiles were calculated using the Io sodium cloud model of Smyth and Combi (1988b) for their case C description of the plasma torus and for an Io geocentric phase angle of 92.9 degrees and an Io System III longitude angle of 48.6 degrees, which are similar to the emission 4 observation conditions in Table 2. Sodium was ejected uniformly from

an assumed exobase of 2600 km radius with a velocity dispersion for a Maxwell–Boltzmann flux distribution, where in (a) $v_m = 1.3 \text{ km sec}^{-1}$ and $\phi_0 = 3.0 \times 10^8 \text{ atom cm}^{-2} \text{ sec}^{-1}$, and in (b) $v_m = 2.0 \text{ km sec}^{-1}$, and $\phi_0 = 1.8 \times 10^8 \text{ atom cm}^{-2} \text{ sec}^{-1}$ (see text).

FIG. 7. Model Calculations for the East-West D₂ Brightness Profiles Using a Maxwell–Boltzmann Flux Speed Distribution. The east-west D₂ brightness profile near Io in both the trailing and forward cloud directions as determined by the emission 4 data of Schneider *et al.* (1991) are shown by the open circles. The east-west profile envelopes in both the trailing and forward cloud directions as determined from the sodium cloud image data are shown by the shaded areas (see Fig. caption 4). The descriptions for the calculated profile symbols, the sodium cloud model and plasma torus, and the Maxwell–Boltzmann flux distribution in (a) and (b) are the same as in the caption of Fig. 6.

FIG. 8. Model Calculations for the Eclipse Data Using a Modified Sputtering Flux Speed Distribution. The atomic sodium column density profile near Io determined from the 1985 eclipse data by Schneider *et al.* (1991) is shown by the open circles. The model calculated column density profiles are shown by solid dots for the (cylindrically-averaged) corona, by solid triangles for the forward cloud along the east-west direction, and by solid squares for the trailing cloud along the east-west direction. These column density profiles were calculated using the Io sodium cloud model of Smyth and Combi (1988b) for their case C description of the plasma torus and for an Io geocentric phase angle of 92.9 degrees and an Io System III longitude angle of 48.6 degrees, which are similar to the emission 4 observation conditions in Table 2. Sodium was ejected uniformly from an assumed exobase of 2600 km radius with a velocity dispersion for a modified sputtering flux distribution, where in (a) $\alpha = 3$, $v_m = 1.0 \text{ km sec}^{-1}$, and $\phi_0 = 3.2 \times 10^8 \text{ atom cm}^{-2} \text{ sec}^{-1}$, in (b) $\alpha = 7/3$, $v_m = 0.5 \text{ km sec}^{-1}$, and $\phi_0 = 4.2 \times 10^8 \text{ atom cm}^{-2} \text{ sec}^{-1}$, and in (c) $\alpha = 2$, $v_m = 0.4 \text{ km sec}^{-1}$, and $\phi_0 = 4.7 \times 10^8 \text{ atom cm}^{-2} \text{ sec}^{-1}$.

FIG. 9. Model Calculations for the East-West D2 Brightness Profiles Using a Modified Sputtering Flux Speed Distribution. The east-west D2 brightness profile near Io in both the trailing and forward cloud directions determined by the emission 4 data of Schneider *et al.* (1991) are shown by the open circles. The east-west profile envelopes determined from the sodium cloud image data are shown by the shaded areas (see caption of Fig. 4). The descriptions for the calculated profile symbols, the sodium cloud model and plasma torus, and the modified sputtering flux distribution in (a), (b) and (c) are the same as in the caption of Fig. 8.

FIG. 10. Two-Dimensional Nature of the Sodium Column Density in Io's Corona. Contours for the two-dimensional column density in Io's corona are shown in the sky-plane of the earth as determined from the sodium cloud model calculation for the modified sputtering flux speed distribution described in Fig. 8(b) for $\alpha = 7/3$. The vertical and horizontal directions are the projected directions that are, respectively, perpendicular and parallel to the semi-major axis of the Io's orbital ellipse on the sky plane. The scale is in kilometers, and the small tick marks are separated by 1000 km. Io's location and size are shown to scale by the black circle. The sodium column density contours in units of 10^{10} atoms cm^{-2} are, from inside to outside, 7, 5, 3, 2, 1, 0.7, 0.5, 0.3, and 0.2.

FIG. 11. Total Source Rate Speed Distribution Function for Sodium at Io's Exobase. The total source rate speed distribution function at Io's exobase, in units of 10^{26} atoms sec^{-1} $(\text{km/sec})^{-1}$, is composed of three separate source rate speed distributions as discussed in the text and is shown for two different source strength for the higher-speed zenocorona source centered about 57 km sec^{-1} . The lower (solid line) and upper (dashed line) curves correspond, respectively, to the sodium zenocorona higher-speed source rate of 2.2×10^{26} atoms sec^{-1} (Smyth and Combi 1991) and 4×10^{26} atoms sec^{-1} . The two source rates for the higher-speed zenocorona source are shown so as to

exhibit its typical time-variable source strength range of $\sim 2\text{--}4 \times 10^{26}$ atoms sec^{-1} as reported by Flynn *et al.* (1994). The decomposition of the solid curve into its three separate source rate speed distributions is shown in the cutout and is determined by combining (1) the isotropic modified sputtering source rate distribution (dotted line in the cutout) for $\alpha = 7/3$, $v_m = 0.5 \text{ km sec}^{-1}$ and a source strength of 1.75×10^{26} atom sec^{-1} , (2) the nonisotropic lower-speed source rate distribution (short dashed line in the cutout) for the sodium zenocorona and directional feature centered about 20 km sec^{-1} , with a source strength of 1.1×10^{26} atoms sec^{-1} as determined by Smyth and Combi (1991), and (3) the nonisotropic higher-speed source rate distribution (longer dashed line in the cutout) for the sodium zenocorona centered about 57 km sec^{-1} , with a charge exchange source strength of 2.2×10^{26} atoms sec^{-1} as determined by Smyth and Combi (1991).

IO SODIUM CLOUD 1981

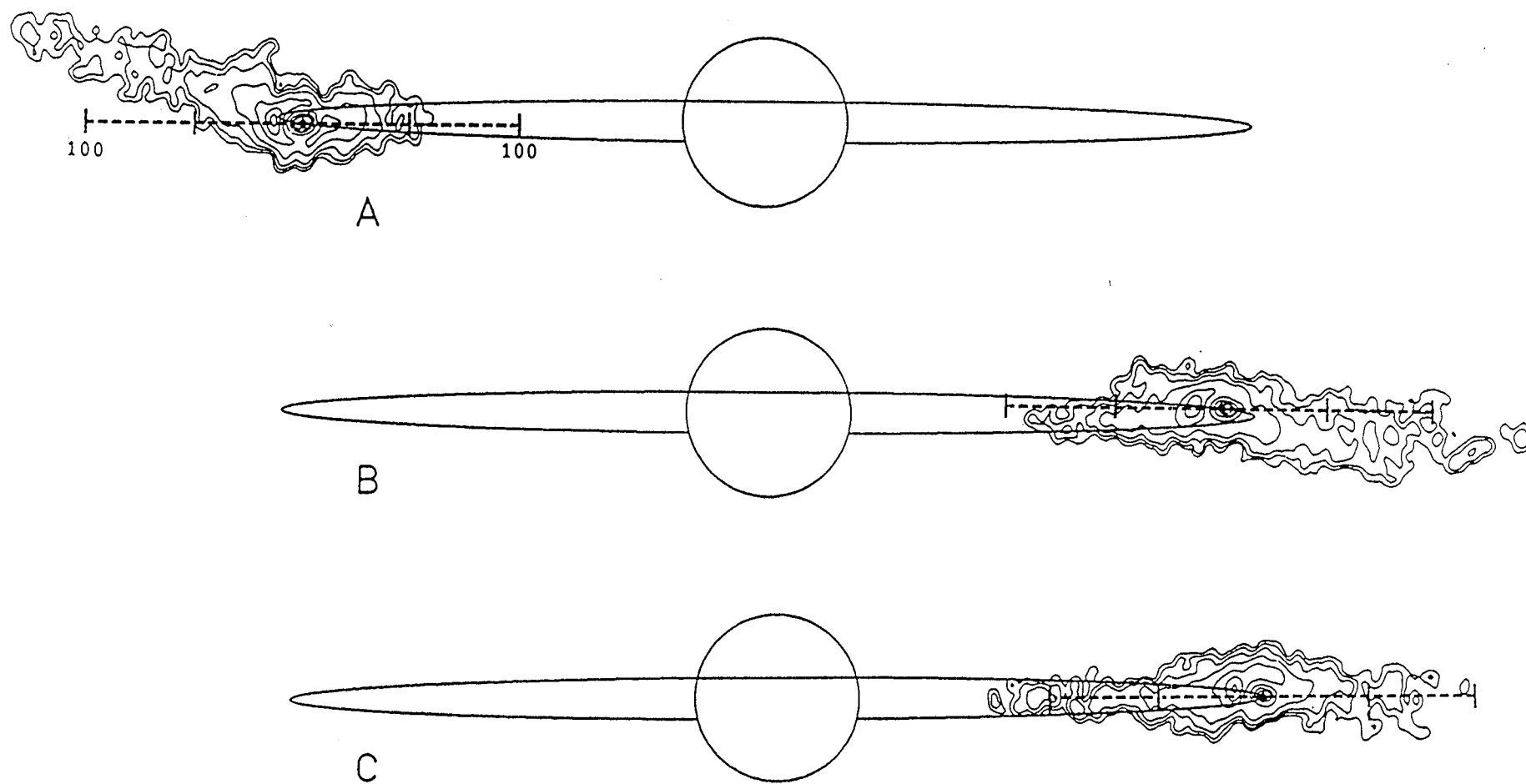


Figure 1

1985 Eclipse Data

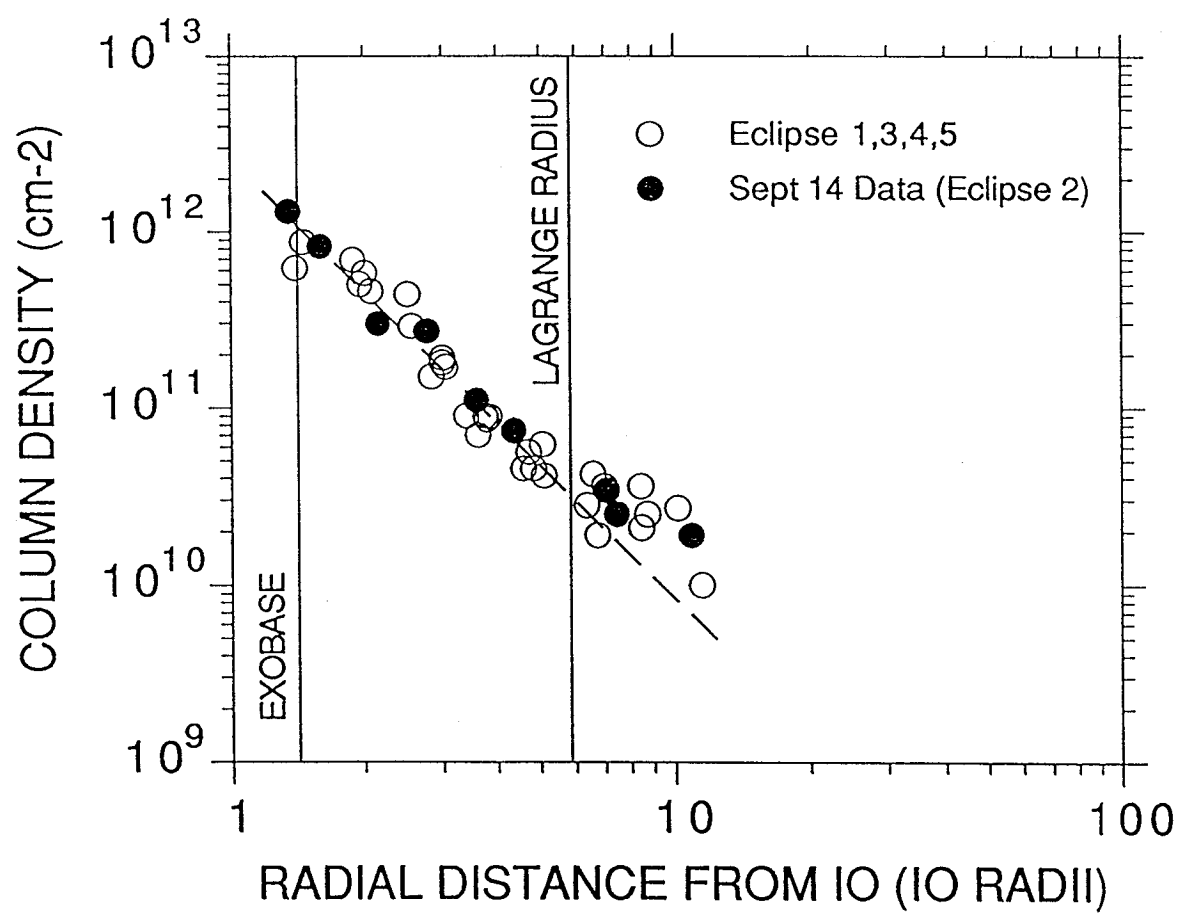


Figure 2

1985 Emission Data

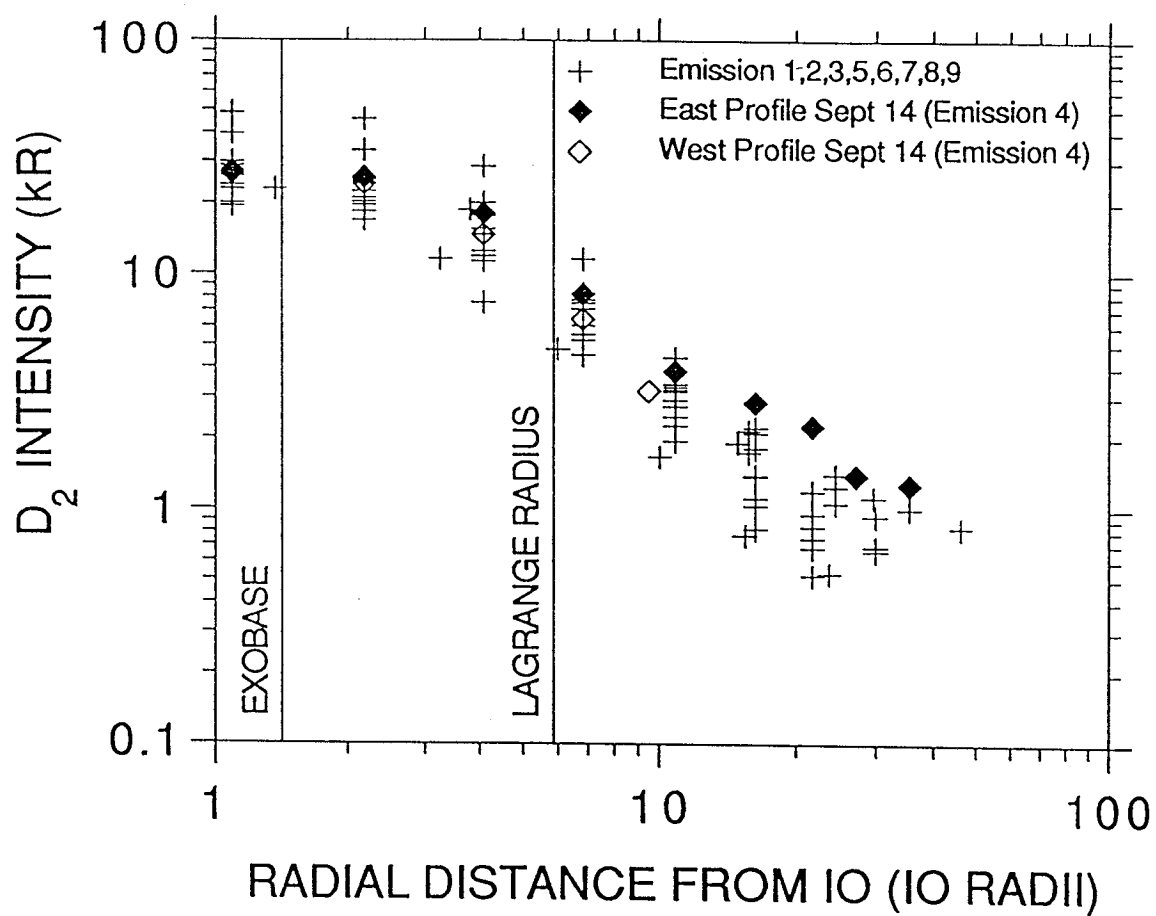
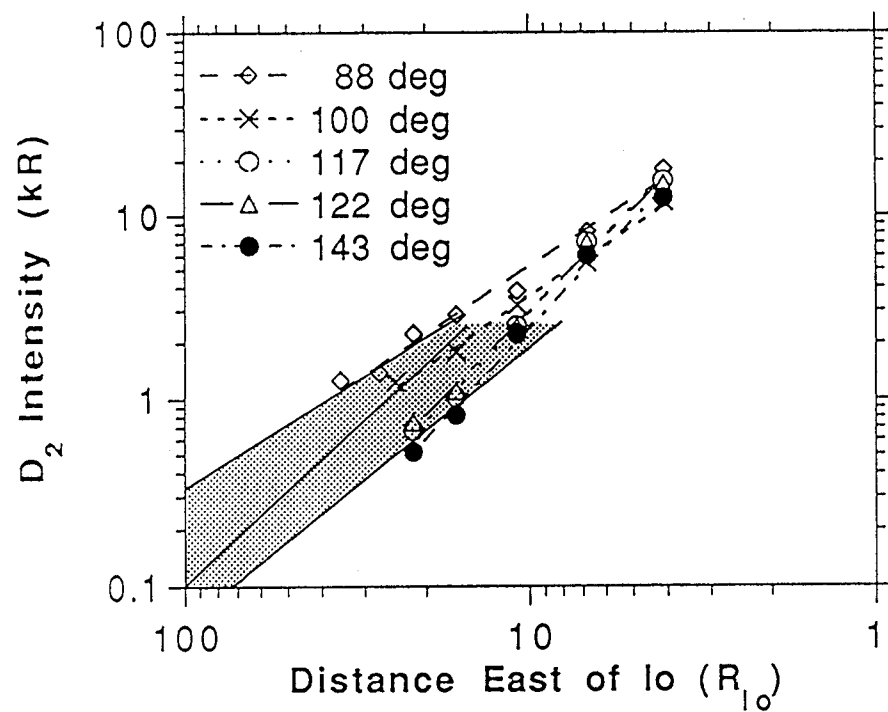
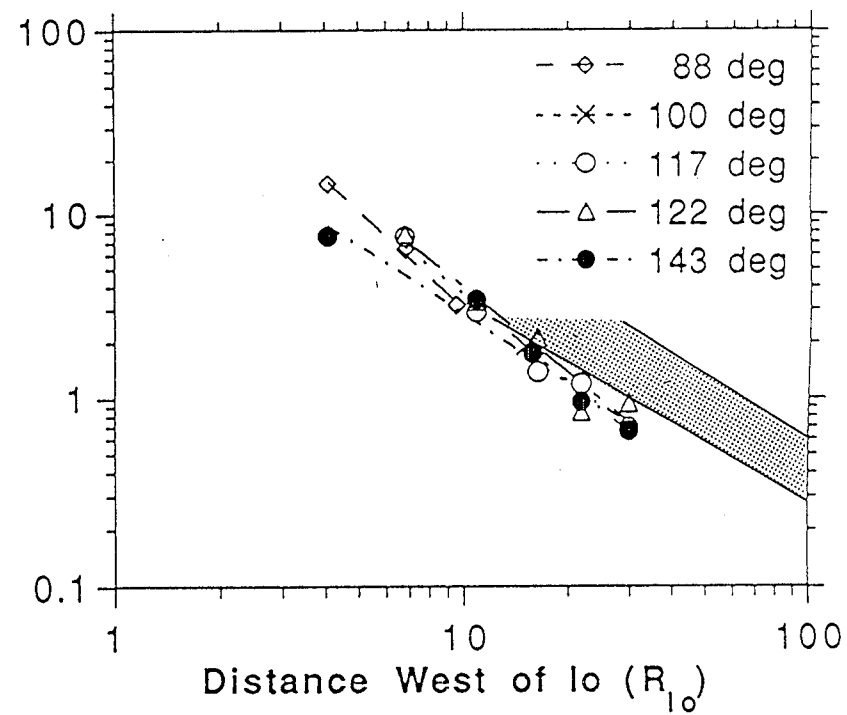


Figure 3

TRAILING CLOUD



FORWARD CLOUD



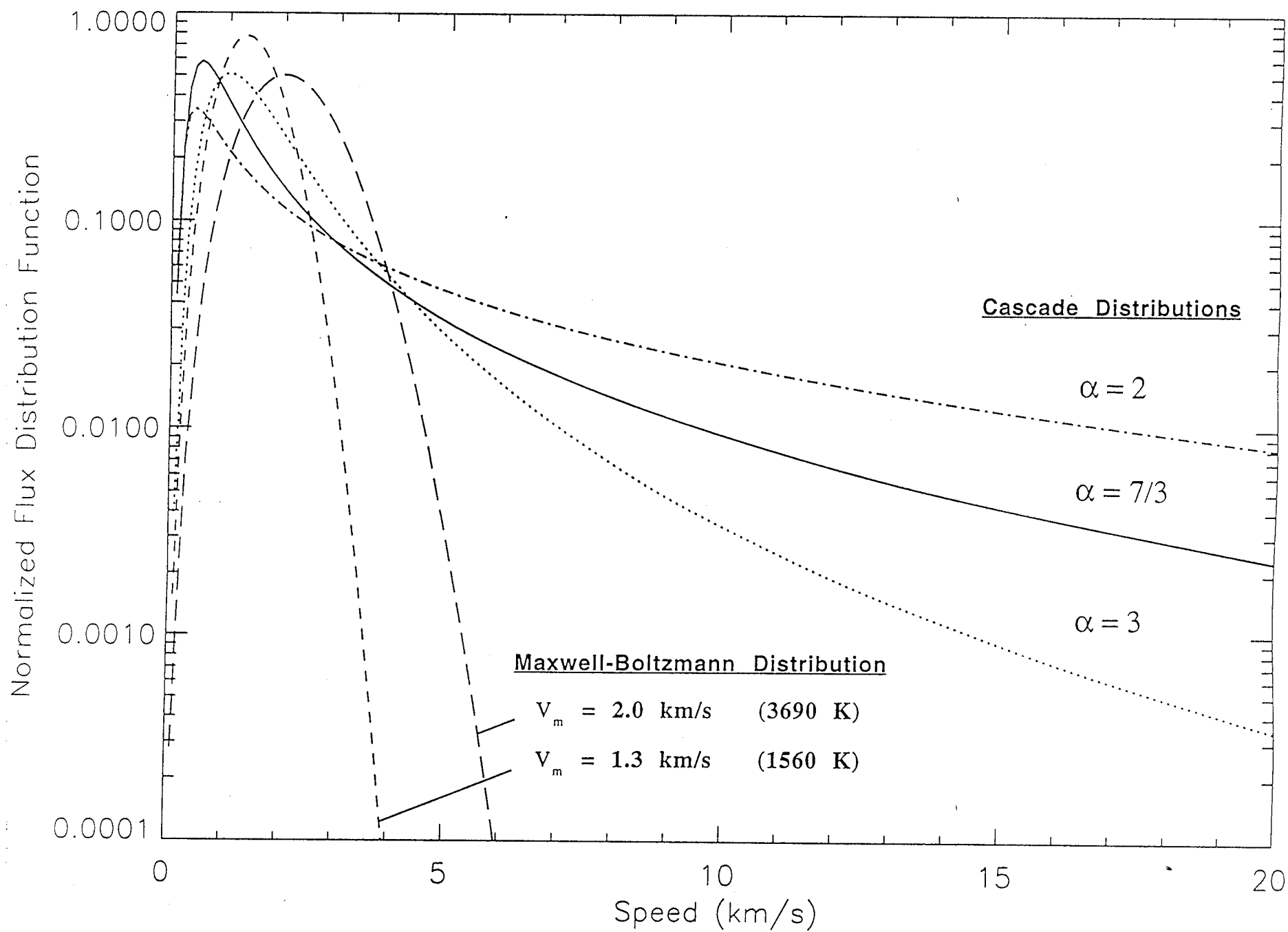


Figure 5

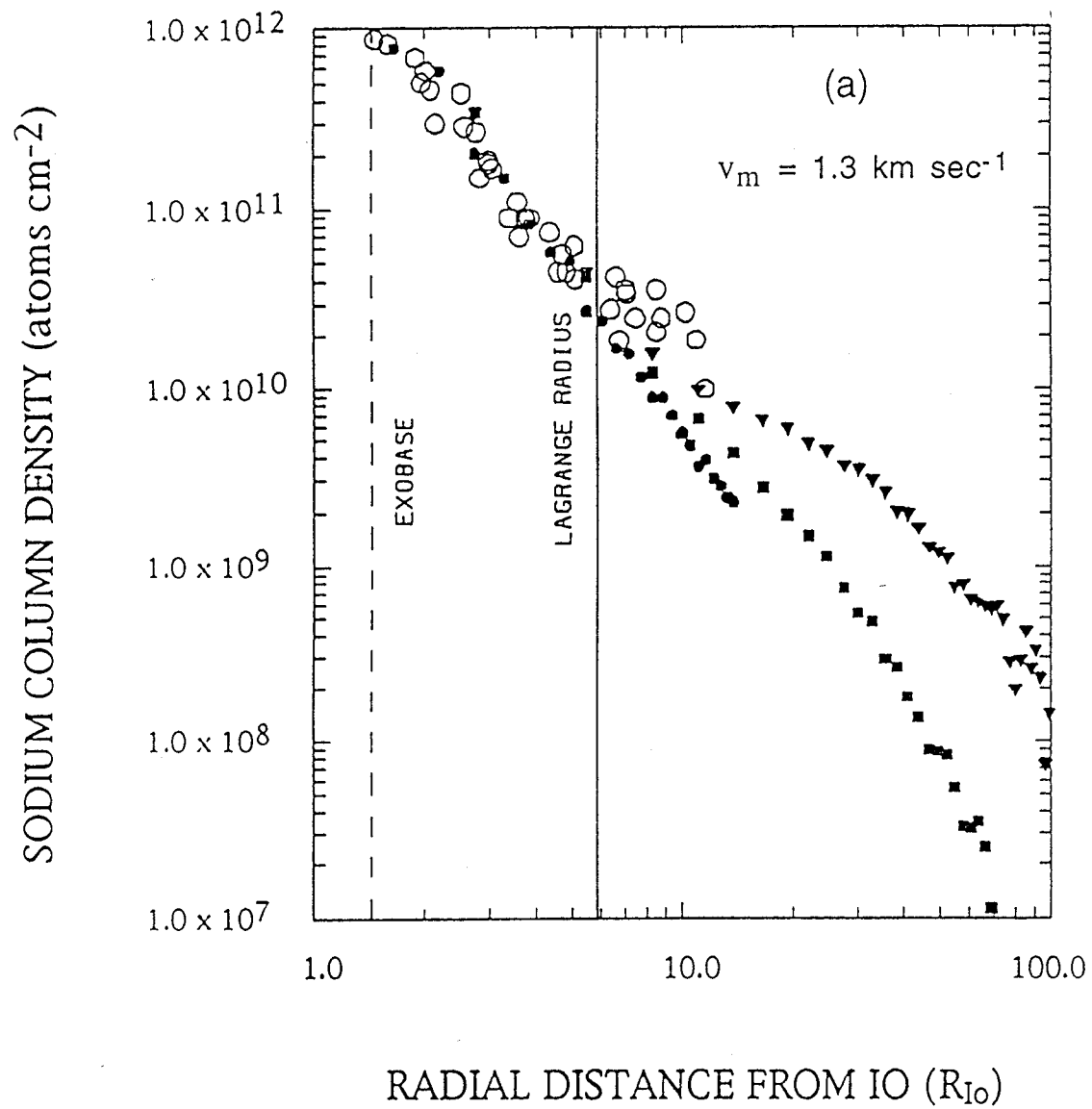


Figure 6a

SODIUM COLUMN DENSITY (atoms cm⁻²)

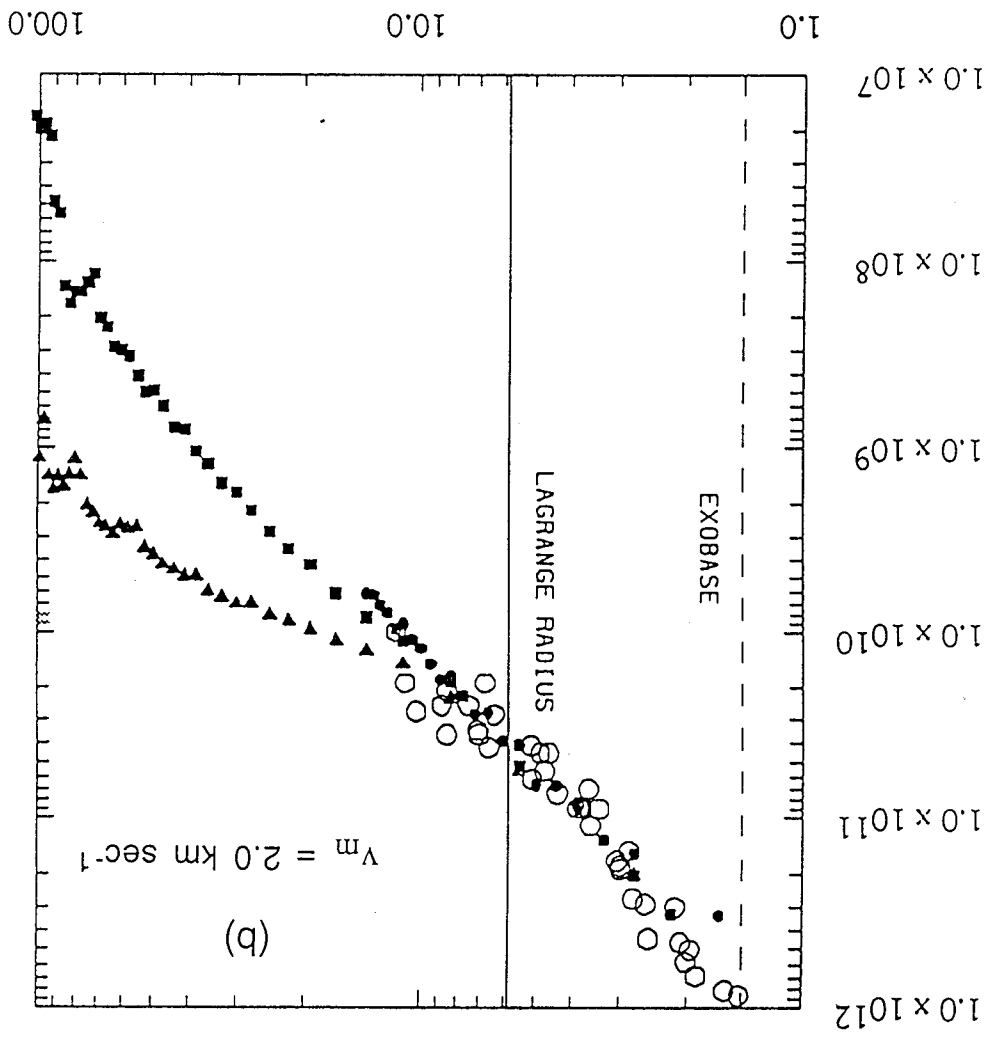
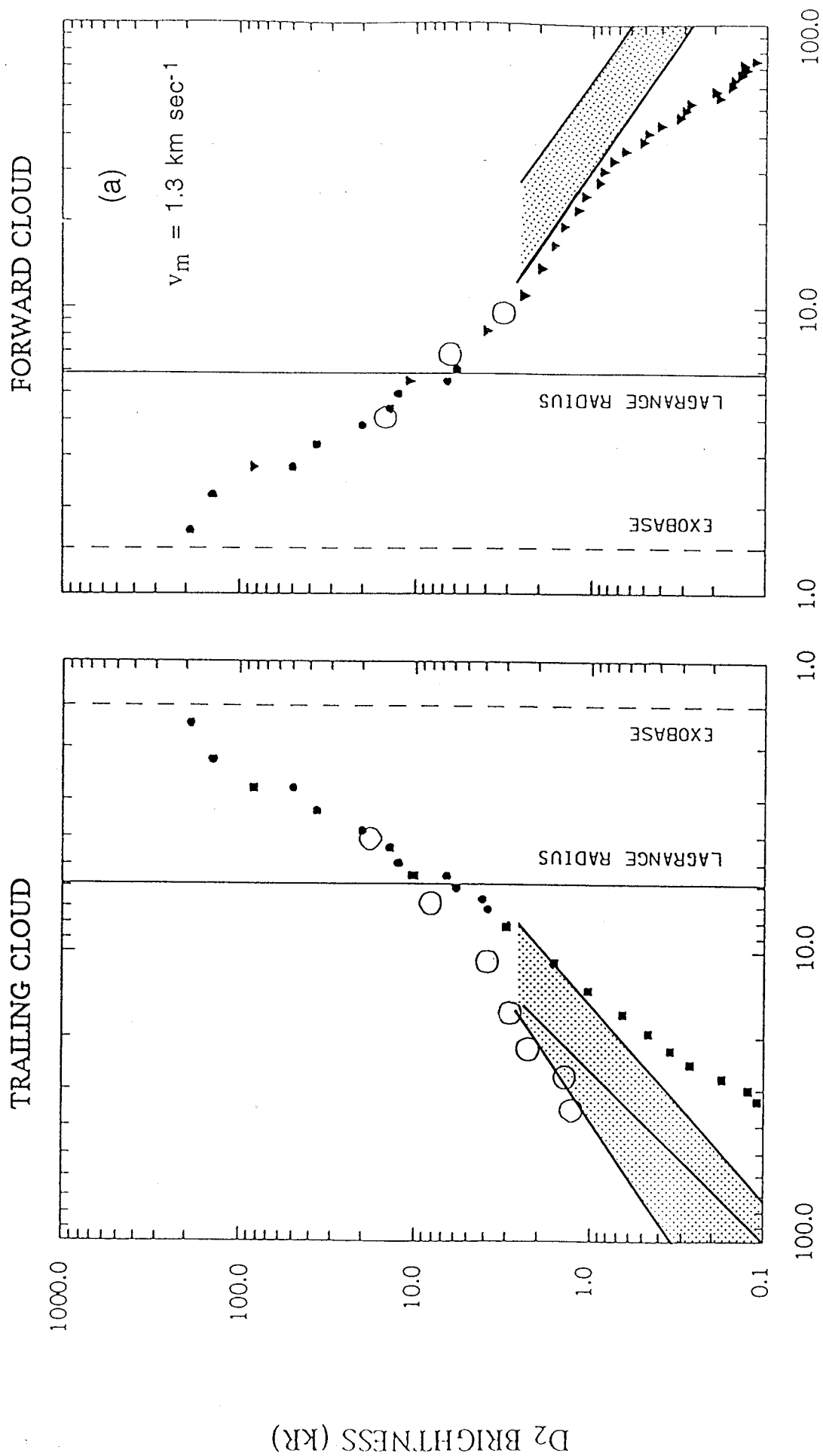


Figure 6b

RADIAL DISTANCE FROM IO (R_{IO})



D2 BRIGHTNESS (KR)

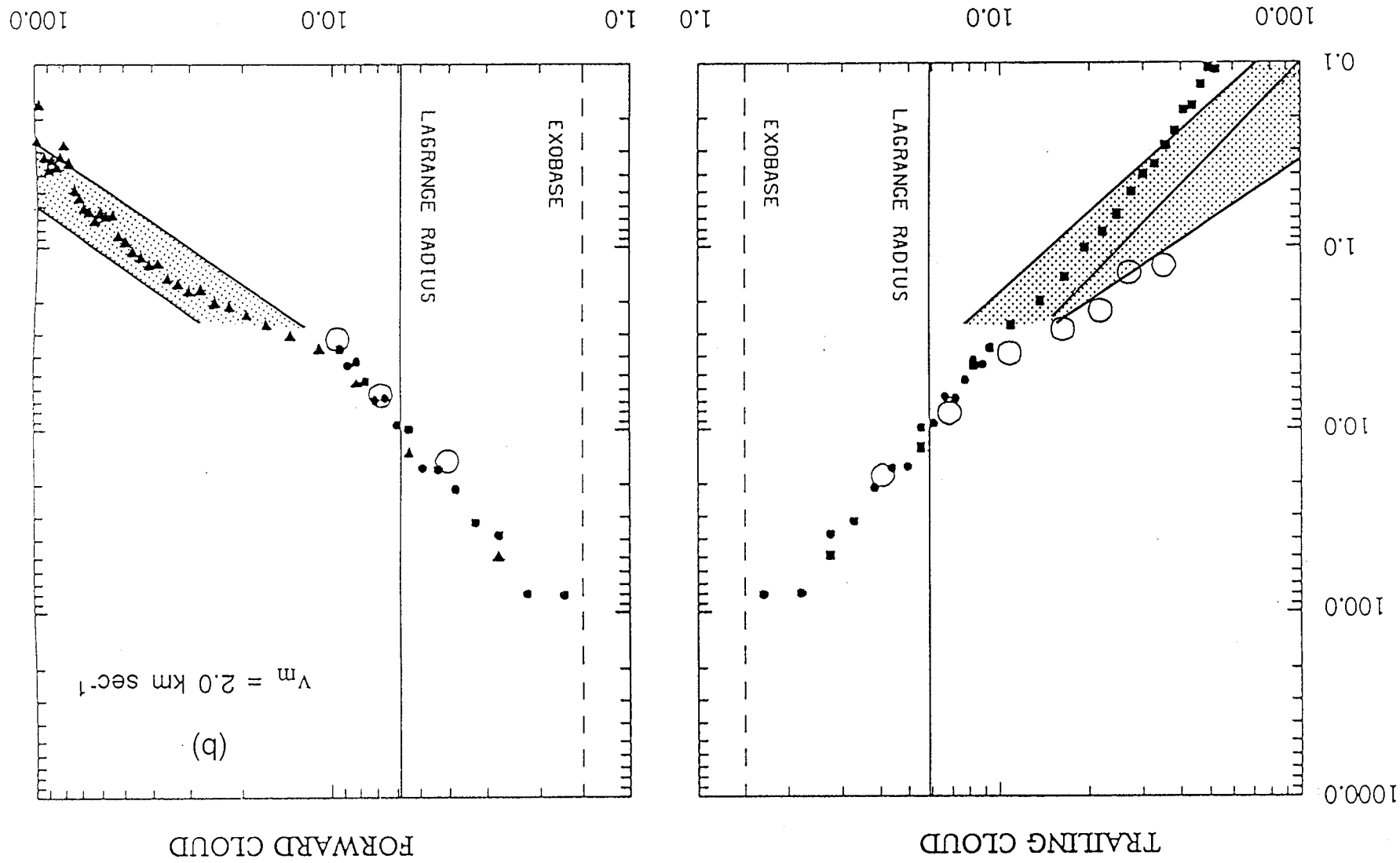
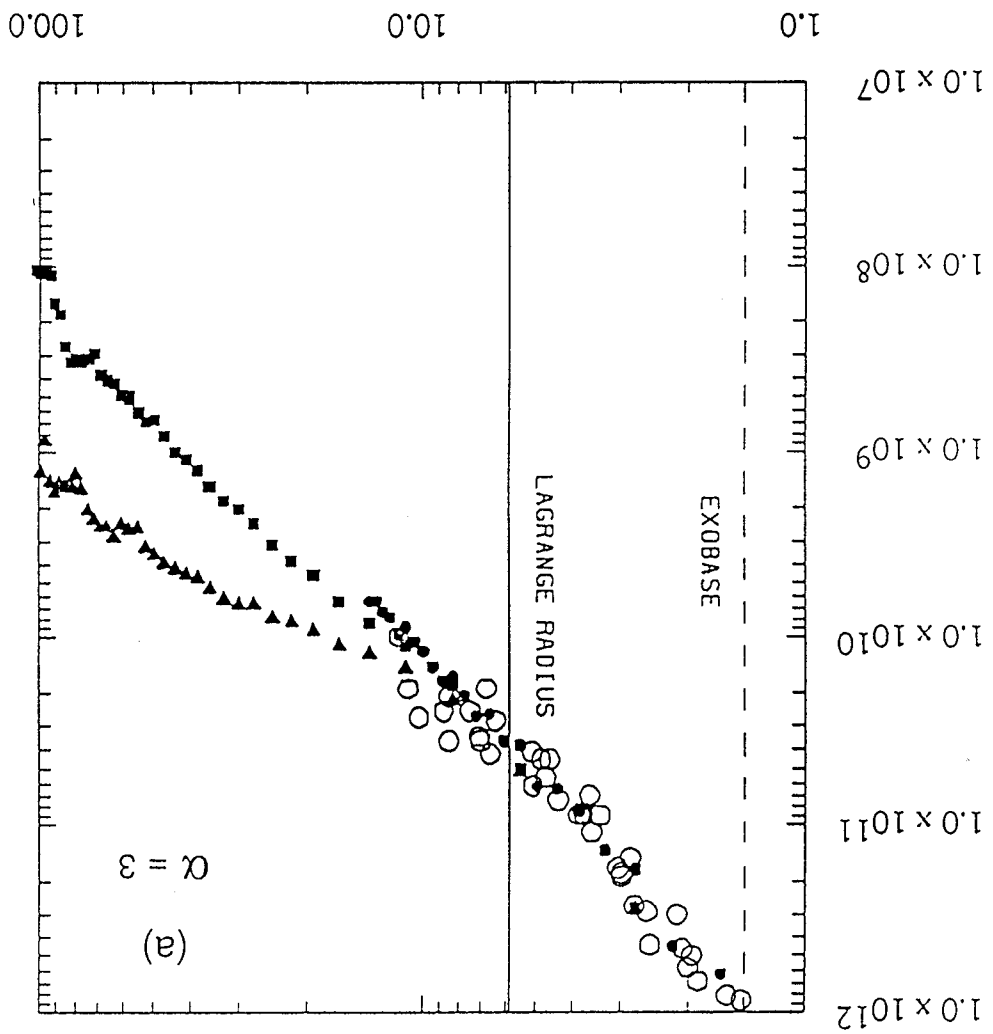


Figure 7b

SODIUM COLUMN DENSITY (atoms cm⁻²)



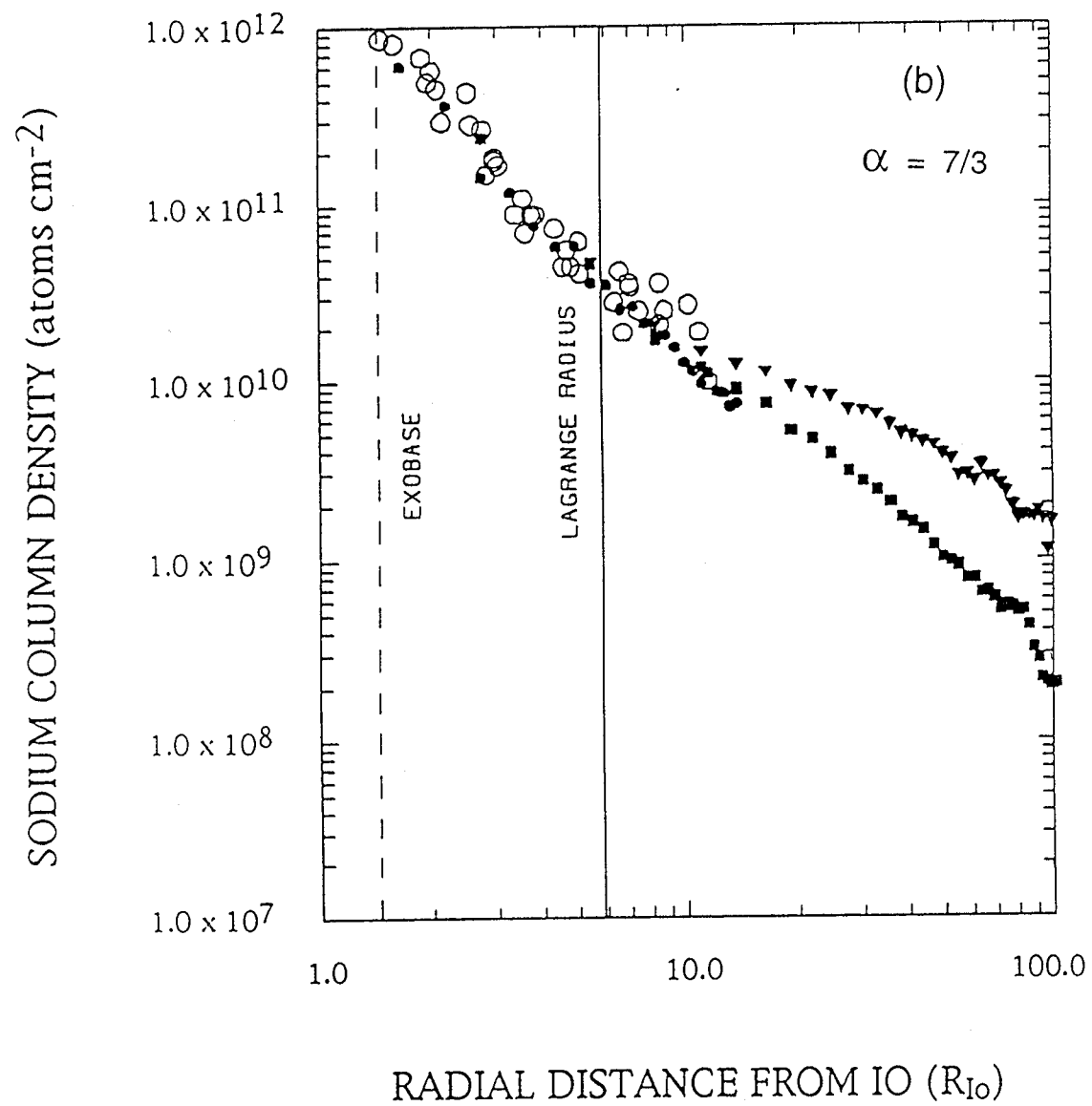


Figure 8b

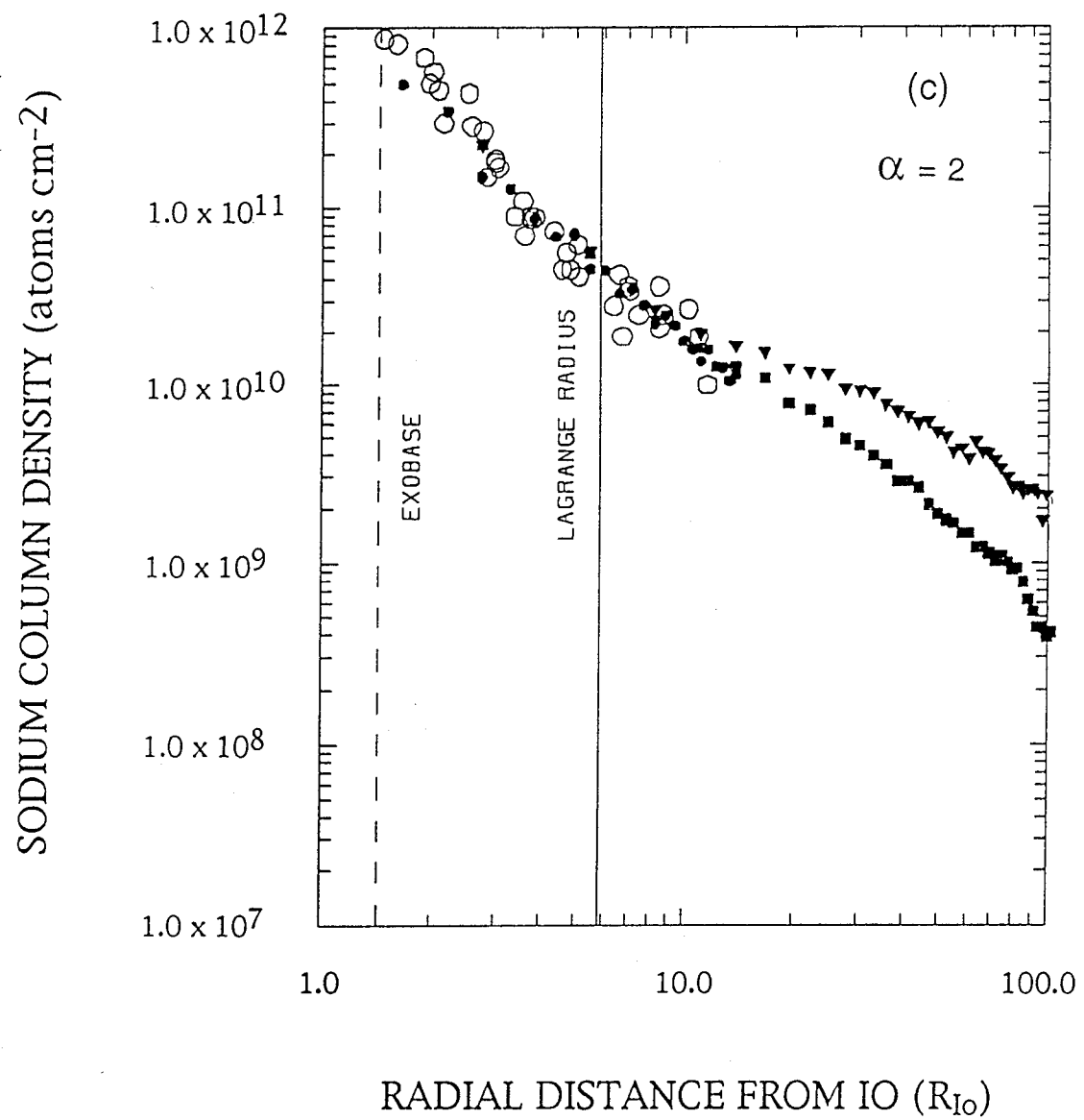


Figure 8c

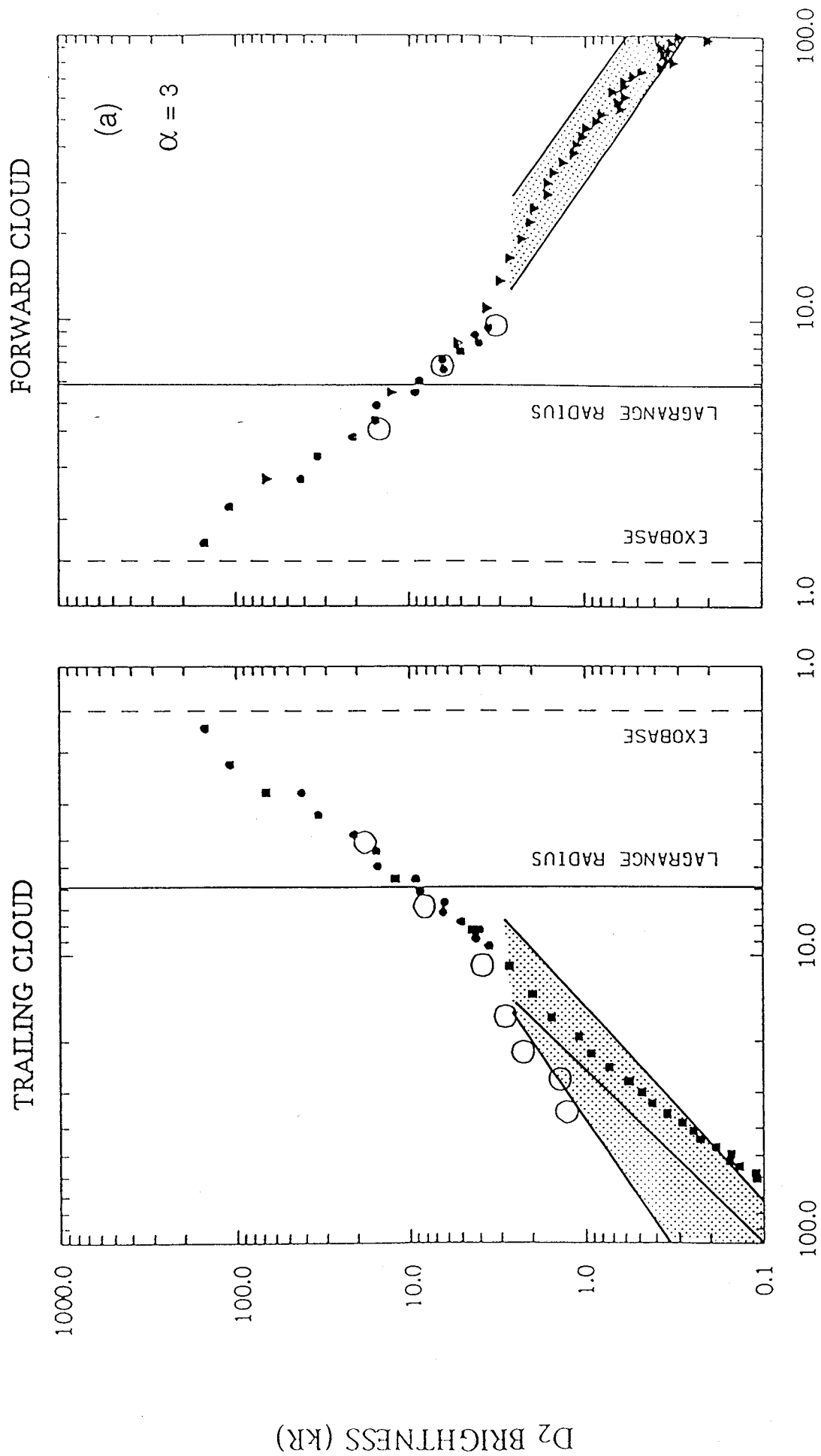
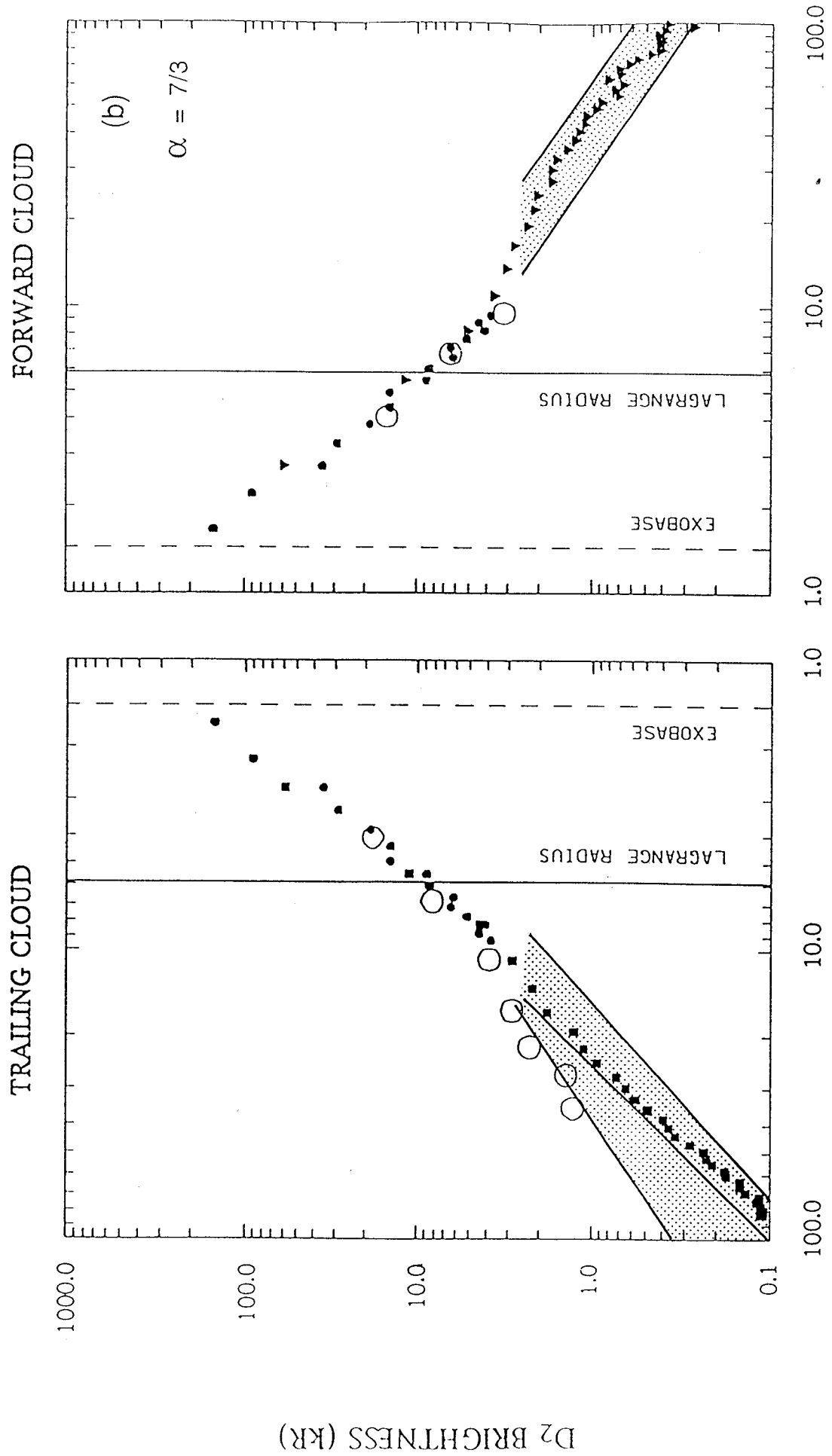
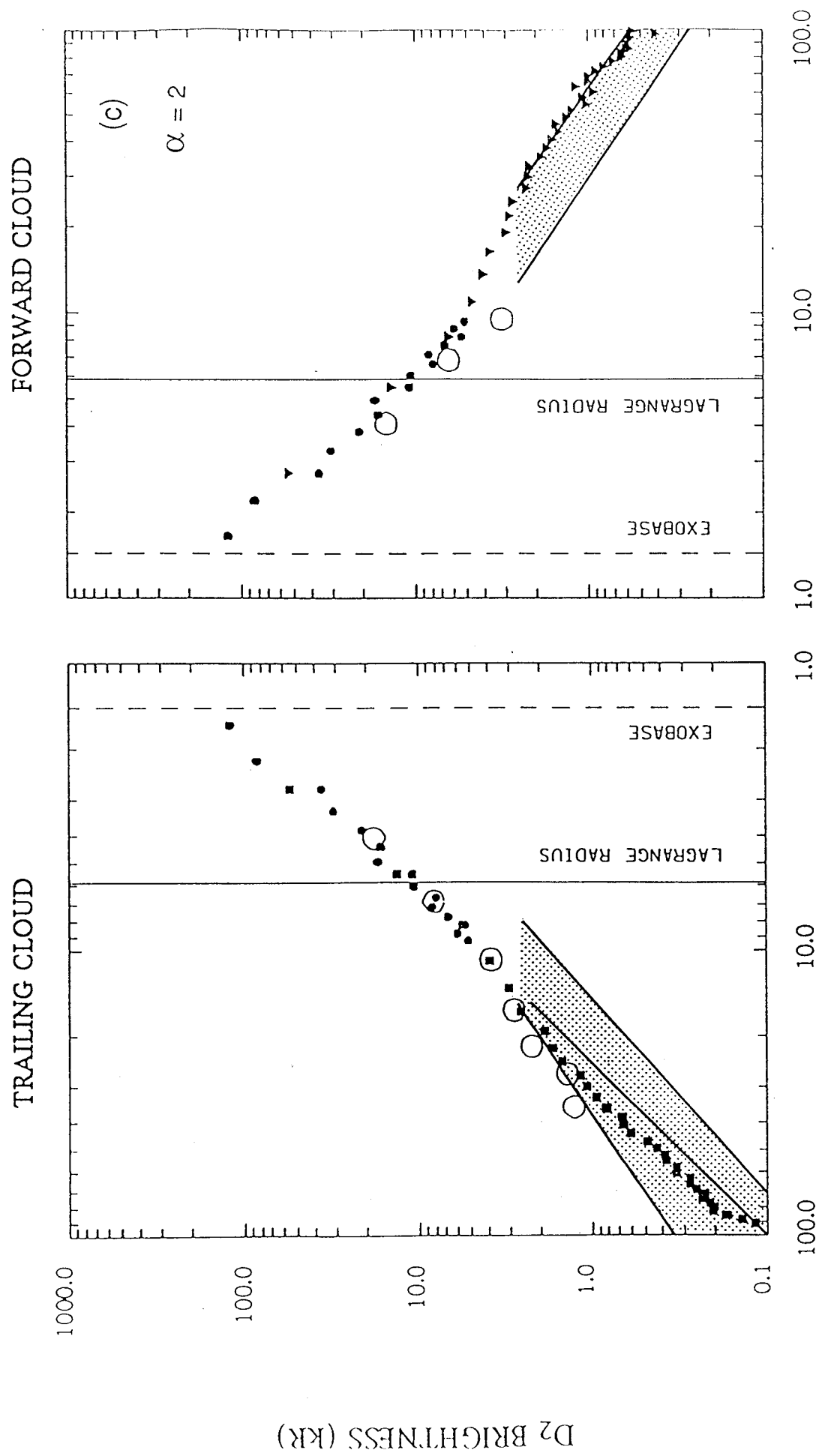


Figure 9a





RADIAL DISTANCE FROM IO (R_{IO})

Figure 9c

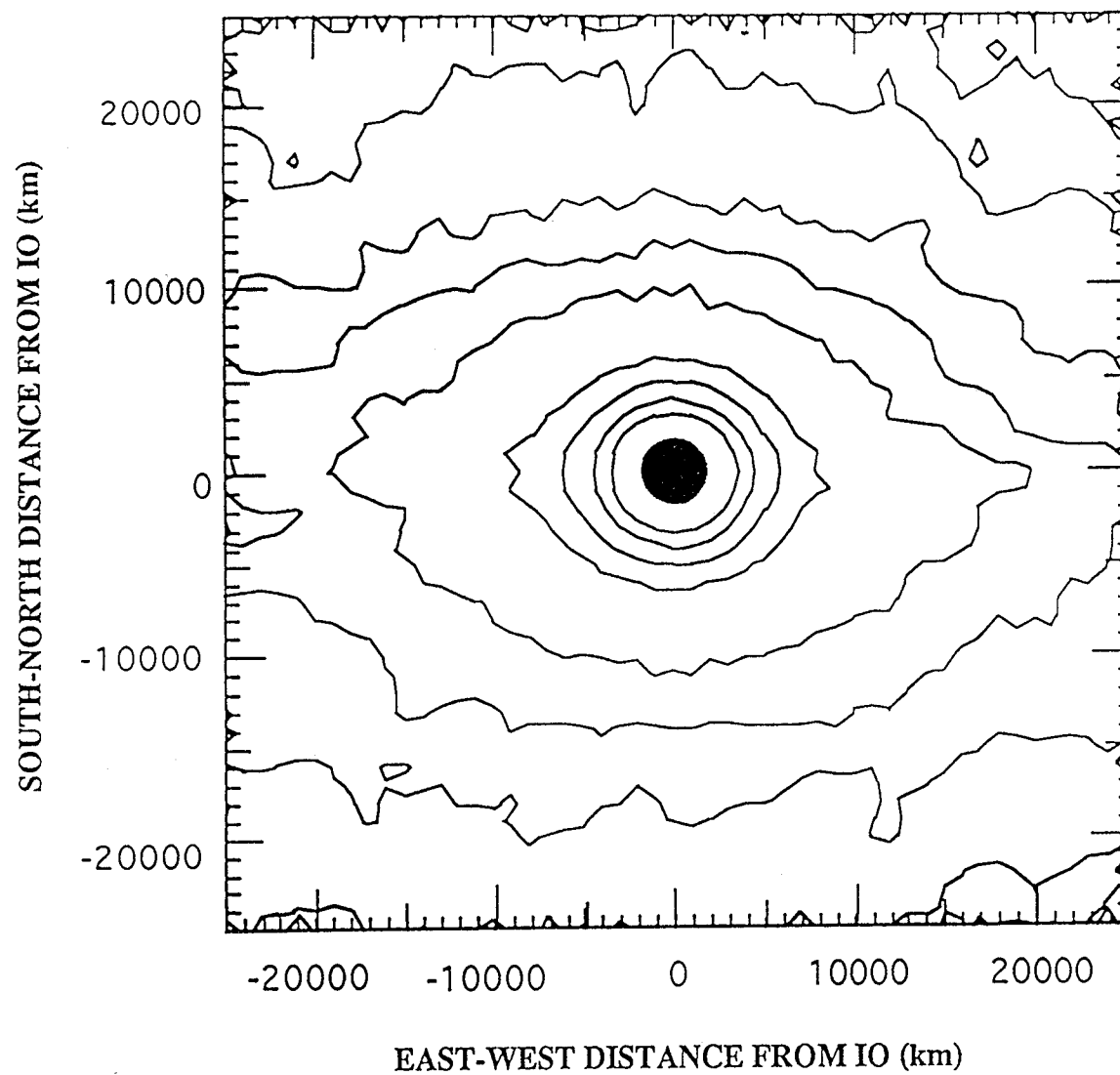


Figure 10

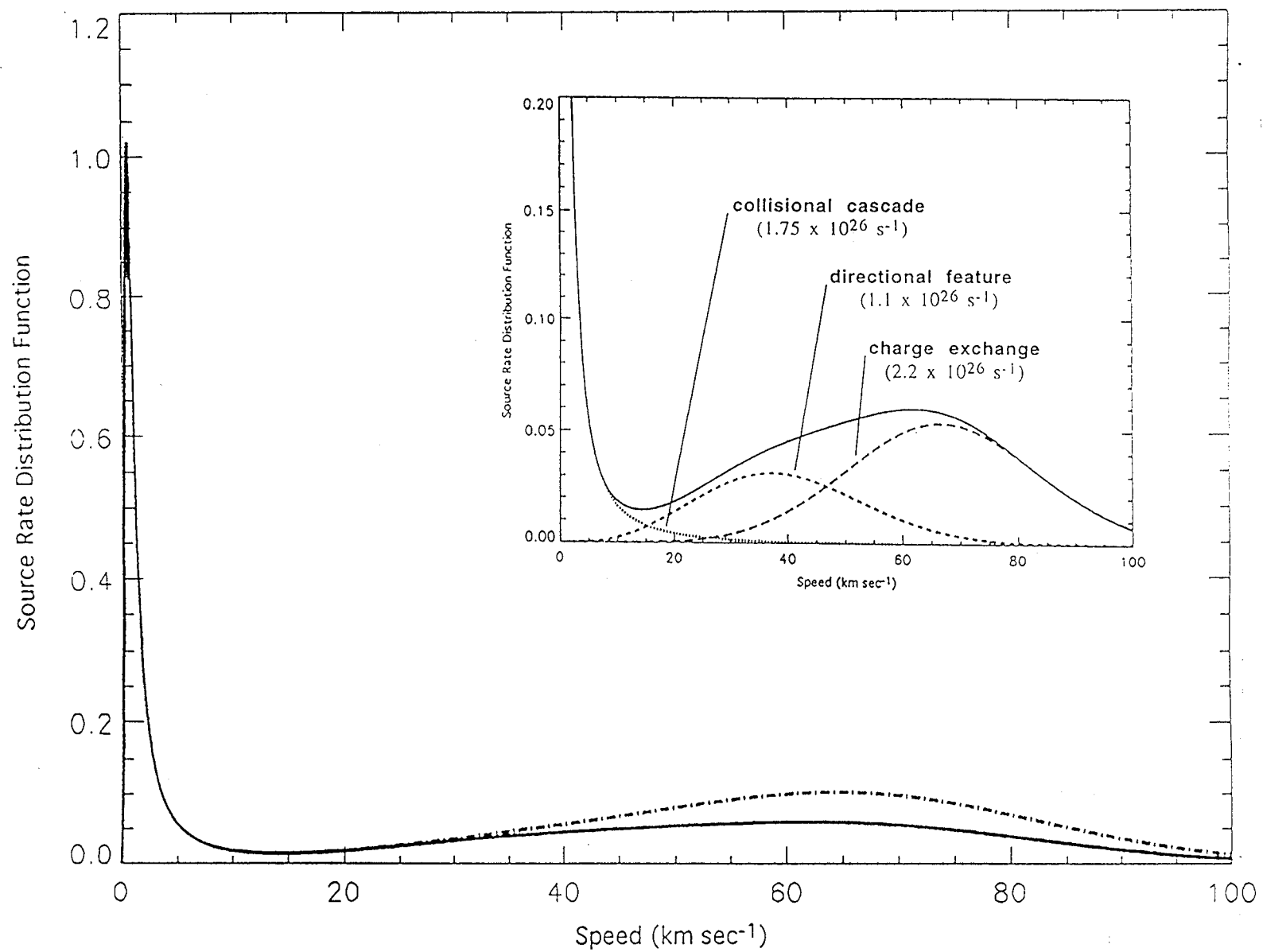


Figure 11

